Measurement of the ratio between the D^+ and the D^0 production cross section using an impact parameter method.

UNIVERSIDADE DE SANTIAGO DE COMPOSTELA

FACULTADE DE FISICA

Departamento de Física de Partículas

Patricia Conde Muíño

Doctoral Thesis

November, 2002.

Acknowledgments

Now that the thesis is finished, I arrived to the point where I have to thank all the people that made it possible. I just hope not to forget anybody, since too many people have contributed in different ways.

I will start thanking Bernardo Adeva for giving me the chance to join the High Energy Physics community, at the University of Santiago de Compostela.

I want to acknowledge Lluís Garrido and Ramón Miquel for offering me the possibility to go to Barcelona and join the HERA-B collaboration. Ramon was my advisor during the first two years and with him I had the first contact with the experiment. I have enjoyed the work during that time. To Lluís I'm in debt for many things but specially for all the support I have received from him in many difficult moments. His practical advises have been very useful.

I don't have words to express my gratitude to Cristóbal Padilla, for many, many things, starting for accepting being my supervisor two years ago. He has been a great supervisor, probably the best I could have. He has given me many ideas, very good advises and I've enjoyed all the discussions with him. But he has also been a good friend, very patient to listen to my fears and my doubts. He always knew how to encourage me to continue working in the difficult moments.

I would like to thank all the HERA-B collaboration, in general, for making this thesis possible. There are many people that have contributed to my analysis with ideas and comments: Michael Schmelling, Mikhail Zavertiaev, Federico Sánchez, Antonio Zoccoli, Marko Starič, Alan Schwarz, and many other. I want to mention also Denis Djumič, who was the first one to see D mesons in HERA-B and who had helped me to start.

During my time at the tracking group I've enjoyed working with many people, in particular, with all the RTRA 2001 group: S. Maschiocci, M.Villa, B.Giaccobe, M. Hohlmann, R.Spighi, U.Uwer, S. Spiridonov, W. Hulsbergen and O. Igonkina. I explicity want to thank Silvia Maschiocci, who has acted as a supervisor for me in many occasions. I want to mention how much I've enjoyed to work with Olya and Wouter in the tracking group. I'm in debt with them for so many questions they had answered me. I would like to thank also Sasha Spiridonov, who always had time to answer my questions about the tracking algorithms

I want to acknowledge the RICH group, and specially the all the people from Ljubljana (P.Križan, M.Starič, T.Zivko, S.Korpar, Damijan, Andrej and Rok) not only because it has been a pleasure for me to work with them but also for their hospitality and friendship.

I should not forget all the colleagues with whom I shared the good and the bad moments during this four years: Dani, with his different way of seeing the world; Ignasi, for his companionship; Rok and Spela, for the nice evenings at their place; Andrej, for his good humor; Damijan, for his friendship; Federico, for listening to me in the bad moments; Imma, for having a smile for everybody; Benedetto for the dinners in Altona; Dickson, for the real Brasilian caipirinhas and the long talks; Steve, for cheering up the people; Galia for the chats at the office; and the students at HERA-B: Marteen, Maaijke, Brian, Dorothea, Marc-Andre, ... who contributed for a nice working atmosfere.

I want to thank all the good friend I have made in Barcelona: Angels, because I could always count on her; Jordi for making us laugh; Albert, for our discussions; Joan for the long mails; Olga for her good humor; María Jesús, for her friendship; David, for showing always a different point of view; Ana and Jens, because they were like my family during the time I was leaving with them; ... They all made my time at Barcelona unforgettable.

Thanks also to my colleagues in the Particle Physics department, in Santiago: Ana, Jose, Cibrán, Pablo, Abraham, Manolo, ... for the coffee breaks, for their jokes, for the dinners and all the good moments during my first year in Santiago.

And of course, all the friends from Santiago (Maite, César, Carlota, Marcos, Álvaro, Tino, Silvia, Rosa, Laura, Pablo, Carlos, Pili, Alejandra, Antonina, Bea, Lucky, Jose Rodríguez, Jose Viña, ...) because they are special, and, even if I don't see them very frequently, I know that they are there at any time I need them.

To all my family who have always believed in me. To my sister and my parents, for listening to me, raising my humor and supporting me all the time. To Tere and Pepín, for being like my second parents, for their good advises and their support. To Sonia and Laura, for being like my sisters.

To Vasco, for all the support I have received from him. He had an enormous patience to keep me calm and to stand me in the bad moments. He has given me the strengths I needed to continue.

Finally, I would like to thank all the people that have helped me with the paper work: Maite and Jose, during the four years I was away from Santiago, and Beatriz Mayo Vieito, for all the paperwork for my PhD.

Contents

List of Tables

List of Figures

Chapter 1

Introduction

Measurements of heavy quark production in deep-inelastic scattering are good tests of the perturbative QCD theory in a wide energy range, from the top quark mass, where the perturbation theory is expected to be very accurate, to the charm quark mass, where some non perturbative effects are expected to be important. Different production mechanisms can be studied in electron-positron annihilation, photon-hadron, photon-photon and hadron-hadron collisions.

Several experimental measurements have been performed to test the production and hadronization of the charm quark: heavy quark pair production, differential distribution of heavy hadrons, jets distributions, quark correlations, ... Although most of these results are in qualitative agreement with the theoretical predictions, there are some quantitative discrepancies that may be solved with a better understanding of the non-perturbative processes in the charm production and hadronization mechanisms. One example of such discrepancies is the D^+ to D^0 production cross section ratio. The theory predicts that the D^0 production cross section is approximately a factor three larger than the D^+ production cross section, $\sigma(D^+)/\sigma(D^0) \sim 0.33$. The experimental results in $\pi - N$ collisions are close to the theoretical expectation, while the measurements done in $p - N$ experiments give comparable values for the D^+ and the D^0 production cross sections. There is no theoretical reason why the $\pi - N$ and the $p - N$ collisions should give different results. New measurements in $p - N$ collision can help to reduce the experimental errors and solve the puzzle.

In this thesis a measurement of the D^+ to D^0 production cross section ratio will be presented. The measurement has been obtained with the 920 GeV proton-nucleus events recorded by the HERA-B experiment, using the HERA accelerator at DESY (Hamburg).

The HERA-B experiment was designed to measure CP violation in the golden B_d^0 decay mode, using the HERA proton beam to produce collisions with an internal target.

HERA-B is a forward spectrometer with a wide angular coverage, composed of a vertex detector, a tracking system and particle identification detectors. The experiment started to take data during the year 2000, dedicating most of the running period to the commissioning of the detector. Nevertheless, there were some runs dedicated to physics studies. The results presented in this thesis were obtained with approximately 5 million events taken with a single high-p_T lepton trigger, in August 2000.

The D^+ to D^0 production cross section is obtained by measuring the amount of D^+ and D^0 decays produced in the single lepton sample, corrected by the ratio of the reconstruction and selection efficiencies, obtained with the Monte Carlo simulation program.

The D mesons are reconstructed in the decay modes $D^+ \rightarrow K^-\pi^+\pi^+$ and $D^0 \rightarrow K^-\pi^+$, plus charge conjugated decays. The main features of those decays, the presence of a kaon and the long lifetime of the D mesons, are exploited in order to select the few D meson decays that are expected in the single lepton sample.

A method to separate the decays of long living particles from the background was developed. The method exploits the large impact parameters that characterize the daughter track of the long living particle. The basic point is the definition of a three-dimensional signed impact parameter significance of a track with respect to the primary vertex. The sign is defined in such a way that the tracks coming from the decay of a long living particle have always positive impact parameters, while the tracks produced in the main interaction have equal probability of positive or negative sign. The significance of the tracks with negative impact parameter is used to define the probability that a track was produced in the primary interaction. The probabilities of all the tracks produced in the decay are combined into one quantity that is used to select the desired decays with a very good efficiency and high background rejection.

The impact parameter method was then applied to the reconstruction of the D^+ and D^0 decays in the single lepton triggered data, and the ratio between the D^+ and the D^0 production cross section was obtained. The measurement is in agreement with the other results obtained in proton-nucleus collisions at high proton energies [39].

The thesis is organized as follows: chapter 2 reviews the theory of the heavy quark production in perturbative QCD and, in particular, the prediction for the ratio between the D^+ and the D^0 production cross section. In the third chapter the HERA-B detector is described, emphasizing the parts that are more important for the analysis presented here. A description of the data sample and the reconstruction chain is given also in the chapter 3. The impact parameter method is explained in chapter 4. In chapter 5, the optimization of the D^+/D^0 selection requirements are presented. Chapter 6 corresponds to the measurement of the ratio and the study of the systematic errors. The conclusions are presented in the last chapter.

Chapter 2

Charm hadroproduction

Despite the large amount of existing experimental data, heavy quark production and hadronization is still a controversial subject, as the theoretical expectations, obtained with the perturbative QCD theory, do not completely agree with the experimental results. The observed deviations may provide clues about the non-perturbative effects that are important or they may indicate that some theoretical assumptions are wrong.

In this chapter, the theory of the heavy quark production and hadronization will be reviewed. The phenomenological applications of these results will be presented, remarking the areas where some discrepancies still remain. In the last section one of these discrepancies will be discussed in more detail.

2.1 The charm production cross section

Hadron-hadron collisions at very high energies can be described as the interaction between the constituent partons of the hadrons (quarks and gluons). In some cases, these collisions involve only soft interactions between the partons that cannot be described in perturbative QCD because the strong coupling constant, α_s, is large when the momentum transfer between the partons involved in the collision is small. There are some other cases where the quarks and gluons exchange a big momentum perpendicular to the collision axis (transverse momentum) or when the mass of the particles produced in the interaction is large. In these cases the lowest order QCD prediction is usually accurate enough to describe the process.

The production of quark pairs in a hadron-hadron collision is depicted in figure 2.1. The collision of hadrons A and B, with momentums P_A and P_B, can be thought as the interaction between two of their constituent partons, that are carrying a fraction of the incident hadron momentum, x_1 and x_2. Then, the differential cross section for quark pair production can be calculated by convoluting the probabilities of finding each of the

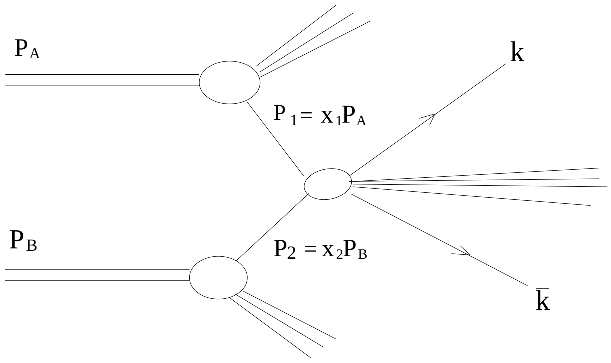

Figure 2.1: *Quark production mechanism in hadron-hadron collisions. The collisions of hadrons A and B, with momentums P_A and P_B is described by the interaction between two of their constituent partons, with a fraction of the incident momentum given by x_1 and x_2. The produced quark, anti-quark pair have momentums k and $\bar{k}$.*

partons in the incident hadrons with the cross section for the parton-parton interaction [1]:

$$d^3\sigma = \sum_{i,j} \int dx_1\, dx_2\, d^3\hat{\sigma}_{ij}(x_1 P_A, x_2 P_B, k, \bar{k}, m, \mu)\, F_i^A(x_1, \mu)\, F_j^B(x_2, \mu), \qquad (2.1)$$

where $k, \bar{k}$ are the momenta of the outgoing quarks produced in the collision and μ is the scale at which the strong interaction coupling constant is evaluated, that is of the order of the quark mass $\mu \sim m$. The functions F_i are the density functions of the partons inside the hadrons A and B, that represent the probability of finding a parton of the type i (or j) in a hadron A (or B). They are evaluated at the scale μ. $\hat{\sigma}$ is the cross section for producing the outgoing quark pair in the parton-parton interaction.

When the scale μ is much larger than the typical QCD scale, Λ_{QCD}, as it is the case for heavy quark production, the partonic cross section, $\hat{\sigma}$, can be calculated as an expansion in terms of the strong coupling constant, α_s. For the heaviest quark, the top, $\mu \sim m_t \gg \Lambda_{QCD}$ ($\Lambda_{QCD} \sim 200 - 300 MeV$), so the perturbative theory can be applied reliably, and the lowest order formula should be enough to describe the production. For the charm quark, however, m_c is not so much larger than Λ_{QCD} and the perturbative theory is at the limit of applicability. Some higher order corrections should be taken into account in order to obtain an accurate prediction for the charm production cross section.

The parton density functions (pdf) cannot be calculated in perturbation theory since they depend on the soft processes that determine the structure of the hadron as a bound state of quarks and gluons. The pdf are universal in the sense that they only depend on the initial hadron and the parton type. They can be determined experimentally and used in the calculation of any QCD process.

The partonic cross section, $d^3\hat{\sigma}_{ij}$ is the product of the invariant matrix element for the production of the quark pair in the collision of the partons i and j, and the final state phase space:

$$d^3\hat{\sigma}_{ij} = \frac{d^3\vec{k}}{2k^0(2\pi)^3} 2\pi\delta\left((p_1 + p_2 - k)^2 - m^2\right) \bar{\sum} |M_{ij}|^2 \,, \tag{2.2}$$

where p_1 and p_2 are the momenta of the incident partons ($p_1 = x_1 P_A$, $p_2 = x_2 P_B$), $|M_{ij}|^2$ is the invariant matrix element and the symbol $\bar{\sum}$ means that $|M_{ij}|^2$ is averaged over spins and colors of the initial state and summed over the spins and colors of the final state.

It is usual to express equation (2.2) in terms of the rapidity of the outgoing quarks, $y, \bar{y}$, and their transverse mass, defined as

$$\begin{aligned} m_T^2 &= p_T^2 + m^2, \\ k^0 &= m_T \cosh y, \\ k_z &= m_T \sinh y. \end{aligned} \tag{2.3}$$

The rapidity y ($\bar{y}$) represent the boost of the outgoing quark (anti-quark) from the frame where it has zero longitudinal momentum. The rapidities add under collinear boost, and the transverse mass is invariant. Thus, the set of variables (2.3) has convenient Lorenz transformation properties under boosts along the collision axis.

In terms of $y, \bar{y}$ and m_T the equation (2.2) becomes:

$$dx_1\, dx_2\, d^3\sigma_{ij} = dy\, d\bar{y}\, dp_T{}^2 \frac{\pi}{4m_T^2} \frac{1}{[1 + \cosh(y - \bar{y})]^2} \frac{1}{(4\pi^2)} \bar{\sum} |M_{ij}|^2 \,. \tag{2.4}$$

When the difference in the rapidity of the two outgoing quarks, $|y - \bar{y}|$ is large, the cross section is heavily suppressed, so the two quarks are more likely produced with similar rapidities. This is a very useful property when designing detectors that cover the forward region to detect heavy quark pairs: if one of the heavy quark hadrons is detected there is a large probability that the other heavy quark is also inside the acceptance of the detector. Therefore, there is no need to build a backwards detector to increase the acceptance of the heavy quark pair, that would be usually very expensive. This is the reason why the B-physics detectors, like LHCb or BTEV are built like a forward spectrometer.

Integrating (2.4) over the final state phase space results in:

$$\sigma(S) = \sum_{i,j} \int dx_1\, dx_2\, \hat{\sigma}_{i,j}(x_1 x_2 S, m^2, \mu^2)\, F_i^A(x_1, \mu)\, F_j^B(x_1, \mu), \tag{2.5}$$

where S is the square of total energy of the incoming hadrons in their center of mass system. The partonic integrated cross sections, $\hat{\sigma}_{ij}$, is usually written as:

$$\hat{\sigma}_{ij} = \frac{\alpha_s^2(\mu^2)}{m^2} f_{ij}\left(\rho, \frac{\mu^2}{m^2}\right), \tag{2.6}$$

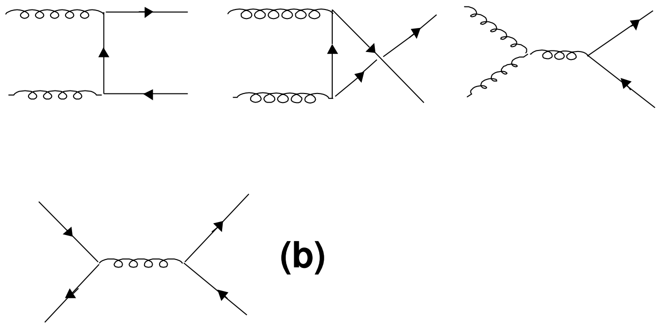

Figure 2.2: *Diagrams for the parton cross section at first order in perturbation theory.*

with

$$\rho = \frac{4m^2}{s}, \tag{2.7}$$

where s is the square of the partonic center of mass energy. The dimensionless functions f_{ij} can be expanded in a perturbative series in α_s:

$$f_{ij}(\rho, \frac{\mu^2}{m^2}) = f_{ij}^{(0)}(\rho) + g^2(\mu^2)\left[f_{ij}^{(1)}(\rho) + \bar{f}_{ij}^{(1)}(\rho)\log\left(\frac{\mu^2}{m^2}\right)\right] + O(g^4) \tag{2.8}$$

with $g^2(\mu) = 4\pi\alpha_s(\mu)$.

In what follows, the calculation of the f_{ij} functions at the first and second order in perturbation theory will be explained. The full calculation of the cross section up to order α_s^3 has been done, for instance, in [2],[3] and [4].

Leading order calculations

The process that describe the short distance cross section to leading order are the gluon fusion and the quark annhililation (see figure 2.2):

$$q + \bar{q} \to Q + \bar{Q}$$
$$g + g \to Q + \bar{Q}.$$

As it was pointed out before, in the case of the charm quark the contribution from the following terms in the perturbative series can be quite important. In fact, processes that

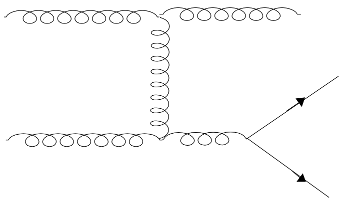

Figure 2.3: *Feynmann diagram corresponding to the process:* $g + g \rightarrow g + g \rightarrow Q + \bar{Q}$.

are in principle of order α_s^3, like the following one (illustrated in figure 2.3):

$$\begin{aligned} g + g \rightarrow & g + g \\ & \hookrightarrow Q + \bar{Q}, \end{aligned}$$

can be so important as the $g + g \rightarrow Q + \bar{Q}$, because the cross section of gluon pair production is around 100 times larger than $gg \rightarrow Q\bar{Q}$.

Computing the leading order diagrams of figure 2.2 the functions f_{ij}, that should be inserted in equation (2.6), can be obtained [1]. They are:

$$\begin{aligned} f_{q\bar{q}}^{(0)}(\rho) &= \frac{\pi\beta\rho}{27}\left[2 + \rho\right] \\ f_{gg}^{(0)}(\rho) &= \frac{\pi\beta\rho}{192}\left[\frac{1}{\beta}\left(\rho^2 + 16\rho + 16\right)\ln\left(\frac{1+\beta}{1-\beta} - 28 - 31\rho\right)\right] \\ f_{gq}^{(0)}(\rho) &= f_{g\bar{q}}^{(0)}(\rho) = 0 \end{aligned} \tag{2.9}$$

where $\beta = \sqrt{1-\rho}$, and ρ was defined in (2.7). They completely define the lowest order cross section for heavy quark production.

Next to leading order calculations

Some of the Feynmann diagrams of the next to leading order corrections for the parton-parton cross section are shown in figure 2.4. The invariant matrix elements squared, $|M_{ij}|^2$, that contribute to the leading order corrections come from the square of the matrix elements for the real emission diagrams (figure 2.4 (b)) and the interference terms between the leading order diagrams with the virtual emission ones (figure 2.4 (a)).

In the calculation of the new matrix elements some divergences will appear. The gluon loops in the virtual diagrams produce the so called ultraviolet singularities because the momentum of the gluon can take any value, including the infinity. These singularities are removed by the renormalization procedure. During this process, a new scale, μ_R, is introduced to indicate the point at which the subtraction is performed. The requirement

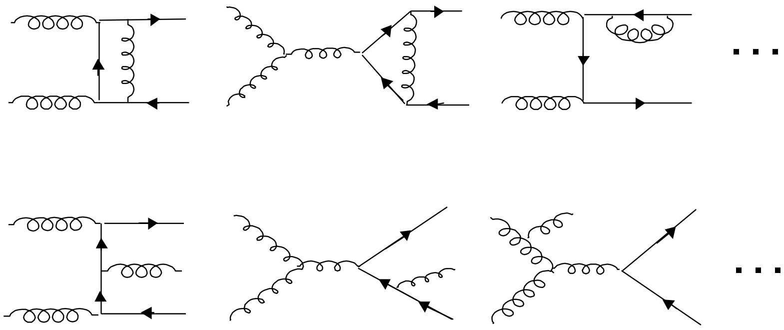

Figure 2.4: *Some of the diagrams that contribute to the quark pair production at NLO in the perturbation series, with virtual (a) and real (b) gluon emission.*

that the physical cross section should not depend on the scale μ_R leads to the equation that describes the evolution of the coupling constant:

$$\frac{d\alpha_s(\mu_R^2)}{d\ln\mu_R^2} = \beta(\alpha_s). \tag{2.10}$$

All the divergent contribution to the cross section is then absorbed in the coupling constant, α_s, that now depends on the scale at which it is evaluated: $\alpha_s(\mu_R^2)$. The equation (2.10) can be expanded in a perturbative series:

$$\frac{d\alpha_s(\mu_R^2)}{d\ln\mu_R^2} = -b_0\alpha_S^2(\mu_R) - b_1\alpha_S^3(\mu_R) + \dots\ . \tag{2.11}$$

At next to leading order, the equation (2.11) has no analytical solution. The possible approximate solutions differ by higher order corrections that are usually related to the different methods used to subtract the singularities (the renormalization schemes).

There are another kind of divergences due to collinear emission of gluons or quarks, called infrared singularities. They appear in the virtual diagrams and in the integration over the emitted parton momentum in the real emission diagrams. They are cured by factorizing out the divergences and absorbing them into the parton density functions. The resulting parton cross section, after removing the infrared singularities is the one that should be introduced in equation (2.5). This process introduces a new scale, μ_F, called the factorization scale, that plays a similar role as the renormalization scale. The consequence is that the parton density functions are no longer independent of the momentum scale μ that characterizes the hard scattering process. Their dependence on the scale is determined perturbatively by the DGLAP (Dokshitzer-Gribov-Lipatov-Altarelli-Parisi) evolution equation [5], [6]:

$$\mu^2 \frac{dF_i^A(x,\mu^2)}{d\mu^2} = \sum_j \int_x^1 \frac{dz}{z} P_{ij}\left(\alpha_S(\mu^2), z\right) F_i^A\left(\frac{x}{z}, \mu^2\right), \tag{2.12}$$

where F_i^A is the density function of the parton i inside the hadron A. Once the F_i^A are known at a certain value of μ (for instance, by measuring them experimentally), they can be evaluated at any other scale.

The P_{ij} are the Altarelli-Parisi splitting functions [6]. They depend only on the flavor of the partons i and j, but not on the incident hadron, so they are independent of the process under study. At the lowest order, $P_{ij}^0(\alpha_S, x)$ can be interpreted as the probability of finding the parton of type i in a parton of type j, carrying a fraction x of the initial parton momentum.

The scales μ_R and μ_F can be different so it is frequent to rewrite the equations (2.5), (2.6) and (2.8) in such a way that the scales can be varied independently:

$$\sigma(S) = \textstyle\sum_{i,j} \int dx_1\, dx_2\, \hat{\sigma}_{ij}(x_1 x_2 S, m^2, \mu_R, \mu_F)\, F_i^A(x_1, \mu_F)\, F_j^B(x_2, \mu_F)$$

$$\hat{\sigma}_{ij} = \frac{\alpha_s^2(\mu_R^2)}{m^2} f_{ij}(\rho, \mu_F^2, \mu_R^2, m^2)$$

$$f_{ij}(\rho, \mu_F^2, \mu_R^2, m^2) = f_{ij}^{(0)}(\rho) + g^2(\mu_R^2)\left[f_{ij}^{(1)}(\rho) + \right.$$

$$\left. + \bar{f}_{ij}^{(1)}(\rho) \log\left(\tfrac{\mu_F^2}{m^2}\right) + \tfrac{b_0}{2\pi}\, f_{ij}^{(0)}(\rho) \log\left(\tfrac{\mu_R^2}{\mu_F^2}\right)\right] + O(g^4).$$

The details of all the calculations (invariant matrix elements, renormalization, factorization, ...) go beyond the scope of this theoretical introduction. The rest of this section will focus on the phenomenological applications of those results. The interested reader can look into references [2],[3] and [4] for the order α_s^3 calculations; [5], [6] for the evolution of the parton density functions, and [7]-[13] for the calculations of the Altarelli-Parisi splitting functions at leading and next to leading order.

The theoretical predictions for the total charm and bottom production cross sections for proton-nucleon collisions, as a function of the beam energy are represented in figure 2.5 [14]. The existing experimental measurements are also shown there. The theoretical predictions were calculated for a charm mass of 1.5 GeV and a bottom mass of 4.75 GeV. The renormalization and fragmentation scales are set to: $\mu_F = 2m_c$, $\mu_R = m_c$ for the c quark and $\mu_F = \mu_R = m_b$ for the b quark. The scales can have arbitrary values but they should be set in a range close to the heavy quark mass, otherwise logarithms of the form

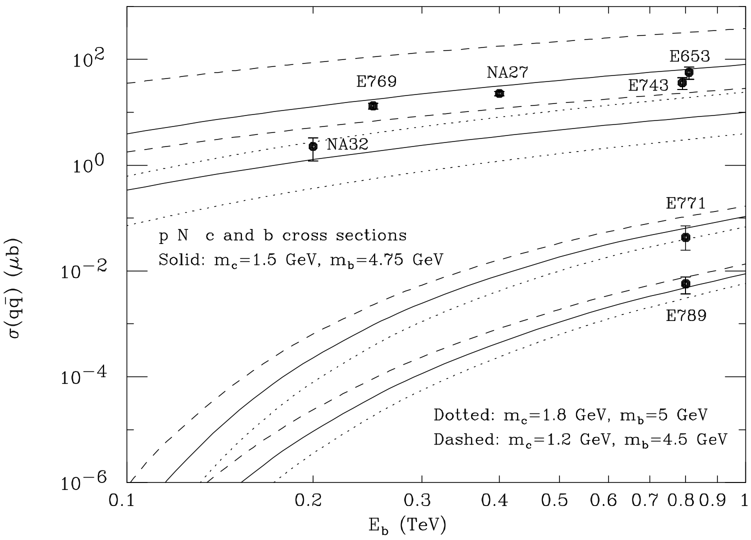

Figure 2.5: *Production cross section of $b\bar{b}$ and $c\bar{c}$ pairs in proton-nucleus collisions, as a function of the proton beam energy. The bands represent the theoretical predictions, obtained by varying the scales μ_F and μ_R in a range from $m_b/2$ to $2m_b$ for the bottom production and keeping μ_F constant ($\mu_F = 2m_c$) while varying the scale μ_R from $m_c/2$ to $2m_c$ for the charm production.*

$\log(\mu_{R,F}/m_{c,b})$ appear at all orders in perturbation theory and the expansion does not converge.

The final value of the physical cross section should not depend on μ_F and μ_R. This is exactly true only if all the terms in the perturbative expansion are included. When the series is truncated at certain order, the dependency of the cross section on the scale is of higher order in the perturbative series. The lower limit of the error due to the uncalculated terms can be estimated by varying the scales μ_F and μ_R and determining the induced variation in the cross section. The error bands shown in figure 2.5 correspond to the variation of the scales in the range between $2m_q$ and $m_q/2$. For the charm quark μ_F was kept constant because the parametrization used for the parton densities is known only for $Q^2 > 5GeV^2$. Three sets of bands are shown, corresponding to different values of the charm and bottom masses, as it is indicated on the plot.

From figure 2.5 one can see that the experimental results are in good agreement with the theoretical expectations, considering the big errors of the predictions. The theoretical uncertainties can be reduced by going to the next order in the perturbation series, but due to the extreme difficulty of these calculations, it has not been done yet. Some improvements were achieved in certain regions of the phase space by summing enhanced contributions at all orders in perturbation theory. At very high energy, for example, terms of the form $\sigma^0 \times [\alpha_S \log S/m^2]^n$ appear. When the energy is much larger than the mass of the quark ($S \gg m^2$) these terms diverge and the perturbation theory is not usable unless these contributions are summed at all orders in the perturbative expansion. This problem can be important at the bottom production at the Tevatron or at the LHC. Close to the energy threshold for production of the heavy quark pairs, another kind of logarithms arise: $\sigma^0 \times [\alpha_S \log^2 \Delta_{thr}]^n$, where Δ_{thr} is some kind of measurement of the energy distance from the threshold. These kind of terms can be important for the production of b quarks at HERA-B, and for the top quark at the Tevatron, for instance.

Resummation of threshold effects up to the next-to-leading order was studied for instance in [15] and [16]. For the high energy logarithms, the resummation was calculated only to next to leading logarithmic level [17], [18], [19].

2.2 Hadronization

After been created, the heavy quarks are moving with opposite momentum, in their center of mass system. The strong coupling constant, α_S, becomes large when the separation between the heavy quark pair increases. At certain point the quarks transform into hadrons, with a process that is not calculated in perturbation theory, called hadronization or fragmentation. The factorization theorem states that the cross section for the production of a hadron H in the collision of two hadrons, A and B, with momenta P_A and P_B (as in figure 2.1), can be expresed as [20]:

$$\begin{aligned} \frac{E\, d\sigma^H}{dk} = \sum_{ijl} \int & \frac{E'\, d^3\hat{\sigma}_{ij,l}(x_1 P_A, x_2 P_B, k', \mu_F, \mu)}{d^3 k'} \\ & \times F_i^A(x_1, \mu_F)\, F_j^B(x_2, \mu_F) D_l^{(H)}(z, \mu)\, dx_1\, dx_2\, \frac{dz}{z^2} \end{aligned} \tag{2.13}$$

where $k' = k/z$ and k is the momentum of the outgoing quark; μ_F is the factorization scale and μ represents the scale at which the fragmentation function is evaluated; $d^3\hat{\sigma}_{ij,l}$ is the partonic cross section for producing the parton l in the collision of partons i and j defined as in (2.2); the function F_i^A (F_j^B) is the structure function for finding the parton i (j) in the hadron A (B) with a momentum fraction x_1 (x_2) and $D_l^{(H)}(z, \mu)$ is the fragmentation function for producing the hadron H from the parton l.

The fragmentation functions $D_l^{(H)}(z,\mu)$ are independent of the process under study and they only depend on the hadron H and the parton l. They cannot be calculated in perturbative QCD but, in the same way that happened with the parton density functions, its evolution is known and can be described using the Altarelli-Parisi splitting functions:

$$\frac{d}{d\log\mu^2} D_l^{(H)}(z,\mu) = \frac{\alpha_S(\mu)}{2\pi}\int_z^1 P_{jl}(x)\, D_j^{(H)}(z/x)\,\frac{dx}{x} \tag{2.14}$$

At the leading order, the splitting functions, P_{jl}, are the same as those used for the parton density functions, but at higher orders they are different [21]. The fragmentation functions $D_l^{(H)}$ are usually measured experimentally at a certain momentum scale and their value at other scales is obtained by applying the equation (2.14).

In the case of a heavy quark, the heavy flavored hadron carries a large fraction of the heavy quark momentum. Thus, the fragmentation function $D_l^{(H)}$ is expected to be peaked at one. It is usual to parametrize it with the Peterson function [22]:

$$D(z;\mu) = \frac{1}{z}\left(1-\frac{1}{z}-\frac{\epsilon}{1-z}\right)^{-2}, \tag{2.15}$$

where the parameter ϵ is obtained from the fits to the experimental data.

With these ingredients, the heavy flavored hadron production cross section can be calculated (see, for instance [23]).

There are many experimental measurements of single inclusive charmed hadron distributions, for $\pi-N$ [24]- [31] and $p-N$ collisions [32]-[36], that do not perfectly agree with the theoretical expectations. The differential cross sections for heavy flavored hadrons are expected to be more dependent on non-perturbative effects that the total cross sections for heavy quark production. Therefore, the discrepancies may help to distinguish the non-perturbative effects that are more important in the charm hadroproduction or they may indicate that some of the theoretical assumptions (like the fragmentation model) are not correct.

One example of such discrepancies is the ratio between the D^+ and the D^0 production cross section, that will be presented in the following section.

2.3 D^+ to D^0 production ratio

The D^+ and D^0 production cross sections can be calculated with the formalism developed in the previous sections. However, with a simple symmetry argument, based on the isospin symmetry of the strong interaction, a prediction for the D^+ to D^0 production cross section ratio [14] can be obtained. The D^+ and D^0 are two pseudo-scalar mesons (with spin $S=0$) belonging to the same isospin multiplet, with $I=1/2$ and $I_3=+1/2$ and $I_3=-1/2$,

	$q\bar{q}\prime$	I	I_3	S	L	J^P
D^+	$c\bar{d}$	1/2	+1/2	0	0	0^-
D^0	$c\bar{u}$	1/2	−1/2	0	0	0^-
D^{*+}	$c\bar{d}$	1/2	+1/2	1	0	1^-
D^{*0}	$c\bar{u}$	1/2	−1/2	1	0	1^-

Table 2.1: *Quantum numbers assigned to the D mesons: isospin, third component of the isospin, spin, angular momentum and parity.*

respectively. The D^{*+} and D^{*0} are the corresponding vector mesons with the same quark content and the same isospin, but with spin $S = 1$. The relevant quantum numbers for this mesons are summarized in table 2.1.

The fraction of D^+ (D^0) mesons produced in the collision of the heavy hadrons can be calculated as the sum of the D^+ (D^0) directly produced in the collision and the ones that came from the decay of the D^* resonances. Then, the ratio between the total number of produced D^+ and D^0's can be obtained as:

$$R = \frac{\sigma_{D^+}}{\sigma_{D^0}} = \frac{\sigma^d_{D^+} + \sigma^d_{D^{*+}} \cdot BR(D^{*+} \to D^+)}{\sigma^d_{D^0} + \sigma^d_{D^{*0}} \cdot BR(D^{*0} \to D^0) + \sigma^d_{D^{*+}} \cdot BR(D^{*+} \to D^0)} \tag{2.16}$$

where $\sigma^d_{D^i}$, $i = +, 0, *+, *0$, is the direct production cross section of the hadron D^i and $BR(D^{*i} \to D^j)$ is the probability that the hadron D^{*i} decays to D^j, with $i, j = +, 0$. The cross section for producing the hadron D^i is the sum of the cross sections for each of the polarization states of the D^i meson. As the spin of the vector mesons is $S = 1$, the total number of polarization states for the resonances D^* and the D^{*+} is 3 times larger than for the pseudo-scalar mesons, that have $S = 0$. Now, considering isospin invariance in the transitions $c \to D*$ and $c \to D$, the probability of producing a D^+, a D^0, a D^* or a D^{*+} directly in the collision of the two initial hadrons, in a particular polarization state, is approximately the same. Therefore:

$$\begin{aligned} &\sigma^d_{D^{*+}} \simeq \sigma^d_{D^{*0}}, \\ &\sigma^d_{D^+} \simeq \sigma^d_{D^0} \\ &\text{and } \sigma^{\mathrm{d}}_{\mathrm{D}^*} \simeq 3\sigma^{\mathrm{d}}_{\mathrm{D}}. \end{aligned} \tag{2.17}$$

Considering the branching ratios of the following transitions [37]:

- $D^{*0} \to D^0$: 100%,
- $D^{*+} \to D^+$: 32.3 %,

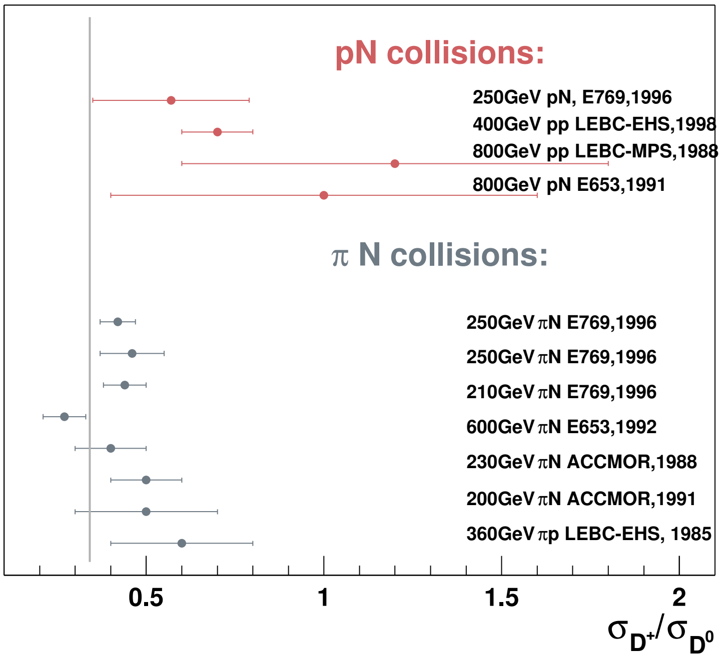

Figure 2.6: *Experimental measurements of the D^+ to D^0 production cross section ratio. The theoretical prediction is shown with a grey line.*

- $D^{*+} \to D^0$: 67.7 %,

the final value of the ratio will be:

$$R = \frac{\sigma_{D^+}}{\sigma_{D^0}} \simeq 0.33 \tag{2.18}$$

It is important to notice that this symmetry argument should hold either for the $\pi - N$ or for the $p - N$ collisions because it affects only to the hadronization of the final state charm quark.

A more accurate prediction can be obtained with the help of Monte Carlo programs that correctly treat all the production and hadronization effects described in the previous sections. The results obtained with the MC program HERWIG [38],[14] predict also the same ratio in the case of $\pi - N$ and $p - N$ collisions, with a value similar to (2.18).

The existing experimental results for this ratio are shown in figure 2.6 [39]. They were calculated by dividing the published values of the two cross sections, that were measured separately. The results in $\pi - N$ collisions are quite close to the theoretical prediction (2.18). On the contrary, in proton-nucleus collisions a larger ratio is obtained. For some of the measurements, obtained at higher proton beam energies, the measured ratio is close to one. For the latest results, that have also smaller errors, the ratio is closer to the average for $\pi - N$ collisions. There is no reasonable explanations why the $\pi - N$ and $p - N$ experiments should give different results.

The measurements for the proton-nucleus experiments were obtained with small statistics and have, as a consequence, large errors. More measurements in this field will help to understand if this difference is real, and there are, in fact, unknown effects in the production of heavy flavored hadrons.

The aim of this thesis is to obtain a new measurement of the D^+ to D^0 production cross section ratio in proton-nucleus collisions at 920 GeV, using the HERA-B detector.

Chapter 3

The HERA-B experiment

3.1 Introduction

HERA-B is a fixed target experiment designed to measure CP violation in the B meson system, specifically in the golden plated decay, $B_d^0 \rightarrow J/\Psi K_s^0$ [40]. Using two target stations in the halo of the 920 GeV proton beam of the HERA storage ring, the spectrometer was designed to cope with very high interaction rates to separate the golden B_d^0 decays, that occur roughly once every 10^{11} proton-nucleus collisions, and reach very high precision in the measurement of the CP violation parameter, $\sin(2\beta)$. This challenging physics program imposed strong requirements in the trigger, in the data acquisition system and in the detector design.

The detector is a forward spectrometer with a very wide angular coverage, from 10 to 200 mrad in the bending plane of the magnet and from 10 to 160 mrad in the non-bending plane (see the schematic overview in figure 3.1). This angular coverage is equivalent to around 90% of the solid angle in the center of mass system.

The target consist of two stations of 4 wires each, that can be displaced to the halo of the proton beam till the desired interaction rate is reached. Downstream from the target, the Vertex Detector System (VDS) is placed. It was designed to separate with very high precision the decay point of the B_d^0 meson from the main interaction point. Behind the VDS, the tracking system starts. It is composed of two different subdetectors with different granularities to keep the hit occupancy below 20%. In the inner region, where particle density is higher, a micro-strip gaseous detector is used (the inner tracker, ITR), with an angular coverage between 10 and 100 mrad. The outer region is covered with honeycomb drift chambers (the outer tracker, OTR).

The tracking system consist of 13 stations composed of several detector layers, placed before, inside and after the magnet, in order to track the charged particles and get an

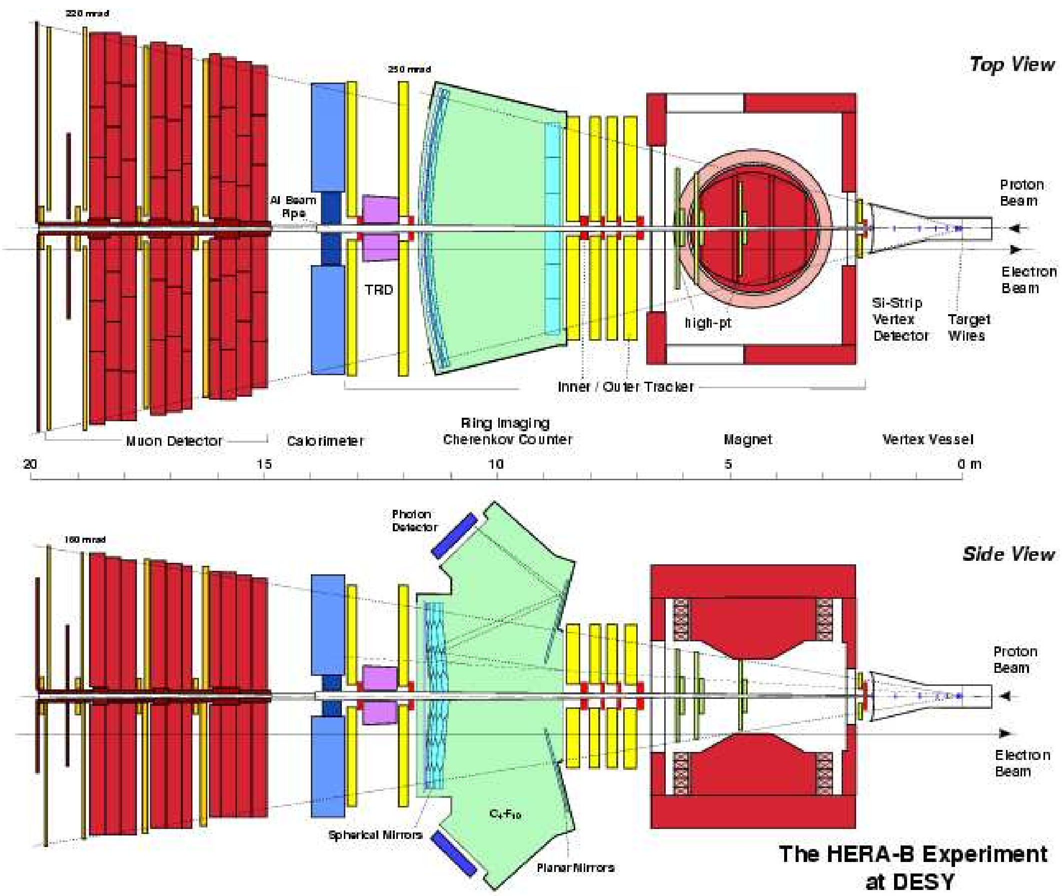

Figure 3.1: *Top- (above) and side view (below) of the HERA-B spectrometer.*

accurate determination of the momentum by measuring the bending angle in the magnet. The HERA-B magnet provides a magnetic field with a maximum intensity of 0.8 T and a field integral of 2.2 Tm.

The particle identification is provided by three different subdetectors: the ring imaging Čerenkov detector (RICH), the electromagnetic calorimeter (ECAL) and the muon chambers (MUON). The RICH was designed to separate kaons from pions in a wide range of momentum, between 10 and 60 GeV, in order to tag the flavor of the B decaying hadron. The ECAL, placed after the tracking system, provides electron and photon identification. Finally, the muons are identified by the muon system, made of several layers of concrete blocks and detectors, with different technologies depending on the distance to the beam center.

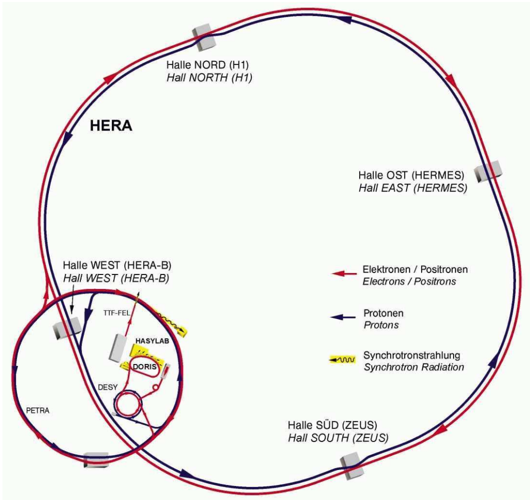

Figure 3.2: *Schematic view of the HERA storage ring with its preaccelerators, at DESY (Hamburg).*

In addition to this, a transition radiation detector (TRD) is placed between the last two tracking chambers with the purpose of providing an extra electron identification at small angles, in a range between 1 and 100 GeV.

To provide fast detection of hadrons with a high transverse momentum at the trigger level, three additional chambers are placed inside the magnet region (high-p_T). They have different technologies for the inner and outer regions (gas-pixel chambers in the inner part and straw tubes with a pad readout in the outer part).

Both, the high-p_T chambers and the TRD detector, were not used during the 2000 run period due to different reasons: the TRD was missing the electronic readout and the high-p_T did not have the interface to the trigger system.

In the next section the detector characteristics are explained in more detail, with special emphasis on the elements that are important for the analysis presented in this thesis. The trigger and data acquisition systems are described in section 3.3. The last part of this chapter is dedicated to the reconstruction chain of the data.

3.2 The HERA-B detector

3.2.1 Beam and target

The HERA-B spectrometer is placed in one of the 4 experimental halls of the HERA storage ring, at the DESY laboratory, in Hamburg. HERA is an storage ring of 6336 m

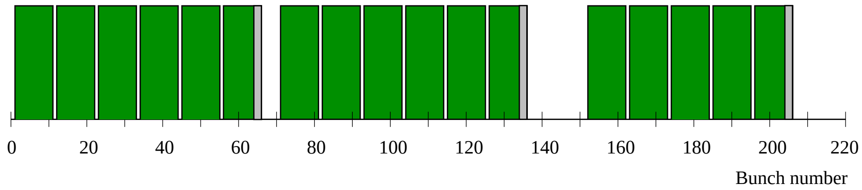

Figure 3.3: *Bunch structure of the HERA proton beam.*

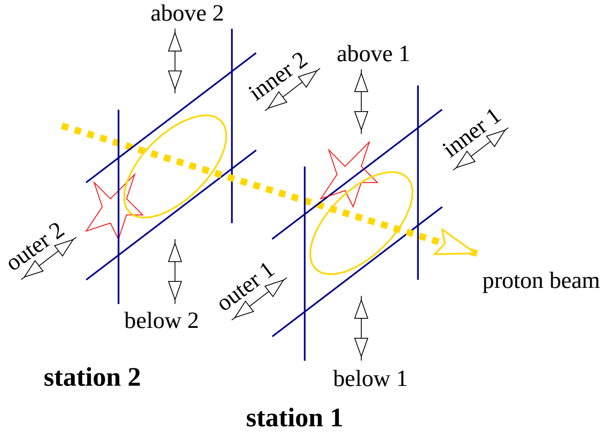

Figure 3.4: *Target configuration in the HERA-B experiment.*

of circumference, that can accelerate protons to 920 GeV energy and positrons (or electrons) to 30 GeV (figure 3.2). The positron and proton beams, that circulate in opposite directions, collide in two points, where the experiments H1 and ZEUS are installed. There are two other experimental halls, where HERMES and HERA-B are installed. HERMES uses only the longitudinal polarized positron (or electron) beam to collide with a polarized target, and HERA-B uses the proton beam only.

The HERA proton beam is structured in 220 bunches that are 30 cm long, separated by nearly 3 m in between. Only 180 bunches are filled. Due to the fact that the preaccelarator, DORIS III, has space for 10 bunches and PETRA for 60 bunches the structure of the HERA proton beam has the form that appears in figure 3.3, with some empty bunches between each block.

HERA-B uses the halo of the proton beam to provoke collisions with a fixed target[1].

[1]Since HERA was running in cleaner conditions than originally planned, the target was frequently touching the core of the beam, and not only the halo.

The halo is populated by drift protons that will be eventually eliminated by the HERA collimators. To reach the desired interaction rate of 40 MHz, 8 wires are installed, divided in two stations of 4 wires each, following the scheme shown in figure 3.4. There is a separation of about 4 cm between the two stations. Each wire can be individually displaced closer or further from the beam center till the desired interaction rate is reached. The interaction rate is monitored by four scintillator counters, placed behind the RICH detector. If any fluctuation in the rate appears, the wires are moved automatically to compensate it, keeping a stable rate during the target operation. The typical distance from the wires to the beam center is around 3 to 5 times the beam width[2]. The interaction rate should be equally distributed between the wires to avoid multiple interactions in the same wire at the same time, that would be difficult to separate. To achieve this each wire is equipped with a charge integrator that measures the δ electrons induced by the protons crossing the nucleus inside the wire material and provides a good relative measurement of the interaction rate in that wire. A monitoring program controls the individual rates and automatically move the targets in or out from the halo to reach equal rates.

During the 2000 data taking the target wires were typically ribbons 500 μm along the beam axis and 50 μm in the radial direction. The wires were made of four different materials (aluminum, tungsten, titanium and carbon) allowing studies of proton-nucleus production cross sections as a function of the nucleus material. For the 2002 run, round wires made of different materials were installed.

3.2.2 Silicon vertex detector

The vertex detector was designed to provide a good separation between the B_d^0 decay point and the primary interaction, as well as good resolution in the impact parameter of the B tagging particles.

The VDS is composed of 64 double-sided micro-strip detectors, distributed in 8 stations, called superlayers (SLs), covering a region of around 2 m from the target wire along the beam direction, with an angular range of 10-250 mrad. Each SL is formed by four modules of 2 double-sided detectors, arranged in 4 quadrants (see figure 3.5 (b)). The micro-strips in each side of the same layer are orthogonal, ensuring a good spatial resolution in both vertical and horizontal directions. The detectors are tilted $\pm 2.5^o$ with respect to the vertical direction.

The resolution in the vertex detector is dominated by multiple scattering. To minimize it, the first seven superlayers are in the vacuum, inside a vessel that is part of the beam pipe. The eighth SL is just in front of the magnet, behind the exit window of the vessel. To ensure good acceptance for the tracks with small angles, the VDS should be placed

[2]The beam width is around 400 μm.

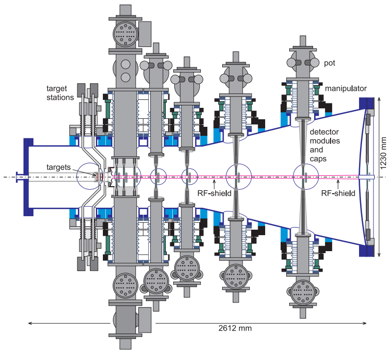

(a)

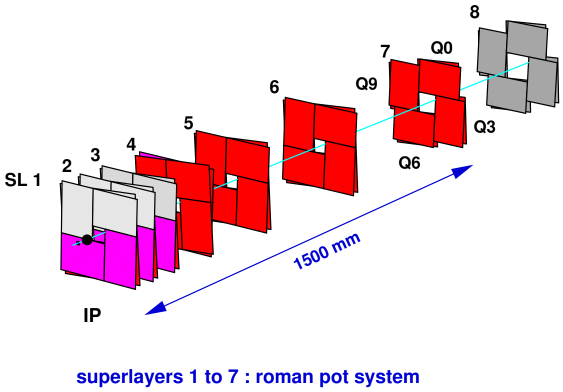

(b)

Figure 3.5: *(a) Longitudinal view of the vertex detector vessel where the target stations and the Roman pots are installed. (b) Spatial distribution of the detector planes.*

10 mm far from the beam. During injection the fluctuations in the position of the proton beam could seriously damage the silicon detector. To protect the detector, each module is contained in a Roman pot, equipped with a system of motors to move the modules away from the beam to a safe position when the accelerator is in injection mode (see figure 3.5 (a) for an schematic view of the vessel and the motors system). The precision of these motors to reach always the same position is close to 1 μm, so the detector does not need a new alignment each time it is moved. During the 2000 data taking period the VDS planes were kept 15 mm far from the beam, resulting in a smaller angular acceptance (between 15 and 250 mrad). The final hit resolution achieved was 12 μm, with an efficiency of 98%. The resolution on the impact parameter of tracks with momentum larger than 50 GeV was 35 μm. The primary vertex resolutions were $\sim$500 μm in the z direction[3] and $\sim$50 μm in x and y.

[3] The HERA-B coordinate system has the z axis along the proton beam direction. The x coordinate is along the horizontal direction, with the positive side directed to the center of the accelerator. The y coordinate is the vertical one.

3.2.3 Tracker system

The HERA-B main tracker is composed of two subdetectors: one that covers the region closer to the beam (ITR), where the particle flux is higher and another one for the outer region (OTR). Both of them are divided in 13 superlayers (SL). The first SL is before the magnet, just at the end of the VDS vessel, to ensure that each track inside the acceptance of the tracker has a point measured before the magnet. There are 6 OTR and 3 ITR superlayers inside the magnetic field, to ensure that the K_S^0 from the golden decay is well reconstructed[4]. The next four superlayers are behind the magnet, and they are called pattern chambers because they are used at the pattern recognition level in the track reconstruction. The last two chambers, placed between the RICH and the ECAL, are used in the first level trigger for a fast tracking, together with the first and the last SL of the pattern region, confirming the signals coming from the muon or ECAL pretriggers. They have double layers of detectors to fulfill the requirements of the trigger.

Inner tracker

The innermost part of the main tracking system is made of Micro-strip Gaseous Chambers (MSGC). The principle of the MSGC's is shown in figure 3.6: when a charged particle traverses the detector, ionizes the electrons from the gas, that drift to the anode strips. In order to reduce the sparking probability, a Gas Electron Multiplier (GEM) foil was introduced. The GEM produces an extra amplification of the signal while keeping lower cathode voltages.

The ITR was designed to support high radiation levels (up to 1 Mrad/year over several years) and to cope with a very high particle flux while keeping the occupancy below 5% to permit efficient tracking and reach a spatial resolution of 100 μm in the bending direction of the magnet. The MSGC strips are oriented with angles of $0^o, \pm 5^o$ with respect to the vertical axis, with a pitch distance of 300 μm, that result in a hit resolution of 90 μm. They produce a very precise measurement of the horizontal coordinate, needed for a good momentum resolution.

During the 2000 data taking period, the ITR was still in an early commissioning phase. It was not fully operational till the last two months and it was never used at the trigger level. The data used in this analysis was taken at the end of the run period, when the ITR was already working in stable conditions. The design resolution was not achieved (it arrived to 150 μm). The hit efficiencies were up to 90%-97%.

[4]These chambers were removed for the 2002 setup.

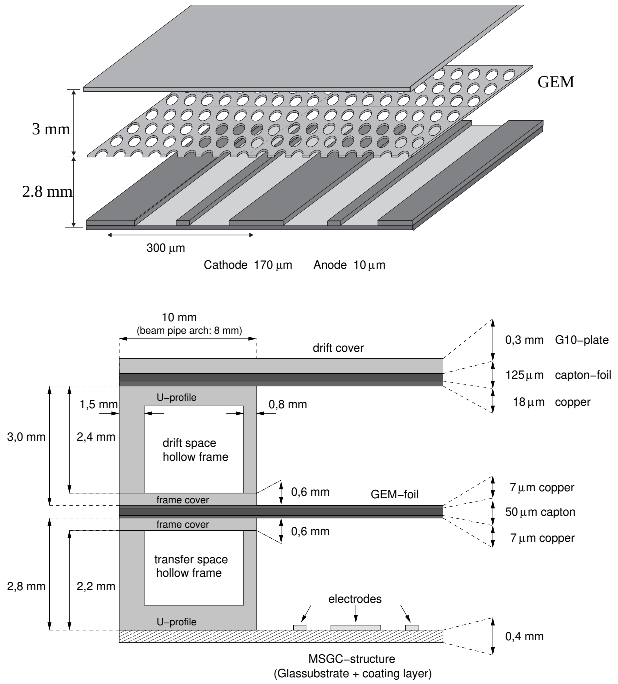

Figure 3.6: *Schematic view of the GEM Micro Strip Gas Chambers that form the ITR system.*

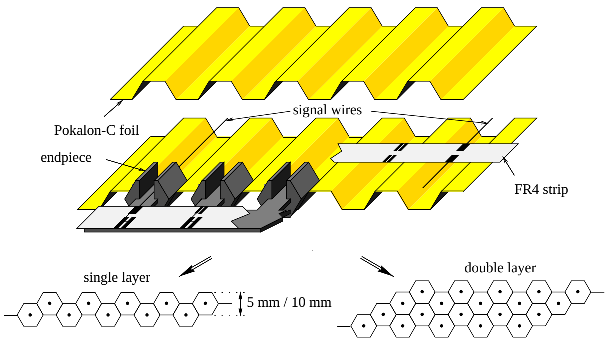

Figure 3.7: *Scheme of the honeycomb structure of a single and a double layer of the OTR detector.*

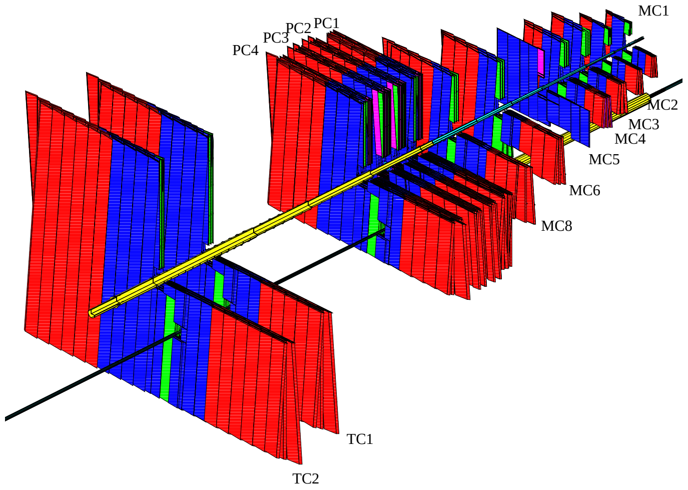

Figure 3.8: *Spatial view of the OTR modules. The upper right quadrant was deleted.*

Outer tracker

The HERA-B outer tracker is made of honeycomb drift tubes (see figure 3.7) arranged in single and double layers (the later ones in the trigger chambers). As in the inner tracker, the wires are oriented with angles of $0^o, \pm 5^o$ with respect to the vertical axis. A superlayer is formed by 3 layers in the magnet area, 3 double layers in the trigger chambers and 6 layers in the pattern chambers. They are divided in modules of different sizes, as it is shown in figure 3.8. Each layer is divided in two halves that can be displaced to allow the access to the inner parts of the detector.

The acceptance of the OTR cover the region from 25 cm till 3 m from the beam axis, approximately. The modules that are closer to the beam pipe have 5 mm cells while the outer ones have smaller granularity (10 mm cells). When a charged particle crosses the tube, it ionizes the electrons from the gas, that drift to the wire and are collected. The OTR is equipped with Time to Digital Converters (TDC) that measure, for every bunch crossing, the time when the avalanche of electrons reached the anode. Thus, the hit resolution is better than the cell size and can reach 200 μm. During the 2000 run the hit resolution was 350 μm and the efficiency was also considerably lower than expected (90% to 95% instead of the 98% design value) due to the fact that higher readout thresholds and lower gas gains had to be used to avoid problems with high voltage. A non-perfect alignment and calibration also contributed.

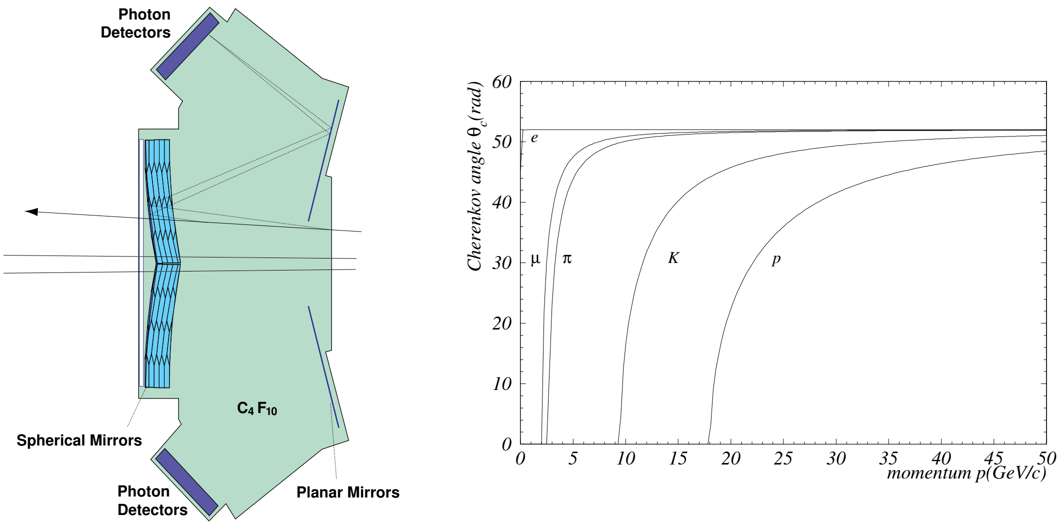

(a) (b)

Figure 3.9: *(a) Schematic view of the Ring Imaging Čerenkov detector. (b) Čerenkov angle as a function of the particle momentum, for electrons, muons, pions, protons and kaons.*

3.2.4 RICH: the Ring Imaging Čerenkov detector

The RICH detector was designed to separate efficiently kaons from pions in a wide range of momentum (between 3 and 60 GeV) to be used in the tagging of the B_d^0 flavor. It uses the Čerenkov effect to determine the speed of the particle: when a particle crosses a medium with a speed higher than the speed of light in that medium it produces a cone of light with an opening angle that increases with the speed of the particle. Knowing the momentum from the tracking chambers, the mass of the particle, and therefore its identity, can be determined.

The HERA-B RICH uses freon (C_4F_{10}) as a radiator gas due to its low Čerenkov threshold, ensuring good identification of particles even at low momentum. The Čerenkov angle as a function of the particle momentum is shown in figure 3.9 (b) for kaons, protons, pions, electrons and muons. The momentum thresholds, at which the particles start to radiate, are around 2.6 GeV for pions, 9.6 GeV for kaons and 17.8 GeV for protons.

The gas is contained in a big vessel made of stainless steel. The particles entry and exit window are made of 1 mm thick aluminum plates. To keep the photon detectors far from the acceptance region of the detector two systems of mirrors are arranged as it is shown in figure 3.9 (a). First, the spherical mirrors, tilted 9^o from the horizontal line, transform he cones into rings that are reflected later in planar mirrors and projected out from the detector acceptance. The photon detector is composed of ~ 1500 photomultipliers of 16

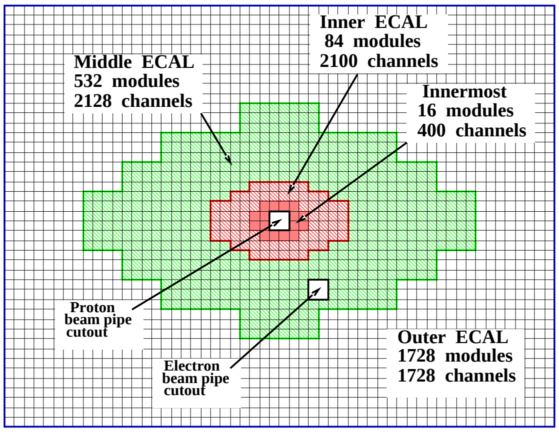

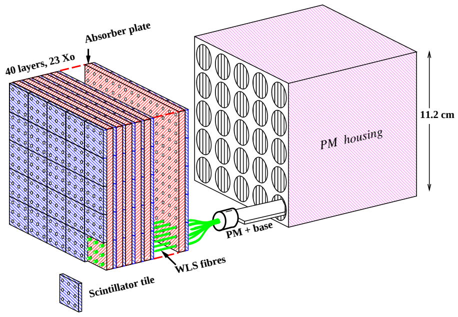

Figure 3.10: *Left: ECAL structure, divided in three regions of different granularity, covering the whole acceptance region. Right: Scheme of the sandwich structure of a module in the inner region.*

channels each and ~ 700 more with 4 channels each. The later ones are placed in the outermost region of the detector, where the occupancy is lower.

The RICH design performance was fully reached, with a single hit resolution of 0.7 mrad [41]. It provides 4σ separation for kaons and pions between 12 and 55 GeV, kaons and protons between 23 and 85 GeV and electrons from pions between 3 and 15 GeV. It has been running reliably in stable conditions for the whole data taking period.

3.2.5 Electromagnetic calorimeter

The electromagnetic calorimeter (ECAL) was designed to separate electrons and photons from hadrons. Photons are seen as a particle that has no track but it leaves an energy deposition in the ECAL. Electrons are particles that leave all their energy in the calorimeter, i.e., the ratio between the energy deposited in the ECAL and the momentum measured with the tracker is approximately one ($E/P \sim 1$). Hadrons leave just a small fraction of their energy there, so $E/P \ll 1$. The ECAL is also used at the trigger level to detect the clusters produced by the electrons from the J/Ψ decay and to send the signal to the first level trigger that will start the track search.

The calorimeter is divided in 2344 modules that are formed by several layers of sampling scintillators sandwiched with absorber materials. All the modules have the same transverse dimensions, $11.2 \times 11.2\,\mathrm{cm}^2$. When a particle traverses the absorbers it produces a shower of electrons, positrons and photons, proportional to its energy. The shower is detected by the scintillator material and the light collected there is transported by wavelength-shifting optical fibers till the photomultipliers that are placed behind (shashlik structure), as it is

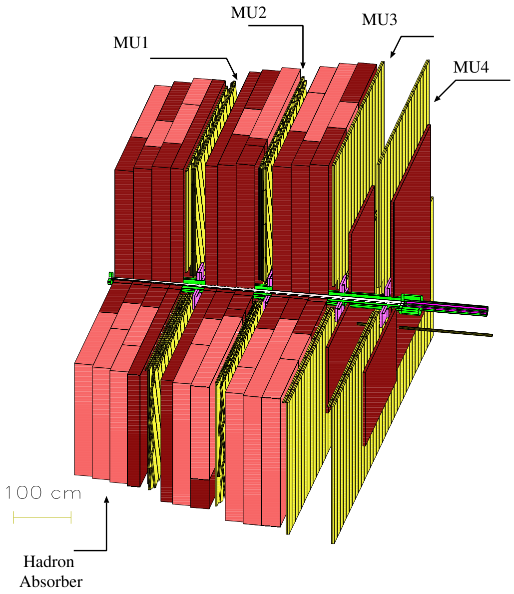

Figure 3.11: *Perspective view of the muon detector.*

shown in figure 3.10(b).

The ECAL is divided in three regions with different granularity that cover the whole acceptance of the detector. In the inner part, each module consists of 25 cells each and tungsten as absorber, to keep the shower confined to few cells laterally. In the middle and outer region the absorber is lead, and each module has 4 and 1 cells, respectively.

The measured energy resolution during the 2000 run [42] in the inner part was $\sigma(E)/E = 22.5\%/E \oplus 1.7\%$ in the range from 12 to 60 GeV, close to the design values. The spatial resolution was 0.2 cm.

3.2.6 Muon chambers

The muon system was designed to separate muons from hadrons in a wide range of momentum (from few GeV to 200 GeV) and to provide the starting signal for the trigger. It covers the full acceptance of the detector and it should have a very high hit efficiency (around 99%) and fast response in order to fulfill the requirements of the trigger system. The punch-through probability (muons coming from hadronic showers in the absorber) should be lower than 5×10^{-3} for hadrons up to 100 GeV.

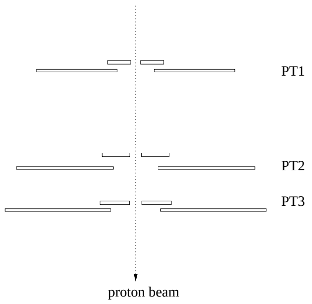

Figure 3.12: *Layout of the high* $\mathrm{p_T}$ *chambers in the HERA-B magnet region.*

To achieve the design requirements, three superlayers of detectors are arranged in between absorber blocks, as it is shown in figure 3.11. There is an additional superlayer at the end to ensure a good measurement of the track directions at the end of the absorber. Each block of absorber has a thickness of about 1 m. The inner region is made of iron. It reaches, together with the ECAL, around 20 interaction lengths. Only muons with more than 4.5 GeV momentum can pass through it. In the outer region, where the spectrum of the muon momentum is softer, the absorber is made of concrete loaded with iron, in order to reduce costs.

The detector planes are made with three different technologies, depending on the position and purpose of the chamber. The first two chambers, used basically in the offline analysis[5], are made of proportional tube chambers, with stereo-angles of $0^o, \pm 20^o$. The inner region is covered with gas pixel chambers to cope with the higher occupancies. The last two chambers, used in the trigger and in the offline analysis, consist of a 0^o layer of pad chambers, with both pad and tubes readouts, and a gas pixel chambers in the central region.

3.2.7 The high-$\mathrm{p_T}$ system

The high-$\mathrm{p_T}$ chambers are needed in HERA-B at the trigger level, to detect hight-$\mathrm{p_T}$ hadrons coming from the decay of a beauty hadron, like $B_d^0 \to \pi^+\pi^-$.

The system consists of three planes of detectors, placed in the middle of the magnet, with two different technologies for the inner and the outer part, distributed as the scheme in figure 3.12 indicates. The inner high-$\mathrm{p_T}$ is made of gas-pixel chambers, similar to those used in the muon chambers, with around 12000 readout channels. The outer high-$\mathrm{p_T}$ is made of straw tubes with a pad readout. The electron shower produced in the straws

[5]The first one participates also on the trigger.

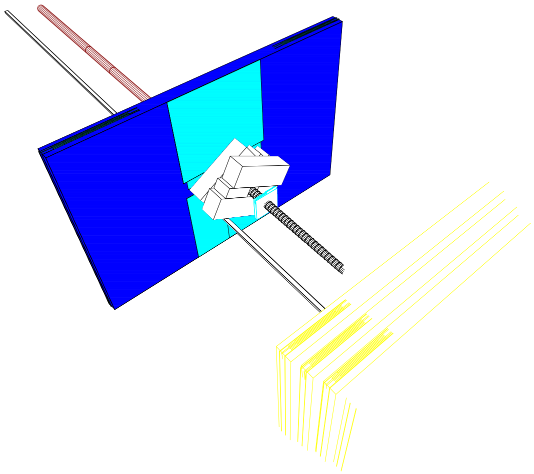

Figure 3.13: *Schematic view of the TRD detector in the space. The RICH and the tracking plane behind it were removed. The last tracking plane is shown with dark color. The beam goes from the lower right corner to the upper left corner.*

when a hadron crosses the tube, induce a mirror signal in the pads, that is read out. The straw tubes do not have any readout.

The high-p_T chambers have a projective segmentation to detect the high-p_T hadrons that leave a different hit pattern than the background particles coming from the main interaction.

The commissioning of the high-p_T system was not finished during the 2000 data taking period [42]. For that reason, they were not used for the data taking.

3.2.8 Transition Radiation Detector

A transition radiation detector (TRD) was designed to improve the identification of electrons in the region close to the beam pipe (the inner region of the ECAL). It is placed between the last tracking chambers, in front of the ECAL (see figure 3.13 for an schematic view). The TRD measures the radiation emitted by the electrons when they cross the separation surface between two media with different dielectric constants. An extra hadron/electron separation factor of 25 is provided, with an efficiency of 95% for the electrons. Additionally it can also be used for tracking.

It is made of straw proportional counters embedded in the polypropylene fiber radiator.

The TRD was installed during the 2000 year but the readout electronics was missing, so it has never been used in the data taking.

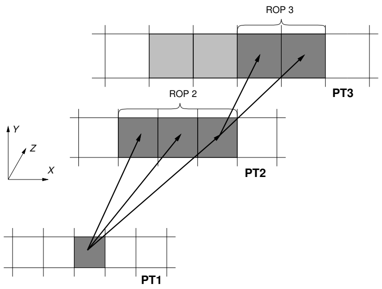

Figure 3.14: *High* p_T *coincidence scheme used at the pretrigger level.*

3.3 Trigger and data acquisition system

The HERA-B Trigger

In order to get enough statistics to measure CP violation in the golden decay channel with good accuracy, HERA-B was designed to run with an interaction rate of 40 MHz, that is equivalent to 4 inelastic interactions per bunch crossing. The 520000 channels of the detector produce 4.7 TBytes/s of data. The impossibility of processing that rate of data, together with the fact that the interesting decays (the golden B_d^0 decay) happen only once every 10^{11} interactions, forced the experiment to use a very selective trigger.

The trigger was designed to work in four levels with different reduction factors, that are indicated in table 3.1. The first step is the **pretrigger** signal that may come from three different systems: the ECAL, the MUON or the high-p_T chambers. The first two systems search for lepton candidates, while the third one searches for hadrons with high transverse momentum. They can all work in parallel. The ECAL pretrigger signal consists in a high energy cluster with transverse energy ($E_t = E * \sqrt{(x^2 + y^2)/z^2}$) larger than a certain threshold. The MUON pretrigger detect pad coincidences in the last two chambers and the high p_T searches for a 3 pad coincidence with a certain pattern (see figure 3.14). No rejection of events is applied at the pretrigger level.

Using the pretrigger signal as a starting point, the **First Level Trigger** traces back the tracks, requiring a hit in each of the detector layers of the tracking chambers used for trigger (the two trigger superlayers plus the first and the last SL in the pattern region that sum 12 double layers in total). The hit efficiency of the tracking detectors is therefore crucial to reach a good efficiency of the FLT. The tracking algorithm, performed in the Track Finding Units (TFUs) is based in regions of interest (RoI's), i.e., in each layer only a small region of the detector is used to find the hits, depending on the hits found in the

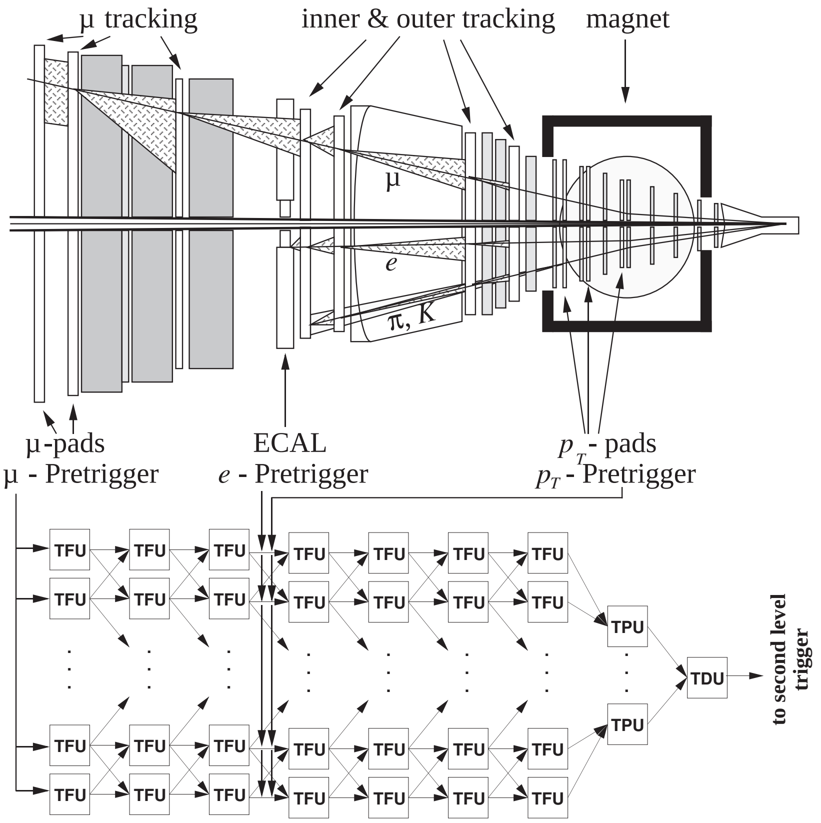

Figure 3.15: *Scheme of the FLT algorithm.*

previous layer (see figure 3.15). This method allows to process very fast a big amount of data. The kinematic parameters and the invariant mass of the track pairs are determined in the Track Parameter Unit (TPU) and the Trigger Decision Unit (TDU). The trigger signal is then distributed by the Fast Control System (FCS) that transfers the buffered data from the detector front end electronics to the Second Level Buffer (SLB).

The FLT was not completely commissioned during the 2000 run period and its performance was well under the design values [42].

The **Second Level Trigger** (SLT) is equipped with a farm of 240 PC's, to further refine the FLT tracking. Each track candidate is propagated through the magnet to the VDS, using a fast algorithm to fit the tracks and refine the accuracy of their parameters.

	input rate	reduction factor	execution time
FLT	10 MHz	200	$< 12\mu$s
SLT	50 KHz	100	3.8 ms
TLT	500 Hz	10-20	100 ms
4LT	20-25 HZ	1-2.5	2-4 s

Table 3.1: *Reduction factor and latency of the different levels of the HERA-B trigger (design values).*

A common vertex for the two tracks is required. Additional requirements on the distance between the secondary vertex and wire can be applied.

If the event is accepted, the raw data of the full event, contained in the second level buffer, is processed by the Third Level Trigger (TLT), that can do a full track and vertex fit. The crucial difference between the SLT and the TLT is that the SLT analyses the data by request mode while the TLT has all the data available. The TLT was not used during the 2000 data taking period.

The last step is the Fourth Level Farm (4LT) that does the full reconstruction of the event and can also do classification into different physics classes to be used in different analysis. It can also apply a selection before storing the events to tape. The online calibration and alignment, together with the data quality monitoring, are also executed in the 4LT farm.

The Data Acquisition System

The Data Acquisition system (DAQ) integrates all the trigger levels, with the interconnections between them (hardware and software) and the logging protocols. The data flow is schematized in figure 3.16. Every bunch crossing (96 ns) all the data coming from the 520000 channels of the detector are readout and stored in 128-depth front-end pipelines, waiting for the FLT decision. The data used by the FLT are directly transmitted to the FLT network by the trigger link boards.

When the event is accepted, the data are transferred to the second level buffer, made of Digital Signal Processor (DSP) boards. This process is controlled by the Fast Control System (FCS). The SLT processes the data in a PC farm that can process different events in parallel. After the SLT, the TLT code is called (if necessary) and processed in the same node. Then, the data is sent by a fast Ethernet connection to the 4LT farm, where it is reconstructed and written to tape.

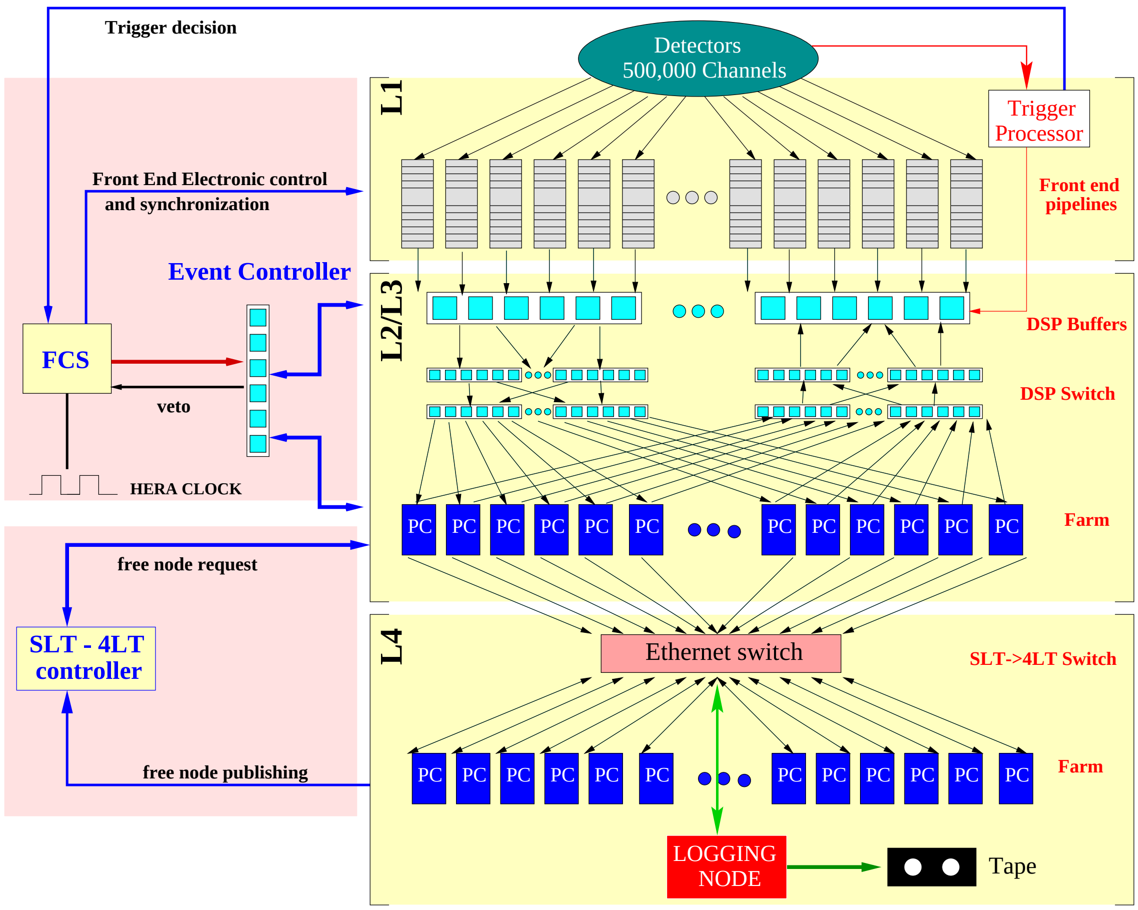

Figure 3.16: *Data flow during the data acquisition in HERA-B.*

3.4 The detector in the 2000 data taking period

The HERA-B detector was not fully installed and commissioned during the 2000 data taking period, as it was pointed out before, due to several technical problems that delayed the construction and commissioning (see [42] for more details).

Each subdetector was in a different situation. The VDS, the RICH and the SLT were fully installed and commissioned, working in stable conditions close to the design values. The ECAL and the MUON chambers were installed, but their performance didn't reach the design values. The OTR installation was finished in 2000 but the detector had several problems: there were frequent high voltage shorts that resulted in up to 15% of dead cells at the end of the running period, the resolution and the efficiency were below design, there were noise problems in the connections between the TDC and the trigger link boards and $\sim 10\%$ of the optical trigger links had transmission errors. This last two points also reduced the efficiency of the trigger system. The ITR was still in a commissioning phase. It was not fully working till the last two months and the design performance was not reached. It was not used in the trigger due to several problems in the read out chips. The first level trigger was in commissioning phase. J/Ψ's were seen but the rate was too low and the efficiency not understood. As a result the trigger conditions were changed very frequently, and there wasn't any large sample of data taken in exactly the same conditions. The high-p_T chambers were missing the interface to the trigger system and the TRD the electronic readout, so none of these two detectors was used during the 2000 run.

3.5 Offline reconstruction

HERA-B was designed to perform the data reconstruction online. During the data taking, online calibration and alignment constants are produced and stored in the HERA-B data bases to be used at the trigger level and during the reconstruction. However, a more detailed offline analysis can determine better alignment and calibration constants and, in the mean time, the reconstruction algorithms can be improved. In order to get the best possible results, the data can be reprocessed offline including all the most up-to-date information.

The analysis presented in this thesis was obtained with the third reprocessing of the 2000 data and therefore, the reconstruction procedure explained in the rest of this section corresponds to the one used in this third reprocessing.

3.5.1 Stand alone reconstruction

It is the first step of the reconstruction. The hit preparation and the *segment* reconstruction are performed at this stage.

- Hit preparation: this is the phase where the raw data stored by the subdetectors is transformed in hits that determine the point where the particle crossed each of the detector planes. A hit can be the position of the wire (OTR), the energy deposited in an ECAL cell, ... The calibration and alignment constants are retrieved from the data base and used at this point to correctly position the hit in space.

- Segment reconstruction: in this phase, segments are reconstructed using only the information from each subdetector, independently from the others. In the VDS and in the main tracker this means that the tracking reconstruction algorithms are executed. In the RICH, hits are combined to find rings if the standalone ring reconstruction (RISE) is used. In the ECAL, the energy deposited in different cells is combined to form clusters and to get the position of the cluster.

The VDS segment reconstruction is done with the package CATS (Cellular Automaton for Tracking in Silicon) [44] that uses a cellular automaton to find segments in the vertex detector. In the main tracking system (OTR and ITR), the tracking algorithm is a combination of two packages: OTR-CATS, that uses the same method as CATS and performs the pattern recognition in the PC chambers, and RANGER [45], that propagates the track through the magnet region and back from the PC to the TC chambers. RANGER does also the refit of the segment, once it is complete.

In the ECAL the cluster reconstruction is done with CARE [46].

The reconstruction of rings in the RICH can be done with different packages. One of them is the stand alone ring search (RISE) [47] that does not use any other information to reconstruct rings apart from the hits found in the photon detector of the RICH. It is executed at this stage of the reconstruction. The other two packages (RITER [48] and RIRE [49]) are track based algorithms, that use the track direction as the starting point of the ring search, so they are executed at the end of the reconstruction chain.

3.5.2 Matching

A matching algorithm, MARPLE [50], is applied to join the segments found in the VDS and in the main tracker (ITR+OTR). The algorithm used in the third reprocessing (called VDS-PC) exploits the especial features of the magnetic field in HERA-B but it does not consider the part of the segment that is inside the magnet[6], i.e., the segment in the main tracker is considered to start at the beginning of the pattern chambers, just after the magnet.

The magnetic field in HERA-B is along the y direction, bending the tracks in the xz plane. In the yz plane the track can be considered as a straight line because the magnetic field along x is negligible. Taking this into account, in the first step of the algorithm the VDS track is propagated to the beginning of the main tracker segment and the difference between the y coordinate of the PC segment and the VDS extrapolated track is required to be smaller than a maximum value ($\Delta y < 35.7\,\text{cm}$).

The second step exploits the fact that the magnetic field is symmetric with respect to the middle point of the magnet in the z direction. Therefore, the bending of the track in

[6]For some time, the alignment of the magnet chambers, together with their performance, were not precisely understood, as the efforts were concentrated in the trigger and patter recognition chambers. As a consequence, the magnet chambers were not used, neither for the matching nor for the momentum calculation.

the magnetic field can be approximated by a simple kick in the middle point.The main tracker and the VDS segments are then propagated to the middle z plane of the magnet region and the difference between the x coordinates of the extrapolated segments is also required to be smaller than a certain value ($\Delta x < 18.6\,\mathrm{cm}$).

These two first requirements are very soft, with the only purpose of reducing the combinatoric background and the execution time of the algorithm.

Then, a better estimation of the momentum is performed by requiring that both tracks should have the same slope, $tx = p_x/p_z$, in the middle of the magnet. Using the momentum to do the propagations, refined requirements in the difference of the x coordinate in the middle of the magnet and the difference in the y coordinate at the beginning of the PC segment are applied ($\Delta x < 2.6\,\mathrm{cm}$ and $\Delta y < 5.6\,\mathrm{cm}$).

Finally, it is possible to use the χ^2 of the momentum fit to apply further requirements to the combinations that passed the previous cuts. This possibility was not used for the 2000 data.

Any combination of a VDS and a main tracker segments that fulfill this requirements is accepted. Given the big number of charged tracks in the HERA-B environment[7], one segment in the main tracker may be matched with more than one VDS segment and vice versa. At this phase of the reconstruction, no other selection is applied, to keep the efficiency as high as possible.

More details about the matching algorithm can be found in [50] and [51].

3.5.3 Track reconstruction

Once the matching is done, the table of reconstructed tracks (RTRA) is filled using the procedure called *reco 2001* [52]. In the first step, all the VDS-main tracker matches are added to the track list. The non-matched main tracker segments are also added. This tracks are refitted with a χ^2 fit method based on the Kalman filter technique, that takes into account all the hits associated to the track [53],[54]. A better estimation of the momentum is performed here. This is the momentum that will be used for the long tracks.

Using the information from the refit a preselection of tracks is performed in such a way that each main tracker segment is used only once. The same VDS segment can still be used in more than one track, as there are some physical processes that can produce this situation (for example a gamma conversion in the VDS will have only one segment in the VDS detector because the two electrons are basically parallel there and will produce two segments in the main tracker, after the magnet has separated the different charged tracks).

[7]Between 55-70 in the main tracker and between 20-30 in the VDS, for a typical run in 2000.

The selected tracks are used now to perform the cluster search in the ECAL, with CARE. The tracks are propagated to the ECAL and the closest cluster that pass certain matching requirements is kept. Only one cluster can be associated to each track.

If the standalone ring search is used in the reconstruction of the RICH, the rings are also matched with the tracks, using the RICH-TRACK algorithm of MARPLE.

In the next step, the VDS segments and ECAL clusters that were not matched before, are matched together using MARPLE. The algorithm estimates the momentum with a simple kick formula for each VDS-ECAL pair. The difference of x and y positions at the last VDS plane are required to be smaller than a maximum value [50]. All the combinations that pass the selection conditions are stored as tracks. This step was used to improve the tracking efficiency in the periods where the tracker system had still very low efficiency.

Finally, all the VDS segments that were not matched with anything are also stored as tracks. The reason for this is that the VDS has a larger acceptance than the other subdetectors and some tracks that cross it do not cross any other detector. These tracks can help in the reconstruction of the primary vertices.

3.5.4 Particle identification

The track based PID algorithms are applied once the track reconstruction is finished. The muon identification algorithm, MURECB [55] propagates the tracks to the muon detector and searches for hits in the muon chambers. The likelihood probability that the track is a muon is determined and stored in the track table.

The track based algorithm of the RICH, RITER, is executed afterwards. It uses the slopes of the tracks to determine the center of the ring and start reconstructing it. The likelihood probability for each mass hypothesis is calculated and stored [48].

3.5.5 Track selection

The main purpose of the track selection algorithm is to choose the tracks in such a way that each segment is used only once, in order to minimize the fraction of clones/ghosts. The selected tracks are flagged. The non-selected tracks are also kept as they may be interesting for other kind of analysis. The track selection depends strongly on the analysis one is interested in. For a detailed discussion see for instance [56] or [57]. In this thesis the selection criterion is the following: only tracks with a VDS and a main tracker segment are used. The tracks are selected in such a way that both segments are used only once by choosing the track that maximizes the following quantity:

$$fom = H_{MAIN} + H_{VDS} + H_{ECAL} + 2 \cdot H_{RICH} - \frac{\chi^2}{N_{dof}} \tag{3.1}$$

where H_{XXX} is the number of hits in the corresponding subdetector and χ^2/N_{dof} is the normalized χ^2 of the track. This selection criterion gives priority to the longer tracks, with the smallest χ^2.

3.5.6 Primary vertex reconstruction

It is performed at the end of the reconstruction chain by GROVER [58]. The algorithm [59] starts searching for clusters of tracks close to the wire position, i.e., within 3σ from the wire, where σ is the track resolution. A first estimation of the vertex position is calculated as the weighed average of the track positions, counting all the tracks in a cluster. Tracks wrongly associated to a vertex can reduce the vertex resolution. To improve the association of tracks to vertices a filtering procedure is applied: the χ^2 contribution of each track to the total vertex χ^2 is calculated. Those tracks that give a χ^2 contribution larger than 20 are rejected. This requirement corresponds to a 10% probability of rejecting a track correctly associated to the primary vertex. If the track is accepted, the vertex position and its covariance matrix are updated. In the next step, the track parameters are estimated taking into account the updated vertex position. The whole procedure is then iterated a couple of times till the desired resolution is reached. It was checked that with more iterations the resolution will not improve [59].

GROVER can also estimate the mean wire position by averaging the primary vertex position over a large number of events. This method gives a more accurate starting point for the primary vertex search.

3.6 Data sample

3.6.1 Real data

The 2000 year run period was mainly dedicated to the detector commissioning. Nevertheless, some data samples for physics studies were taken. In April 2000, around 3 millions of inelastic events were taken using different target materials. They were essential to develop the tracking system and do the first studies about the luminosity [60], particle fractions [49], V0 cross section [61] and Λ polarization studies [57].

The largest data sample consisted of events triggered with a J/Ψ (double lepton triggers), either in the electron or in the muon decay channel, with several different trigger requirements. They were used for the commissioning of the trigger and later on, for the measurement of the $b\bar{b}$ cross section [62], J/Ψ differential cross sections [63] and χ_c studies [64].

Finally, a sample of around 5 million of events were taken with a single lepton trigger. As this sample is enriched in heavy quarks, specially charm, it will be used to search for

D meson decays in the analysis presented in this thesis.

The single lepton runs were taken in August 2000, at the end of the data taking period. At this time the detector was completed and running in stable conditions, but the trigger was still in commissioning phase. The total data sample consists of $\sim 5\,\mathrm{M}$ of events, but not all of them in the same conditions. The trigger conditions and the number of events for each run are summarized in table 3.2. The first million of events (sample A) were taken with a single muon trigger, requiring in the pretrigger a two pads coincidence in the last two muon chambers and a track with $\mathrm{p_T} > 1.\,\mathrm{GeV}$ in the FLT and SLT. The SLT was using the FLT record and applying the algorithm with slicer and refit [65]. The run 17137 (sample B) was in the same conditions as sample A, but the SLT was not using the FLT record. For the rest of the runs, the ECAL and muon pretrigger were used together. A pretrigger signal was either an ECAL cluster with $E_t > 1\,\mathrm{GeV}$ or a two pads coincidence in the last two muon chambers. For the run 17242 (sample C), the FLT and the SLT searched for a track with $\mathrm{p_T} > 1\,\mathrm{GeV}$ and the SLT was using the FLT record. The sample D was taken with the same trigger conditions plus an extra requirement in the maximum occupancy in the RICH ($N_{hits} < 3000$) to reduce the number of events with multiple interactions. The last sample (E) was in the same conditions as D but increasing the requirement on transverse momentum in the SLT ($\mathrm{p_T} > 1.5\,\mathrm{GeV}$). The interaction rate was 2 MHz for all the runs but the run 17265, that was taken at 5 MHz. The target wire was in all the cases the same, the *inner II* wire, made of carbon.

The OTR gas mixture and the HV thresholds were changed slowly from run 17242 to 17266.

All these differences make the sample very unsuitable for the an absolute cross section measurement, as it is impossible to estimate accurately the efficiency of the trigger. Nevertheless, it is still good for the measurement of cross section ratios, assuming that the changes in the trigger conditions affect the two measurement channels in the same way.

The data was reconstructed several times, with improved algorithms for the track reconstruction and selection and better calibration and alignment constants. In the analysis presented in this thesis, the third and last reprocessing was used. The reconstruction chain was explained in section 3.5.

3.6.2 Monte Carlo

In order to study the efficiencies and optimize the cuts for the reconstruction of the D mesons it is necessary to have a good simulation of the detector and the interactions that happen in the experiment. The event generator of HERA-B uses two different packages to properly simulate the complete interaction. PYTHIA/JETSET [66] is a generator optimized to simulate the hard processes and it cannot properly simulate the nuclear

Sample	run number	Trigger	I_{rate} (MHz)	N_{events}
A	17116,17127-17135	single μ (FLT+SLT)	2	1.08 M
B	17137	single μ (no FLT)	2	0.41 M
C	17242	FLT: Single μ or e ($\mathrm{p_T} > 1.5\,\mathrm{GeV}$) SLT: $\mathrm{p_T} > 1.\,\mathrm{GeV}$	2	0.16 M
D	17243,17245,17246	Single μ or e ($\mathrm{p_T} > 1.\,\mathrm{GeV}$), RICH cut	2	0.62 M
E	17251-17266	FLT: Single μ or e ($\mathrm{p_T} > 1.\,\mathrm{GeV}$) SLT:($\mathrm{p_T} > 1.5\,\mathrm{GeV}$), RICH cut	2/5	2.35 M

Table 3.2: *Summary of the trigger conditions for the single lepton triggered runs.*

effects. On the contrary, FRITIOF [67] is optimized to generate normal inelastic proton-nucleus interactions but the heavy flavor production is not correctly treated. The solution for HERA-B consists in a combination of both packages [68]. In the first step PYTHIA is called to generate the heavy quark pair in the collision of the proton with a nucleon from the target nucleus. The remaining energy after the production of the heavy quark is passed to FRITIOF to generate the underlying nuclear interactions. There are different modes to generate the fragmentation of the heavy quark that produce the heavy hadrons, before calling FRITIOF. The MC used in this thesis was produced with the following procedure [68]: when the heavy quark is generated in a color singlet cluster, the heavy quark and all the decay products are kept. If it is created in a color string, the string containing the heavy quark is boosted to its rest frame. All the first generation fragments that move into the heavy quark hemisphere, together with their decay products, are kept. The other fragments are discarded. The selected particles are boosted back to the lab frame. With this scheme, the heavy hadron and the associated particles keep the flavor correlations.

After FRITIOF, all the particles are passed through the detector simulation, done with the GEANT package [69]. The geometry, dead materials and detector positions are described as they were at the time of data taking, August 2000. The detector simulation was done in a realistic way: the masking of noisy/dead channels from the runs of the single lepton trigger was applied for the OTR/ITR and the ECAL and the hit efficiencies and hit resolutions for the OTR and ITR were set to realistic values. An automatic procedure that searches into the data base for the appropriate values, corresponding to the run that is indicated, was used. No simulation of noise in the subdetectors was applied because it was not available.

Around 280000 $c\bar{c}$ and 400000 inelastic events were produced [70]. The $c\bar{c}$ events were forced to have a D^+ or a D^0 decaying into the channels: $D^+ \to K\pi\pi$ and $D^0 \to K\pi$. In

Sample	events
Inelastics	$\sim 400\,K$
$c\bar{c}$ with a $D^+ \to K\pi\pi$	$\sim 74\,\mathrm{K}$
$c\bar{c}$ with a $D^0 \to K\pi$	$\sim 200\,\mathrm{K}$
$b\bar{b}$ with a $D^0 \to K\pi$	$\sim 17\,\mathrm{K}$

Table 3.3: *Samples of Monte Carlo data used.*

table 3.3 the number of events of each kind are shown. A small sample of $b\bar{b}$ events with a $D^0 \to K\pi$ was also produced, to study the possible background coming from $b\bar{b}$ events.

The simulation of the trigger was not applied for two reasons: it was still in a developing phase, with a non-user-friendly runnable version, and the number of available MC events was not enough to get good statistics after the trigger simulation[8].

In order to reproduce the occupancies observed in real data for the single lepton triggered runs, the $c\bar{c}$ events were mixed with 1 inelastic per event in average following a Poisson distribution. It is not possible to reproduce with the MC the background distributions of the real data, specially because the trigger simulation was not used. Therefore, the underlying event in the MC is there just to ensure that the reconstruction efficiencies for the D's are the correct ones (the one expected for the real data) as the reconstruction efficiency may depend on the occupancy of the event.

The reconstruction chain for the MC was exactly the same as for the real data, explained in section 3.5.

[8]Note that the simulation of one MC event can take one billion times longer than the duration of a real event in the detector, making very time consuming to generate a large amount of MC events.

Chapter 4

Impact parameter tagging

4.1 Introduction

In this chapter, a new procedure to reconstruct and isolate the decay of a particle with lifetime will be presented. The impact parameter tagging is a powerful method that combines the information from the lifetime of the mother and the impact parameter of the daughter tracks in one quantity that can be enough to separate the desired decay from the background. This method has been used successfully in other experiments to separate $b\bar{b}$ events from the background, taking into account that in a $b\bar{b}$ event there are, in average, more tracks with lifetime than in other events, due to the decay of the beauty particles [71].

The main idea consists in getting advantage of the large impact parameters that characterize the daughter tracks of a long-living particle. A signed impact parameter is defined in such a way that particles coming from the primary interaction will have, in average, the same probability of having positive or negative impact parameter, while tracks with lifetime always have positive impact parameters. The significance distribution of the tracks with negative impact parameter is used to parametrize the probability that a track comes from the primary vertex. The probabilities of all the daughter tracks are combined together in a simple way to obtain a quantity that condenses all the information and is very powerful to separate the signal decay from the background. The more tracks participating in the combined probability, the more powerful the method is. The same happens with the decay distance: the larger the lifetime, the better the capability to separate the signal from the background.

In the next section, the method of the impact parameter tagging will be explained in detail. Then, a study of the errors of the tracks and vertices in real data are presented. The application of the method to the real data will be discussed afterwards.

4.2 Method

4.2.1 The signed impact parameter

The impact parameter of a track with respect to a vertex is calculated as the smallest distance in the space between the track and the vertex. All the tracks used in this analysis start in the VDS detector, where there is no magnetic field, so, in this case, they are considered as straight lines in the calculation of the impact parameter.

The definition of the sign is based on the fact that the decay point of the hadron must lie along its flight path. The impact parameter of a track with respect to the primary vertex is positive when the point of closest approach between the daughter track and the reconstructed mother track is downstream from the primary vertex. With this definition, the sign of the impact parameter can only be calculated after reconstructing the decay of the mother particle. For the signal decays, if no measurement errors are present, the point of closest approach between each of the daughter tracks and the mother track is always the decaying vertex, that should be placed downstream from the primary vertex if the decaying particle has a certain lifetime, resulting in a positive sign.

When measurement errors are considered, the background combinations made of tracks produced in the primary interaction will have the same probability of having positive or negative sign. To make this point more clear consider a charged D that decays in the hadronic mode $D^+ \to K^-\pi^+\pi^+$. Imagine that three tracks from the primary vertex are combined to form a fake D^+ candidate, called D^+_{fake}. The reconstructed decaying vertex will lie in a certain region around the primary vertex and the D^+_{fake} reconstructed track will have basically any direction around the primary. Then, the point of closest approach between each track and the reconstructed D^+_{fake} will have exactly the same probability of lying upstream or downstream from the primary vertex. This point is illustrated in figure 4.1.

In what follows, the decay channel $D^+ \to K\pi\pi$ will always be used to illustrate the method. This notation includes the decay $D^+ \to K^-\pi^+\pi^+$ and its charge conjugated decay. In the same way, $D^0 \to K\pi$ will stand for $D^0 \to K^-\pi^+$ and $\bar{D}^0 \to K^+\pi^-$.

In reality, the tracks coming from the decay of a particle with lifetime can have negative impact parameter due to the finite resolution in the measurement of the track parameters and the vertex position. When the decay happens too close to the primary vertex, the experimental resolution may be insufficient to differentiate the secondary from the primary vertex and around half of those tracks with lifetime will have negative impact parameters. This is the main contribution to missigned tracks. When the reconstructed decay vertex is far enough from the primary to differentiate it, the missigning probability is very low. The effect is clear when looking at figure 4.2, where the efficiency of assigning the correct sign for the impact parameter has been plotted as a function of the distance in z between

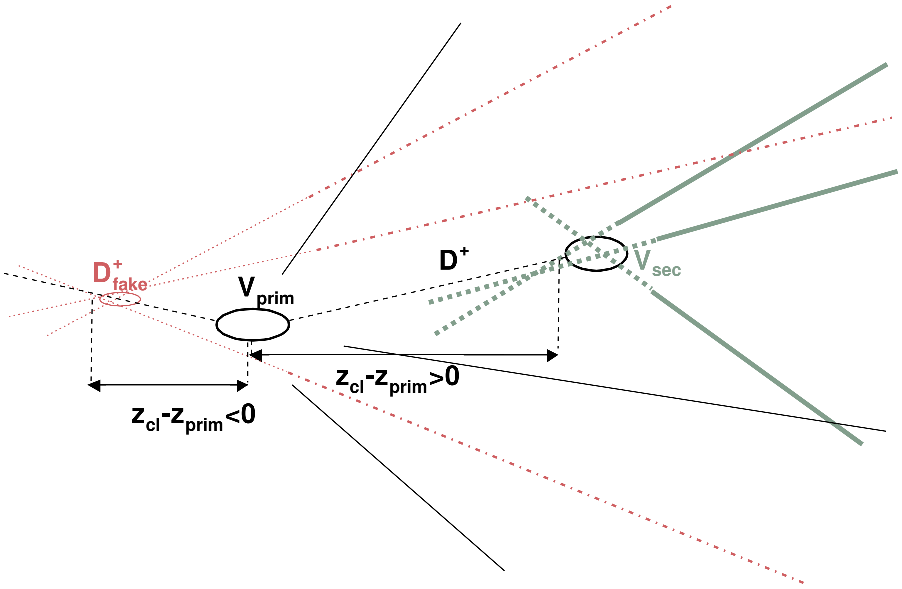

Figure 4.1: *Scheme showing the impact parameter signing procedure. The thick lines represent the daughter tracks of a true D^+ decaying into $K\pi\pi$. All the tracks in the decay have positive impact parameters. The dashed-dotted lines stand for a background combination of three tracks coming from the primary vertex that produce negative impact parameters.*

the primary and the secondary vertices. The efficiency for decays that happen within $1\sigma_z$ from the primary, with $\sigma_z = \sqrt{\sigma^2_{z_{prim}} + \sigma^2_{z_{sec}}}$, is around 50%, rising till 99% for decays that happen more than $6\sigma_z$ far from the primary.

The resolution on the impact parameter depends strongly on the momentum of the track, on the angle with the z axis and on the number of VDS hits, making it very difficult to compare directly the impact parameter from different tracks. It is better to use, instead, its statistical significance, defined as the ratio between the impact parameter and its measured error, $S = b/\sigma_b$.

σ_b is calculated from the covariance matrix of the track and the primary vertex. The details about the calculation are explained in the appendix A. In order to get the full statistical power of the method the correlations between the primary vertex and the tracks should also be taken into account. In HERA-B, the primary vertex is calculated with an iterative algorithm (section 3.5.6), that makes it impossible to estimate analytically the contribution from the correlation. To avoid introducing biases, the primary vertex is reconstructed again excluding the tracks that will be used to reconstruct the D candidate.

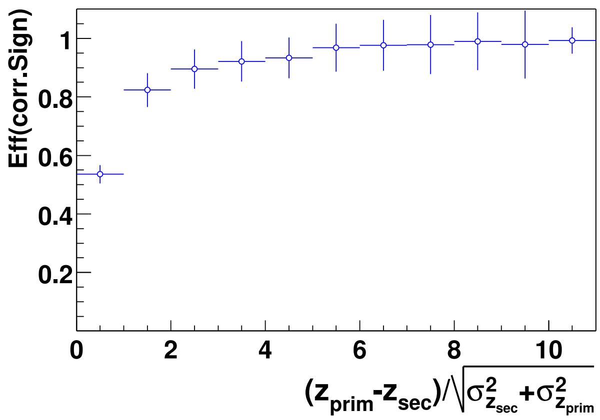

Figure 4.2: *Efficiency of assigning the correct impact parameter sign to the tracks coming from the decay of a D^+, as a function of the distance between the primary and the secondary vertex, divided by its error.*

This method has the disadvantage that the resolution on the primary vertex position might be worse than expected. In general, the larger the number of tracks used in the primary vertex the better the resolution on its measured position. When the three tracks used to reconstruct the D candidate are, in fact, tracks produced at the primary interaction, the primary vertex is reconstructed with three tracks missing, resulting in a poorer resolution.

A sample of Monte Carlo inelastic events, with 1 interaction per event in average, was used to study the significance distribution of the tracks used to reconstruct D candidates[1]. In figure 4.3, the significance for all those tracks is plotted with a solid line. The root mean squared distance between the tracks and the reconstructed secondary vertex was required to be smaller than a maximum value ($RMS < 0.05\,\text{cm}$) in order to reject very badly reconstructed vertices. A stronger requirement is not needed at this stage.

For the inelastic events, the immense majority of the D candidates are background. This explains why the significance distribution is symmetric around zero. The histogram with open circles represents the significance for the tracks coming from the decays of long living particles, like K^0_S and Λ^0, combined with other background tracks to form a fake D^+ candidate. This particles are the responsible for the larger values of the significance, either positive or negative, in inelastic events. They can have negative values because they are forming fake secondary vertices with tracks that may come from the primary. They

[1] A 'D candidates' or a ' reconstructed D track' means combinations of three tracks that were joined to make a vertex out of them. By default, no quality requirement is applied to the secondary vertex, so in principle any triplet of tracks can be a D candidate.

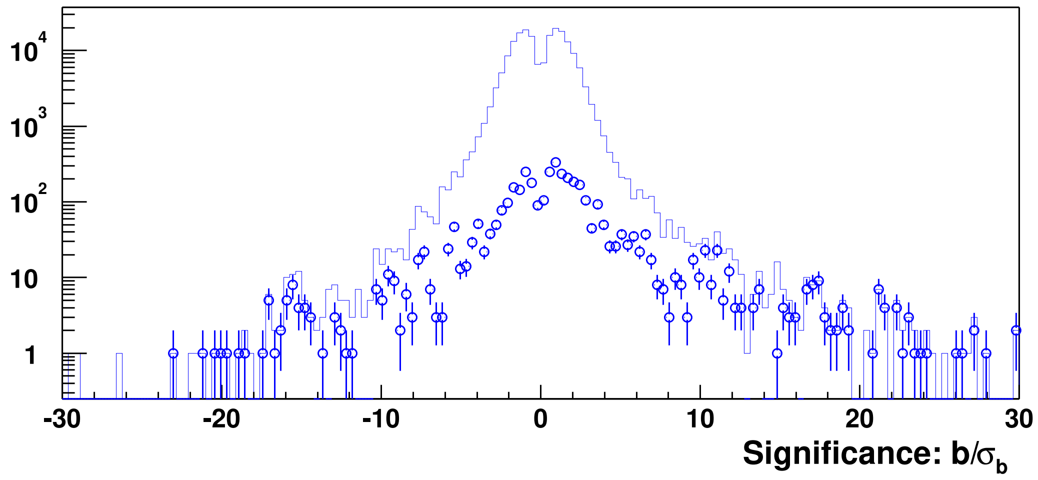

Figure 4.3: *Impact parameter significance of all tracks used in the reconstruction of D candidates in MC inelastic events (solid line). Here, a D candidate is any combination of three tracks that pass the vertex fit with a $RMS < 0.05$ cm. The significance of tracks that come from the decay of a long living particles, like K_S^0 and Λ^0, is displayed with open circles.*

produce a small tail to the positive side, so the resulting significance distribution is not perfectly symmetric. These lifetime tracks can be rejected by requiring good quality of the reconstructed secondary vertex.

The significance distribution for $c\bar{c}$ events where a $D^+ \to K\pi\pi$ was produced is shown in figure 4.4. Again, a soft requirement on the quality of the secondary vertex was applied ($RMS < 0.05\,\text{cm}$)[2], just to eliminate very badly reconstructed secondary vertices. The solid line, represent all the tracks in the event. The light shadowed region are the tracks coming from the primary vertex. The distribution is symmetric around zero, as it was expected. The daughter tracks of the D^+ are represented by the dark shadowed histogram. Most of them have large positive impact parameters, producing a long tail to the positive side of the significance distribution. There are, nevertheless, a small number of D^+ daughter tracks with negative significance due to decays that happened too close to the primary vertex that cannot be resolved.

[2]In the rest of this section, a secondary vertex will be any combination of three tracks that pass the vertex fit with a $RMS < 0.05\,\text{cm}$. The RMS will be discussed later, on sections 4.3.6 and 5.3.

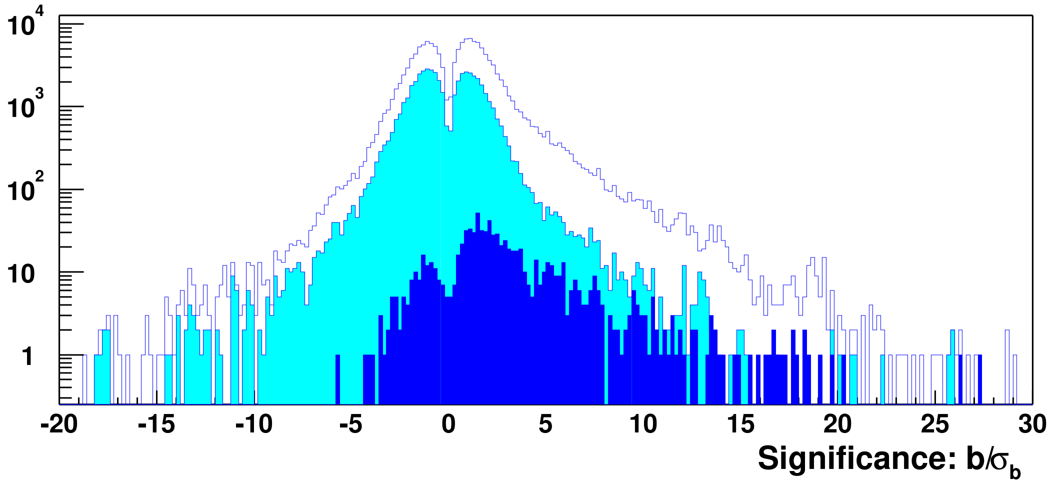

Figure 4.4: *Significance of the impact parameter for $c\bar{c}$ events where a $D^+ \to K\pi\pi$ was produced. The solid line corresponds to all the tracks in the event. The light shadowed region correspond to tracks coming from the primary vertex and the dark shadowed histogram to the signal, i.e., the D^+ daughter tracks.*

4.2.2 Track probability

The negative side of the significance distribution represents the shape of background under the positive side.

If the errors in the tracking and in the vertexing were exactly gaussian the negative side of the significance distribution could be described by a function of the type $c_1 x e^{-x^2/2\sigma^2}$. The contribution from missigned tracks and non-gaussian tails in the errors can be parametrized with a term of the form $c_1 x e^{-x/\Lambda_1} + c_2 e^{-x/\Lambda_2}$. As a consequence, the best function to describe the shape of the significance is the sum of those two terms: $f(x) = c_1 x (e^{-x^2/2\sigma^2} + e^{-x/\Lambda_1}) + c_2 e^{-x/\Lambda_2}$, where the parameters c_1, σ, Λ_1 and Λ_2 are obtained from the fit. $f(x)$ measures the resolution of the impact parameter significance and describes well the negative side of the distribution (see figure 4.5).

The resolution function can be considered as the differential probability that a track comes from the primary vertex. Integrated, it gives the total probability for a track to be produced at the main interaction vertex. Mathematically, it is the probability that a track from the primary vertex produces the observed impact parameter or any other value

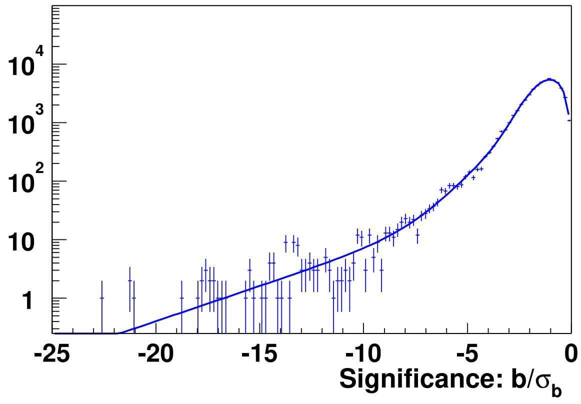

Figure 4.5: *Fit of the negative side of the significance distribution for $c\bar{c}$ events where a $D^+ \to K\pi\pi$ was produced. The resolution function has the form: $f(x) = c_1 x(e^{-x^2/2\sigma^2} + e^{-x/\Lambda_1}) + c_2 e^{-x/\Lambda_2}$.*

equally or more unlikely:

$$P_T = \int_{S_b}^{\infty} f(x)dx \tag{4.1}$$

P_T can also be thought as the probability that a measured b/σ_b is compatible with the fitted shape of the resolution function. In what follows, a negative probability will stand for the function (4.1) applied to a track with negative impact parameter.

The track probability for $c\bar{c}$ events where a $D^+ \to K\pi\pi$ was produced is shown in figure 4.6, for all the tracks in the event (solid line) and for the daughter tracks of the D^+ (dark shadowed region). The negative side of the distributions is flat because it was used to define the probability, demonstrating, again, that the calibration function describes perfectly well the shape of the background. The positive side is mostly flat, but it has a spike at zero, produced by the tracks that were in the tail of the significance distribution and have a very small probability of coming from the primary vertex. The D^+ daughter tracks with negative probability, or with positive probability but with large values, are due to the D decays that happen too close to the primary, as explained before.

It it interesting to remark here that the long tails in the significance distribution have translated into a sharp spike, easier to select and to manipulate.

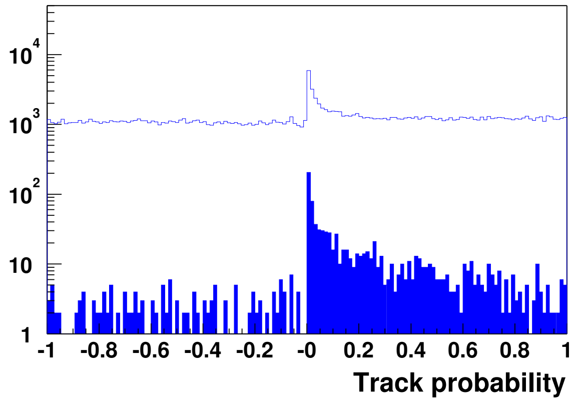

Figure 4.6: *Track probability distribution for $c\bar{c}$ events where a $D^+ \to K\pi\pi$ was produced. The scale in the y axis is arbitrary. The solid line represents all tracks. The shadowed histogram corresponds to the signal decays, the D^+ daughter tracks.*

4.2.3 The combined probability

To get the maximum advantage of the impact parameters in the decay of a long living particle, it would be optimal to combine the track probabilities of all the daughter tracks.

The combined probability of N tracks can be expressed as [71]:

$$P_N \equiv \Pi \cdot \sum_{j=0}^{N-1} \frac{(-ln\Pi)^j}{j!}, \tag{4.2}$$

where $\Pi \equiv \prod_{i=1}^{N} P_{T_i}$. The demonstration that this quantity behaves as a probability can be seen in [71] .

P_N is the probability that any group of N tracks without lifetime produce the observed values of the track probabilities or any other set of values equally or more unlikely. Only tracks with $b > 0$ enter in the calculation of the combined probability, P_N, as the other ones were mainly produced at the primary vertex. This reduces the chances of using a background track by 50%.

In figure 4.7 the combined probability of the three daughter tracks is plotted, for the vertices associated with the MC D^+ decays (dots) and for the background from inelastic events (solid line). The spike at zero for the signal is now more pronounced than for the individual track probabilities in figure 4.6, increasing the separation power between the signal and the background. There is also a small spike at 1 corresponding to the cases

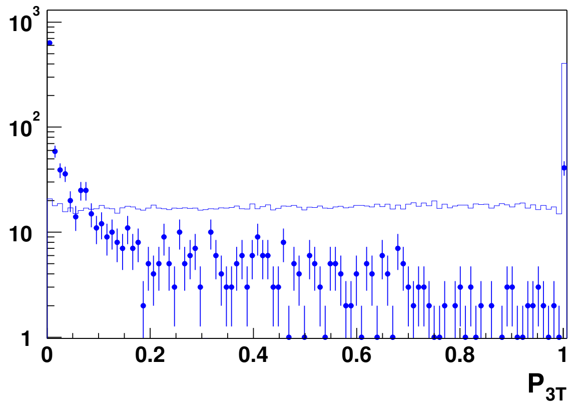

Figure 4.7: *Combined probability of the three daughter tracks for all the background D candidates in inelastic events (solid line) and for the signal $D^+ \to K\pi\pi$ decays in $c\bar{c}$ events (full circles).*

where no daughter tracks have positive impact parameter, i.e., to those D's that decayed very close to the primary. The distribution for the background is basically flat with a big spike at $P_{3T} = 1$.

The efficiency and rejection factor of a cut on the maximum combined probability of the three daughter tracks ($P_{3T} < x$) is plotted on figure 4.8, as a function of the maximum P_{3T} required. The background from inelastic events is plotted with crosses. A soft requirement on P_{3T}, for instance $P_{3T} < 0.05$, has an efficiency of 64% with a rejection factor of 96% for the background. Increasing even more the requirement on P_{3T}, better signal to background ratios can be obtained, reducing only slowly the efficiency. For the background coming from $c\bar{c}$ event the efficiency is plotted with open circles. It is larger because there are more tracks with lifetime, coming from other charmed hadrons, that increase the indidividual track probabilities. In general, the main background in the reconstruction of a decay like the $D^+ \to K\pi\pi$ come from vertices made by one or two tracks coming from the decay of another particle, plus one or two tracks from the main interactions. This combinations produce a small P_{3T} that may pass the requirements. They can be eliminated by identifying the particles in the decay or requiring a good quality secondary vertex.

For comparison with the requirement on the combined probability, the efficiency and rejection factor of a cut on the minimum lifetime of the D^+ is shown in figure 4.9, as a function of the minimum lifetime required. The signal is, again, plotted with full circles

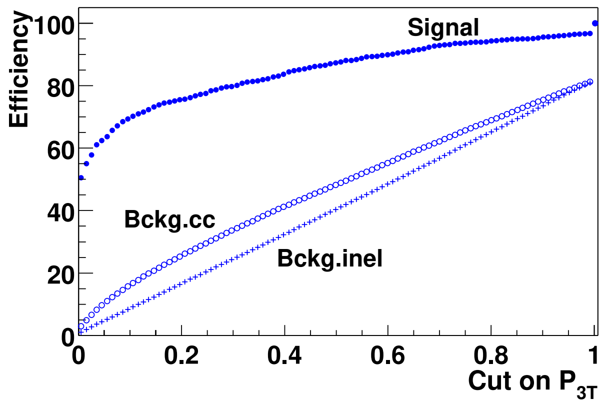

Figure 4.8: *Efficiency of a cut on the maximum combined probability ($P_{3T} < x$) for the signal (full circles), for the background from inelastic events(stars) and for the background from $c\bar{c}$ events (open circles), as a function of the maximum combined probability cutoff.*

and the background from inelastic events with stars. For a rejection factor of 96% the efficiency is 50%, that is a relative factor of 30% lower than the one obtained by requiring a small P_{3T}. Increasing the signal over background ratio a little bit more implies significant looses in efficiency, that do not occur for the cut on the combined probability.

4.3 Impact parameter significance for real data and MC

To apply the impact parameter tagging it is necessary to understand very well the errors and in particular, to demonstrate that there is no bias in the measurement of the impact parameter and its error, that could reduce the selectivity of the method. Nevertheless, it is not necessary to ensure that the actual value of the errors is the correct one if the effect is homogeneous for all tracks, because the calibration function will account for a global widening/narrowing of the significance distribution. This is a very powerful property of the impact parameter method presented here: it is self-calibrated so it can handle homogeneous over- or underestimations of the track errors.

At the time that this analysis was done, very few information existed about efficiency of the tracking, resolution in momentum and track parameters. Therefore, the knowledge about the errors of the tracks was also very poor. It was generally believed that the covariance matrix was underestimated by a certain factor, but there was no study about this.

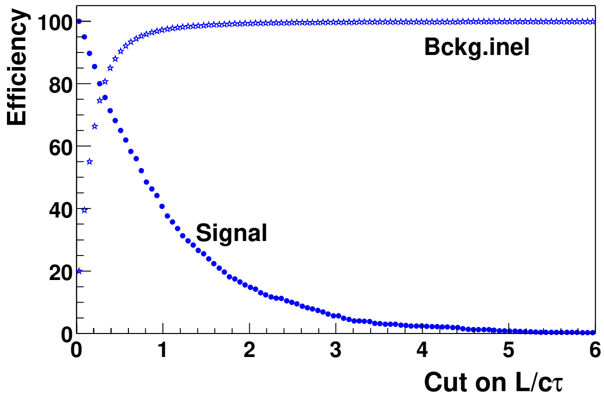

Figure 4.9: *Efficiency for the MC signal (full circles) and rejection factor for the background from inelastic events (stars) as a function of the minimum lifetime required in a* D^+ *decay.*

To demonstrate that there is no bias on the track errors, the significance for tracks coming from the primary interaction will be compared with the significance for tracks produced in the decay of other particles, using the MC-truth to differentiate them. But, before that, it should be proved that the MC reproduces well the real data.

The sample to search for D decays is the single lepton triggered runs (see 3.6.1). The trigger system was still in developing phase when the data was taken, and its performance at that time is still not well understood, so it is impossible to reproduce with the MC all the details of the real data, as for example, occupancies or track distributions in the phase space. Therefore, a sample of minimum bias runs, that are pretty well understood will be used to do the comparison between data and MC. The scheme of the analysis is the following:

- Analyse the track distributions, comparing data and MC, to ensure that the MC reproduces well the tracking.
- Compare the track errors for real data and MC. If any correction is needed it will be applied.
- Study the primary vertex reconstruction. Compare resolution in position and error distributions for data and MC.
- Finally, the behavior of the the impact parameter significance will be checked with the MC to demonstrate that there is no bias.

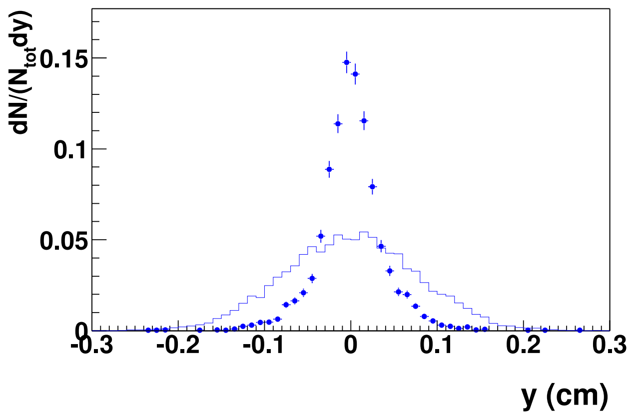

Figure 4.10: *Distribution of the y coordinate of the primary vertex, for real data (full circles) and MC (solid line). Both distributions are normalized to the same number of entries.*

HERA-B has taken several runs of minimum bias data, with a large number of events. In addition, there are random triggered events intermixed with all the other data samples, independently of the trigger setup. To do the comparison between data and MC, the random triggers taken at the same time of the single lepton events were used. Since not too much statistics are needed, this sample is sufficient and guarantees that the data has the same detector conditions.

The MC data sample consisted of 20 K inelastic events, with one interaction per event, in average. The data was reconstructed in a realistic way by applying the masking of hot/dead channels from the run 17137 in the OTR, ITR and ECAL reconstruction. Realistic channel efficiencies were also used for the OTR and ITR (see section 3.6.2).

There is one important difference between the MC and the real data: the width of the beam is not properly simulated. The target used during the single lepton triggered runs was the *inner II wire*, that is along the y direction. In this case, the y coordinate distribution width of the primary vertex is the convolution of the primary vertex resolution in y with the beam size along y, as the target dimensions along this direction are very large. The resolution in the y coordinate of the primary vertex is very small in comparison with the beam size, so the width of the distribution can be considered to be produced by the width of the beam. As it can be seen in figure 4.10, the interaction region is wider in the MC, implying that the probability of merging vertices in real data will be larger. As a consequence, it will be impossible to compare events where there is more than one interaction. For events with only one interaction, the comparison between MC and real

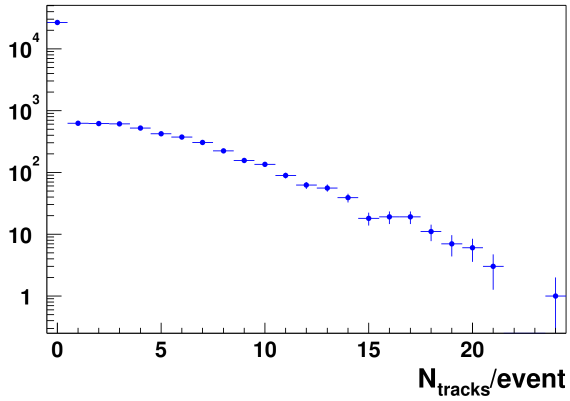

Figure 4.11: *Distribution of the number of tracks per event, in real data (minimum bias events from the single lepton runs).*

data is still possible because the individual track distributions and the relative distance between tracks and vertices are not affected by the beam size.

The best way of selecting events with one interaction is to use only events with one reconstructed primary vertex. As the requirements applied to the primary vertex (explained in section 4.3.3) are very selective, there will be a fraction of events with two or more interactions that have, in fact, only one reconstructed primary. The fraction of those events was studied using a sample of Monte Carlo inelastic events with an occupancy similar to the one observed in the single lepton runs. Only the interactions that produce more than 4 tracks inside the acceptance of the VDS were considered, as the other ones will not be detected. In these conditions, 22% of the events with one reconstructed primary were produced by more than one inelastic interaction. Those cases correspond, typically, to two interactions that happened too close one to the other to resolve them. Therefore, the track distributions will not be affected, and the comparison can be done.

4.3.1 Track reconstruction

The tracking efficiency and resolutions may depend on the occupancy of the event, so it is very important to properly reproduce the real data occupancies with the MC. To compare the total occupancy, the empty events were removed from the real data[3] by requiring at least one long track in the event (i.e. a track with a segment in the VDS and a segment in

[3]There are no empty events in the MC.

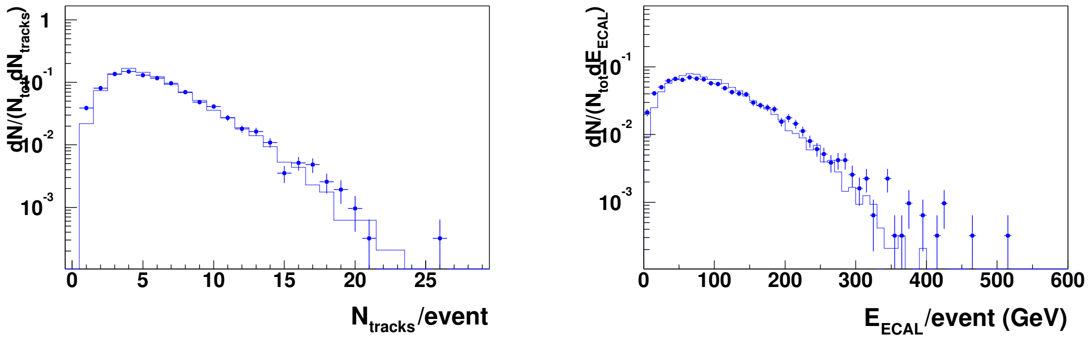

(a) (b)

Figure 4.12: *Comparison of the occupancies for real data (dots) and MC (solid line), after extraction of empty events. Two distributions are shown: number of tracks per event (a) and total energy deposited in the ECAL per event (b). In both cases the histograms are normalized to the same number of entries.*

the main tracker). The distribution of the number of tracks per event in real data can be seen in figure 4.11. The cut will eliminate just the events in the first bin. After eliminating empty events, the total number of tracks per event and the total energy deposited in the ECAL per event are compared for real data and MC in figure 4.12. Apart from small deviations in the tails, that are not statistical significant, the real data and the MC agree within one standard deviation.

Before having a look at the track errors, all the quantities that influence the track parameters were checked to see if the real data is well reproduced in the MC: spatial distributions, angles, momentum, transverse momentum and number of hits in the VDS, for events with only one primary. All these distributions are shown in figures 4.13 and 4.14. The differences in small regions of some distributions (like the first three bins in the p_t distribution) are not large enough to produce visible effects on the track errors or on the impact parameter distributions, that will be checked in the next subsection. Therefore, it can be considered that the MC reproduces the real data sufficiently well to perform the intended analysis.

4.3.2 Track errors

The tracks are described by the coordinates at the first point (x,y,z) and the momentum at that point ($tx = px/pz$, $ty = py/pz$, Q/p), as obtained after the refit of the track. The errors on those parameters and their correlations are described by their covariance matrix C_{tr}. For an n-dimensional random variable, $\mathbf{x}$, with components x_i, (i=1,2, ..., n), the

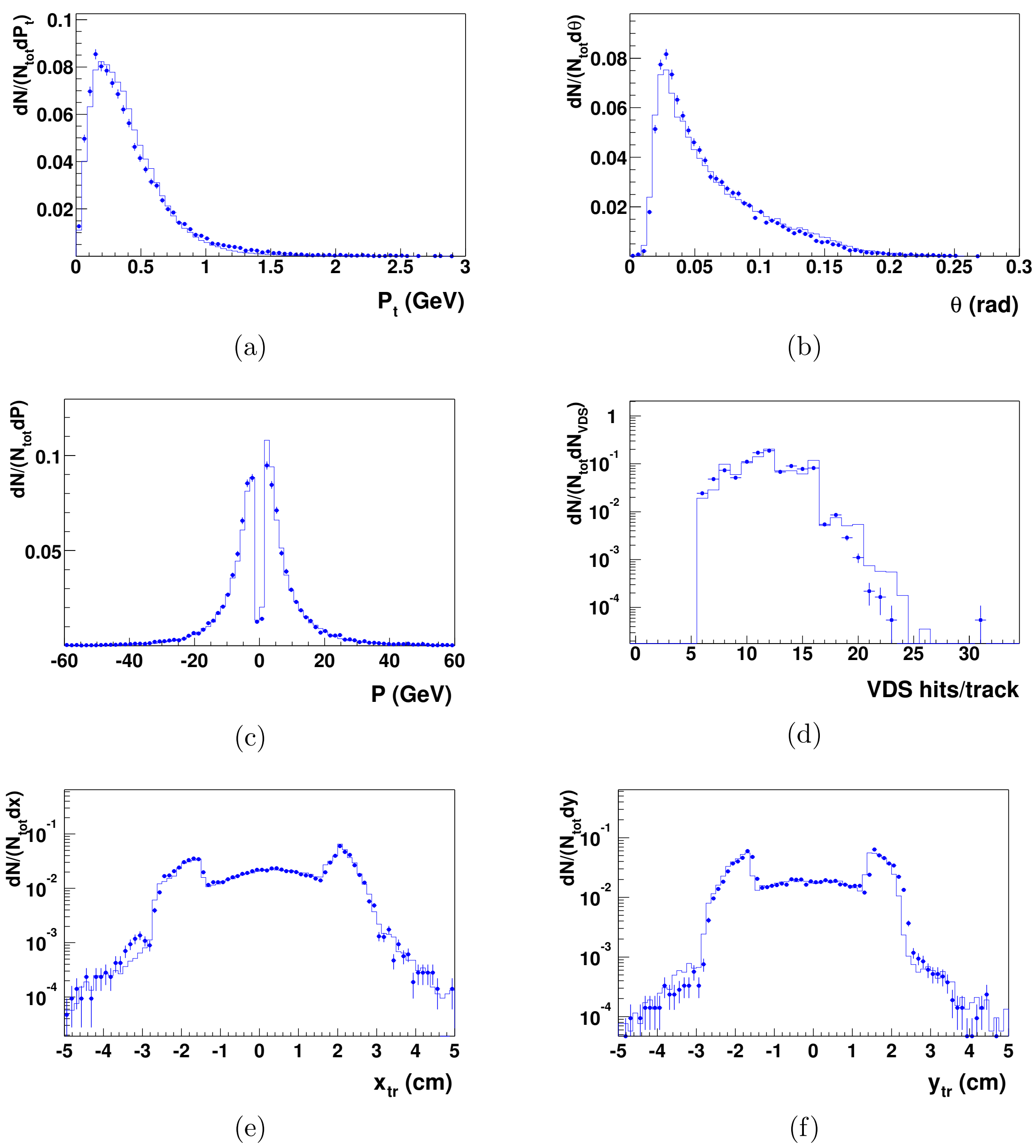

Figure 4.13: *Comparison of some track distributions for MC (solid line) and real data (dots), using minimum bias events: (a) Transverse momentum of the track; (b) Angle between the track and the z axis; (c) Momentum of the track; (d) Number of hits that the track has in the VDS detector; (e) x coordinate at the first measured point of the track; (f) y coordinate at the first measured point. In each plot both histograms are normalized to the same number of entries.*

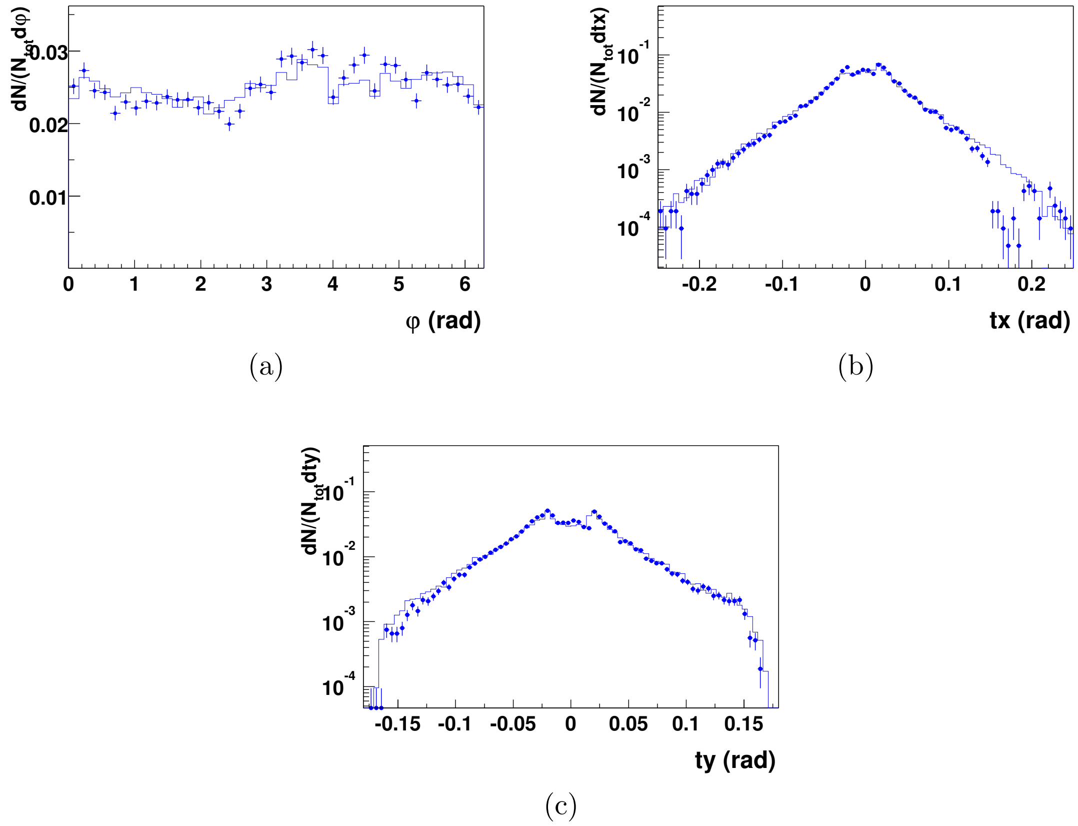

Figure 4.14: *Comparison of some track distributions in MC (solid line) and real data (dots), using minimum bias events: (a) angle with respect to the x axis; (b) slope in x (p_x/p_z); (c) slope in y (p_y/p_z). In each plot both histograms are normalized to the same number of entries.*

covariance of x_i and x_j is defined as [72]:

$$cov(x_i, x_j) \equiv < (x_i - \mu_i)(x_j - \mu_j) > = < x_i x_j > - < x_i >< x_j >, \tag{4.3}$$

where μ_k is the mean of x_k ($\mu_k = < x_k >$) and the symbols $<>$ represent the mean value of the quantity that appears inside. The matrix with elements $V_{ij} = cov(x_i, x_j)$ is called the *covariance matrix*. It is symmetric and non-negative. The diagonal elements of V_{ij} are the usual variance for each of the variables:

$$cov(x_i, x_i) =< x_i^2 > - < x_i >^2 = \sigma_i^2 \tag{4.4}$$

$cov(x_i, x_j)$ measures the correlation between the two variables, x_i and x_j. As the variance has dimensions, it is common to express the correlation between two variables in terms of another quantity, the *correlation coefficient* ρ_{ij}:

$$\rho_{ij} = \frac{cov(x_i, x_j)}{\sigma_i \sigma_j}. \tag{4.5}$$

ρ_{ij} is a number that can vary from -1 to 1 and measures the correlation between x_i and x_j. It is zero when x_i and x_j are completely uncorrelated. With (4.5), the covariance matrix can be expressed as:

$$\mathbf{V} = \begin{pmatrix} \sigma_1^2 & \rho_{12}\sigma_1\sigma_2 & ... & \rho_{1n}\sigma_1\sigma_n \\ \rho_{12}\sigma_1\sigma_2 & \sigma_2^2 & ... & \rho_{2n}\sigma_2\sigma_n \\ ... & ... & & \\ \rho_{1n}\sigma_1\sigma_n & \rho_{2n}\sigma_2\sigma_n & ... & \sigma_n^2 \end{pmatrix} \tag{4.6}$$

In HERA-B, the vector $\mathbf{x} = (x, y, tx, ty, Q/p)$, and $\mathbf{V}$ is a 5×5 matrix, with 15 independent elements. The comparison of the diagonal elements of the covariance matrix between data and MC can be seen in figure 4.15. The errors on the positions and on the momentum agree quite well, while the errors on the slopes (tx, ty) are larger in the MC. The errors in real data cannot be smaller than in the MC because there might be still some miscalibrations or misalignments that are not properly estimated in the real data and were not included in the MC. Therefore, a correction factor C_f was applied to the covariance matrix in the real data, to account for the unknown underestimation of the errors. The corrected track errors have the form:

$$\begin{aligned} \sigma_{tx} &= \sigma_{tx}^0 \cdot C_1 \\ \sigma_{ty} &= \sigma_{ty}^0 \cdot C_2, \end{aligned} \tag{4.7}$$

where σ_{tx}^0 and σ_{ty}^0 are the original values of the errors on tx and ty. One must be careful when correcting the covariance matrix. The diagonal elements cannot simply be multiplied by a certain factor because the resulting covariance matrix should be non-negative. To keep this property, the corrections are applied by substituting σ_{tx}^0 and σ_{ty}^0 by $C_1\sigma_{tx}^0$ and $C_2\sigma_{ty}^0$ in all the elements of the covariance matrix that depend on them:

$$\begin{array}{lcl} V_{tx,tx}^0 = (\sigma_{tx}^0)^2 & \rightarrow & V_{tx,tx} = (C_1\sigma_{tx}^0)^2 = (C_1)^2 \cdot V_{tx,tx}^0 \\ V_{tx,x}^0 = \sigma_{tx}^0\sigma_x\rho_{tx,x} & \rightarrow & V_{tx,x} = (C_1\sigma_{tx}^0)\sigma_x\rho_{tx,x} = C_1 \cdot V_{tx,x}^0 \\ V_{tx,y}^0 = \sigma_{tx}^0\sigma_y\rho_{tx,y} & \rightarrow & V_{tx,y} = (C_1\sigma_{tx}^0)\sigma_y\rho_{tx,y} = C_1 \cdot V_{tx,y}^0 \\ & ... & . \end{array} \tag{4.8}$$

The symbols V_{ij}^0 indicate the original covariance matrix elements and the V_{ij} are the corrected values. In this way, the correlation coefficients keep their original value, between -1 and 1.

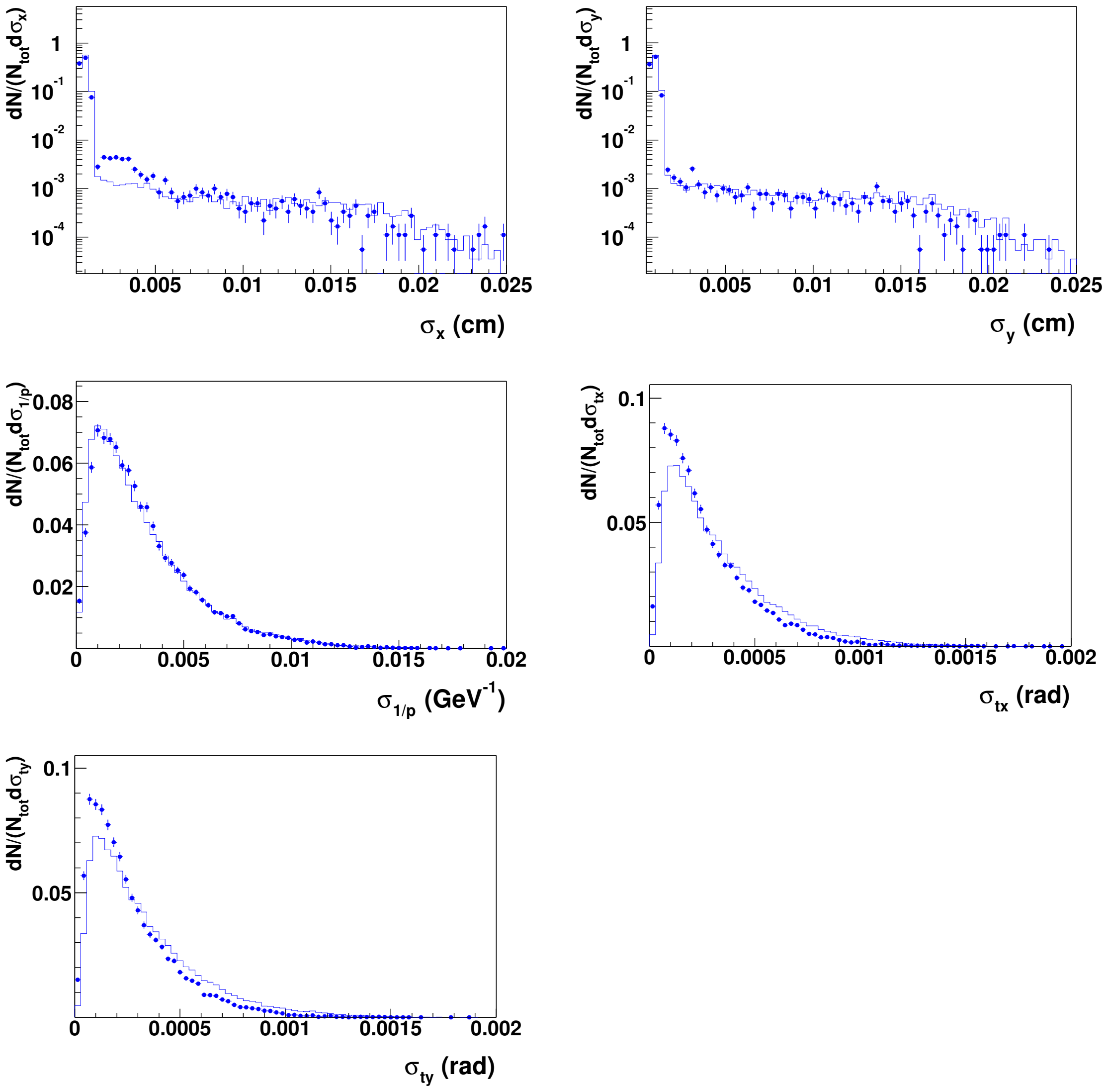

Figure 4.15: *Comparison of the diagonal elements of the track covariance matrix for MC (solid line) and real data (dots), using minimum bias events. The histograms for real data and MC are normalized to the same number of entries.*

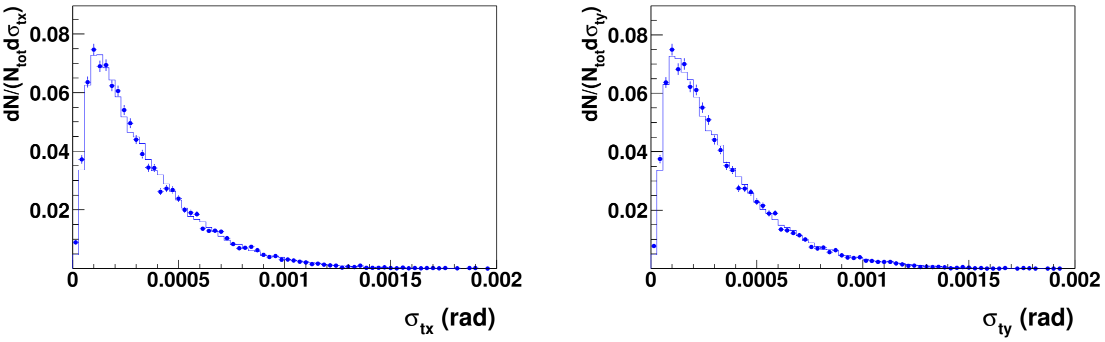

Figure 4.16: *Distributions of the errors on the slopes of the tracks (tx and ty) after the correction is applied.*

To obtain the correction factors C_1 and C_2, an iterative procedure was applied, until the distributions in MC were in good agreement with the data. The result obtained is that the correction factor for σ_{tx} and σ_{ty} are the same: $C_1 = C_2 \equiv C_f = 1.22$. Applying the correction, the distributions of the errors of the slopes in MC are in agreement with the real data for all ranges of σ_{tx} and σ_{ty} (see figure 4.16). The other covariance matrix elements (non-diagonals) are shown in figures 4.17 and 4.18, after the correction described above was applied. Some track parameters, like the momentum of the track or the position of the first measured point, do not have a big influence in the value of the impact parameter. Therefore, the small differences in some covariance matrix elements that express the correlation between those variables, like V_{xy} or V_{ptx}, are not relevant because their contribution to the total error of the impact parameter is very small.

In the studies of the following sections this correction factor will always be applied to the covariance matrix of the tracks in real data, unless the contrary is specified.

4.3.3 Primary vertex reconstruction

The default reconstruction of primary vertices in HERA-B is done with the vertexing package GROVER [58]. The standard algorithm used the z wire coordinate as a constraint for the z coordinate of the primary vertex. This method pushes the z coordinate of the reconstructed primary vertices to a region within $\pm 3\sigma$ from the wire. The main problem is that the error in z is forced to be smaller than a maximum value ($\sigma_z < 0.1\,\mathrm{cm}$), producing the unphysical distribution that is shown in figure 4.19. The statistical meaning of the error in z is lost.

The primaries can be refitted without the wire constraint, keeping all the tracks that were found by the primary vertex finder. The distribution of the resulting z coordinate

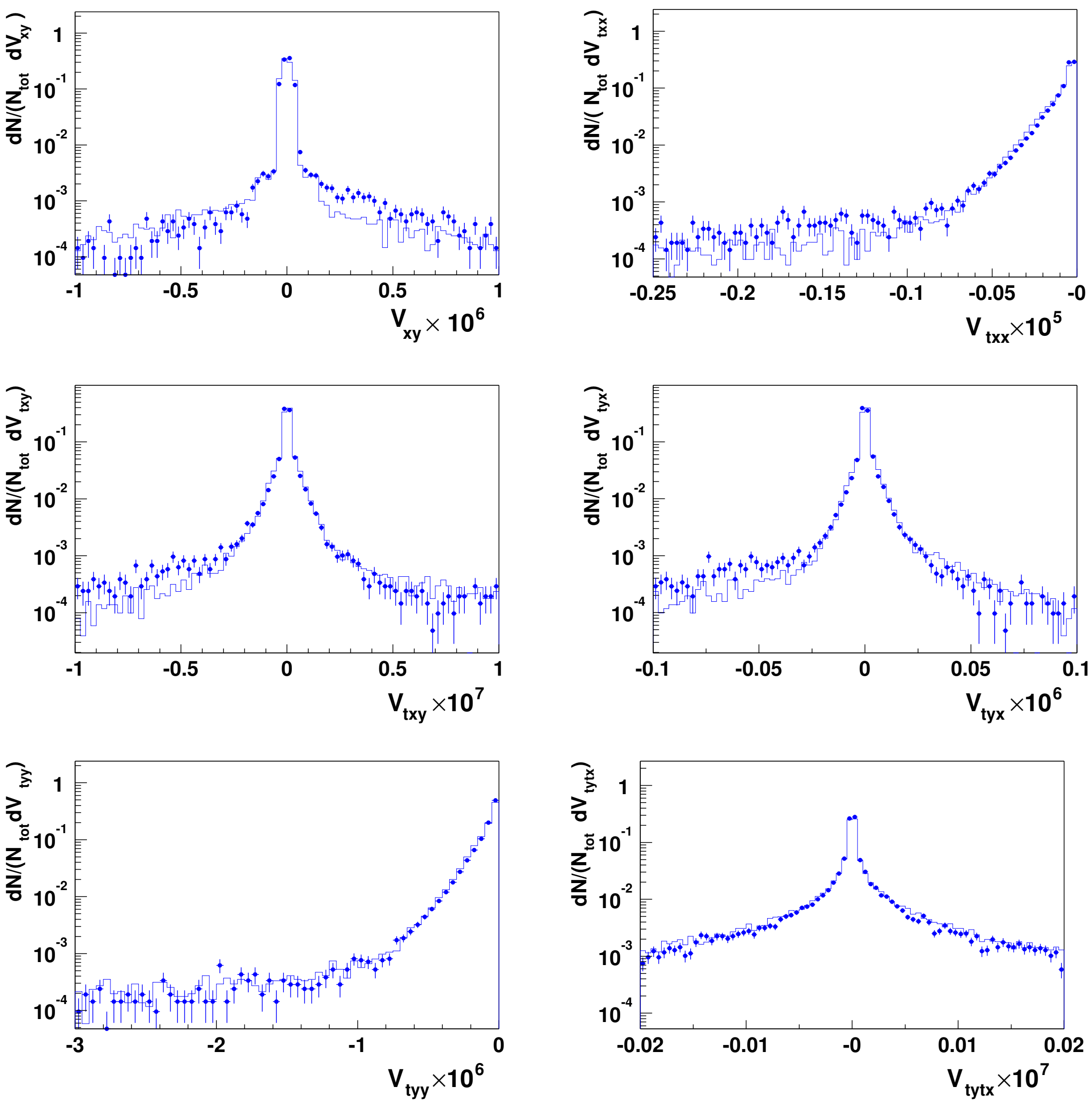

Figure 4.17: *Comparison of some of the MC non-diagonal covariance matrix elements (solid line) with the real data (full circles), after applying the correction explained in the text. The elements that express the momentum correlations with the other variables are shown in 4.18.*

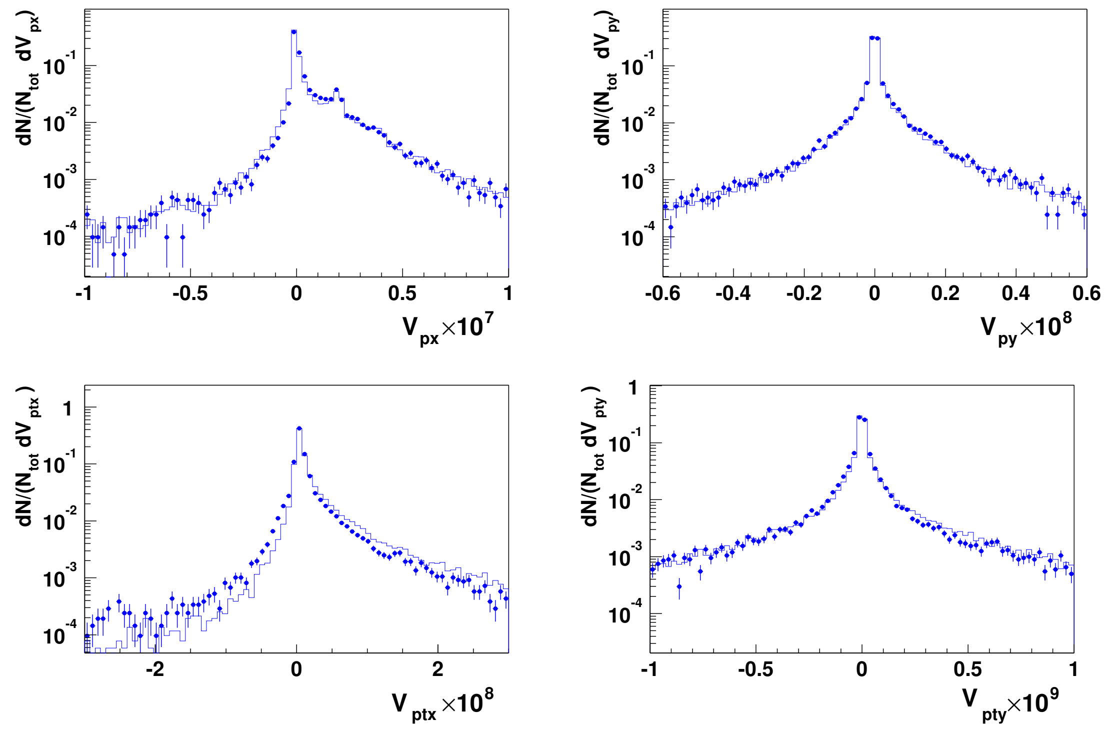

Figure 4.18: *Comparison of some of the MC non-diagonal covariance matrix elements (solid line) with the real data (full circles), after applying the correction explained in the text.*

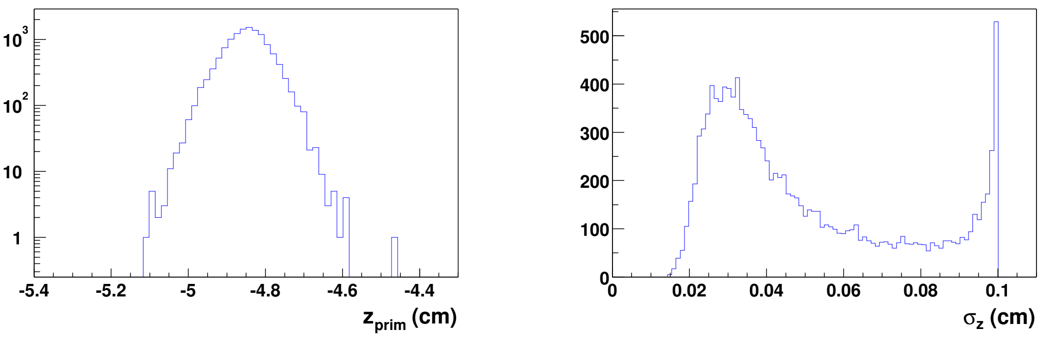

(a) (b)

Figure 4.19: *Distributions of the z coordinate of the primary vertex (a) and its error (b) for all the primaries reconstructed with wire constraint algorithm.*

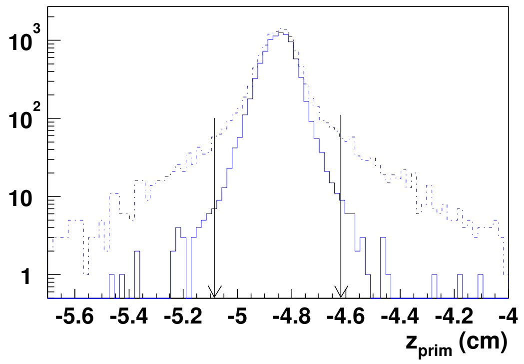

Figure 4.20: *Distribution of the z coordinate of the primary vertex after applying a refit without wire constraint (dashed line). The primaries with more than 5 tracks are shown with a continuous line. The arrows show the limits of the region within $\pm 3\sigma$ from the mean position of the wire.*

is shown in figure 4.20, with a discontinuous line. The distance $\pm 3\sigma$ from the mean wire position is marked with vertical arrows. As it can be seen, there are long tails of vertices that were reconstructed too far away from the wire to be real primaries. Rejecting vertices with less than 6 tracks most of the tails are eliminated (solid line histogram), keeping mainly the good primary vertices.

To avoid being biased by imposing the wire position, the primary vertex search was redone with a new GROVER algorithm [73] that does not apply the wire constraint. The distribution of the x,z coordinates of the primary vertex position obtained with the new algorithm are shown in figure 4.21. There are long tails corresponding to vertices that were found far away from the wire, formed by very few tracks. They can be eliminated by keeping only primaries with more than 4 tracks (solid line).

The mean of the x,z primary vertex position distributions represent the average wire position for the considered events. The width is dominated by the resolution of the primary vertex because the dimensions of the wire in x and z are small. In table 4.1 the resolution on the target position in x and z, measured as the width of the x,z distributions, are presented. The new algorithm has slightly worse resolution in z than the previous one but the errors have the proper meaning and the positions are not biased by the wire position.

The comparison of the number of tracks per vertex is shown in figure 4.22, after the selection. The difference in the first two bins is not statistically significant.

The target position in the MC sample is slightly different from the position in real data (see table 4.2). The difference in x and z position is smaller than a millimeter in

	$\sigma_x(\mu m)$	$\sigma_z(\mu m)$
Without wire constr.	57 ± 1	649 ± 11
With wire constr.	58 ± 1	549 ± 5

Table 4.1: *Resolution on the target position, measured as the width of the distribution of the primary vertex position for a large number of events, for the algorithms with and without wire constraint. Only primaries with more than 4 tracks were used to estimate the resolution.*

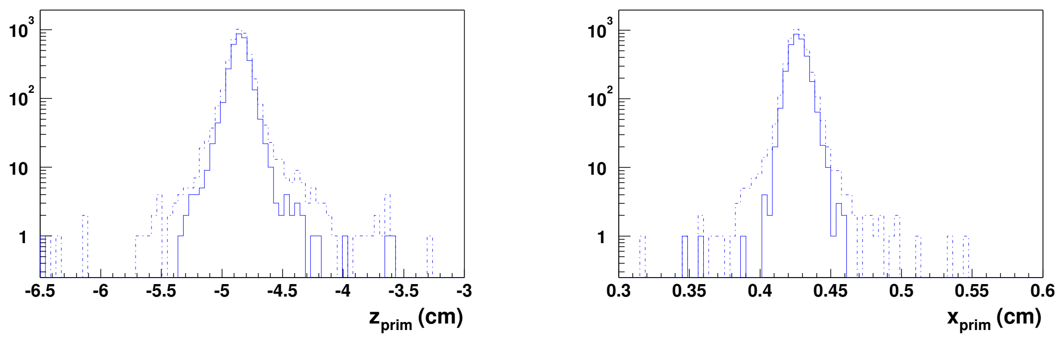

(a) (b)

Figure 4.21: *Distributions of the z (a) and x (b) coordinates of the primary vertex for all the primaries reconstructed with the new algorithm, without wire constraint. In both cases, the dashed line show all primaries found by the algorithm, and the solid line the vertices with at least 5 tracks.*

	x (cm)	$\sigma_x(\mu m)$	z (cm)	$\sigma_z(\mu m)$
MC	0.5155 ± 0.0001	42 ± 1	-4.799 ± 0.001	539 ± 6
Data	0.4268 ± 0.0001	57 ± 1	-4.852 ± 0.001	649 ± 11

Table 4.2: *Comparison of the mean positions of the target wire and the resolution in the measured position for data and MC, as obtained by averaging the primary vertex position over a large number of events. The algorithm without wire constraint was used to reconstruct the primaries.*

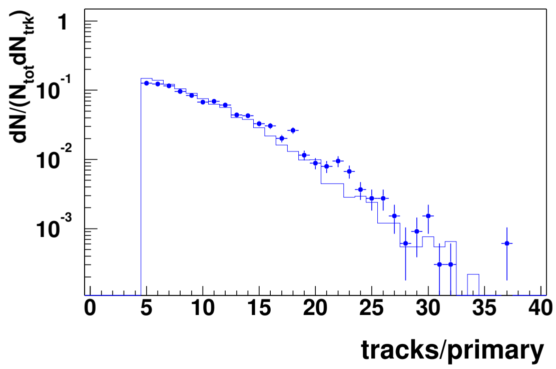

Figure 4.22: *Number of tracks per vertex for real data (dots) and MC (solid line). The new algorithm (no wire constraint) was used and only vertices with more than 4 tracks were considered.*

both cases.The impact parameter resolution could be influenced by the wire displacement if the acceptance in the VDS would change, as the resolution in the first point of the track depends on the number of hits of the VDS segment. The VDS acceptance is not modified because a displacement of half a millimeter in z would produce at most a difference of 0.1 mm in the measured x,y position of the track in the VDS, that is very small in comparison with the size of the VDS detector. This is confirmed by the fact that the number of hits in the VDS in the MC agree well with real data, as was shown in figure 4.13 (d). Therefore, the displacement of the wire won't introduce any difference between real data and MC, and the direct comparison of the impact parameter and its error can still be done.

The distribution of the primary vertex covariance matrix elements for real data and MC can be seen in figure 4.23. The differences in the first bins are small and do not have a visible influence on the error of the impact parameter, as it will be shown later.

The agreement between data and MC demonstrates that the behavior of the real data is understood, once the correction in the covariance matrix of the tracks is done and the primaries are reconstructed with an algorithm that does not introduce any bias. Nonetheless, the difference in resolution shown in table 4.2 means that in the real data the errors are not properly estimated, they should be larger than the MC to account for the difference in the resolution. This is a homogeneous effect that just modifies the shape of the significance distribution. As the impact parameter method is self calibrated the difference in the resolution does not invalidate the method.

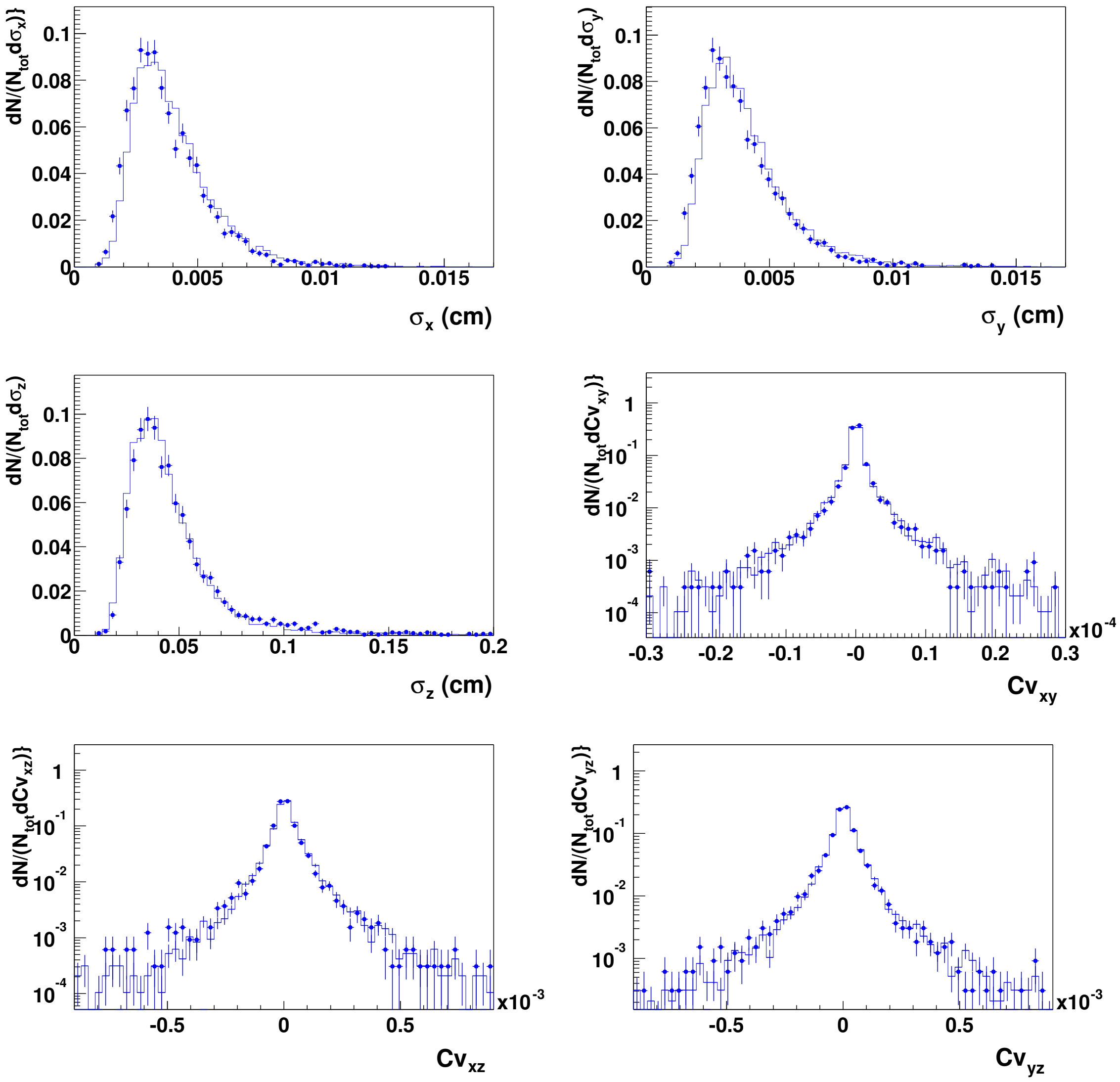

Figure 4.23: *Comparison of the covariance matrix elements of the primary vertex for real data (dots) and MC (solid line). The new primary vertex algorithm was applied, selecting only primaries with more than 4 tracks. For the real data the track covariance matrix was corrected as explained in section 4.3.2.*

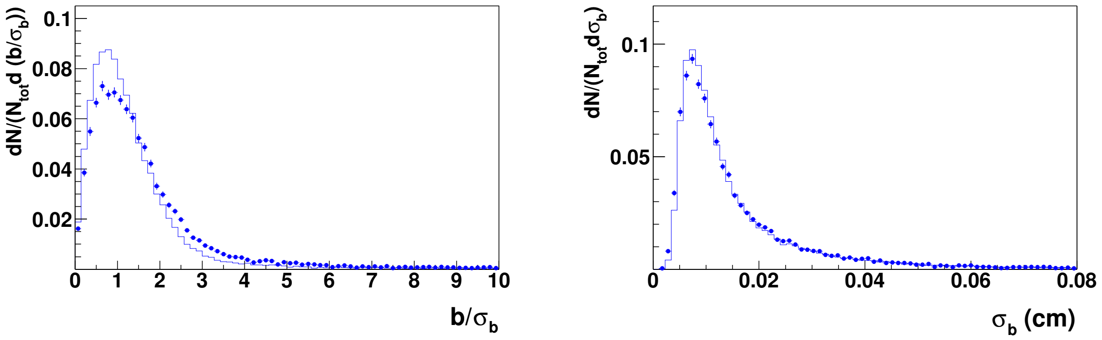

(a) (b)

Figure 4.24: *Comparison of the impact parameter (a) and its error (b) for real data (dots) and MC (solid line).*

4.3.4 Impact parameter

The track impact parameter, with respect to the primary vertex, and its error are plotted in figure 4.24 for MC and real data. The error distribution for MC agree with the real data but the impact parameter distribution does not agree. This effect points back to a difference in the resolution of the first measured point of the track, that is worse in real data, probably due to misalignments that were not included in the MC or to a wrong estimation of the intrinsic hit resolution in the real data.

To prove this point, an extra smearing was added to the MC tracks, in several different ways:

a) the slope tx of the tracks was smeared with a gaussian term of $\sigma = 0.17\,\mathrm{mrad}$. The rest of the track coordinates were kept with the original resolutions.

b) The same smearing factor was added to the other slope, ty, while keeping tx and the other coordinate with the original resolutions.

c) Both slopes were smeared with the same gaussian error, $\sigma = 0.11\,\mathrm{mrad}$. The other track coordinates were kept with the original resolutions.

The results are very similar in the three cases: the track distributions do not change because the smearing of the resolution does not influence them. The impact parameter distribution changes, decreasing the resolution in the same amount as the data, as it is shown in figure 4.25 for the case when both slopes are smeared with the same gaussian term.

Another consequence of the smearing in the track slope tx is that the resolution in the x coordinate of the primary vertex is around a 20% worse, getting more similar to

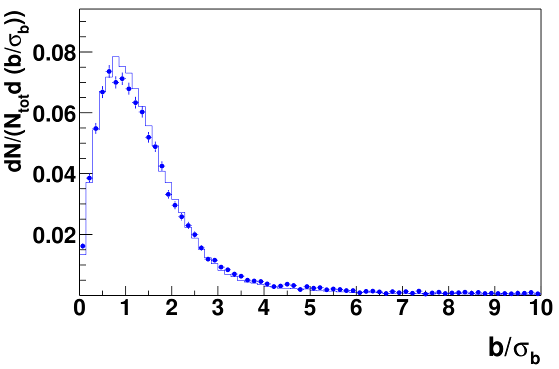

Figure 4.25: *Comparison of the impact parameter distribution for the smeared MC (solid line) and the real data (full circles).*

the real data than it was before (see table 4.2). The comparison of the x coordinate of the primary vertex for the smeared MC and the real data can be seen in figure 4.26. The distributions were centered in the same point, in order to show the agreement in the width. The smearing in ty cannot be seen in the width of the y position of the primary vertex because the wire is placed along the y direction and the distribution of y measures the width of beam and not the resolution in y.

Besides the resolution of the slopes, there can be other effects contributing to the difference in resolution of the impact parameter between the MC and the real data: the resolution in the coordinates of the first point of the track (it will not be easily seen in the impact parameter but it may affect something else, like the resolution in the RMS of the secondary vertex fit); the resolution on momentum; a combination of small differences in all the quantities or the combination of only some effects. For the purposes of this analysis it is enough to reproduce the same resolution of the impact parameter that was obtained for real data and no further understanding of the source of the discrepancy is needed. In what follows, the slopes of the tracks, tx and ty, will be smeared with the same gaussian error, $\sigma = 0.11\, mrad$ (case c), unless the contrary is specified.

4.3.5 Signed impact parameter significance

Up to now, the distributions of the unsigned impact parameter and its error were presented. To obtain the signed impact parameter distribution it is necessary to make triplets of tracks, apply a vertex fit, and calculate the sign with the procedure explained in section 4.2. In this process, only events with one reconstructed primary vertex are considered.

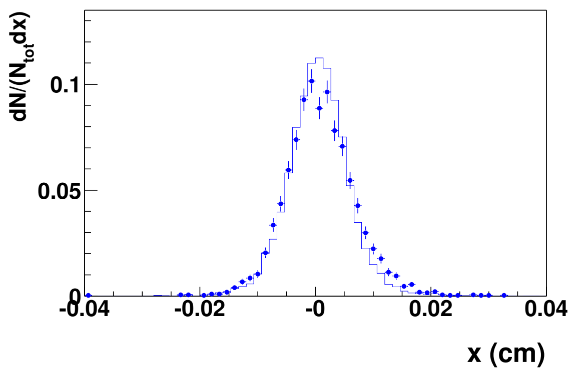

Figure 4.26: *Comparison of the x coordinate of the primary vertex in real data (full circles) and in MC, after applying the smearing in the track slopes (solid line).*

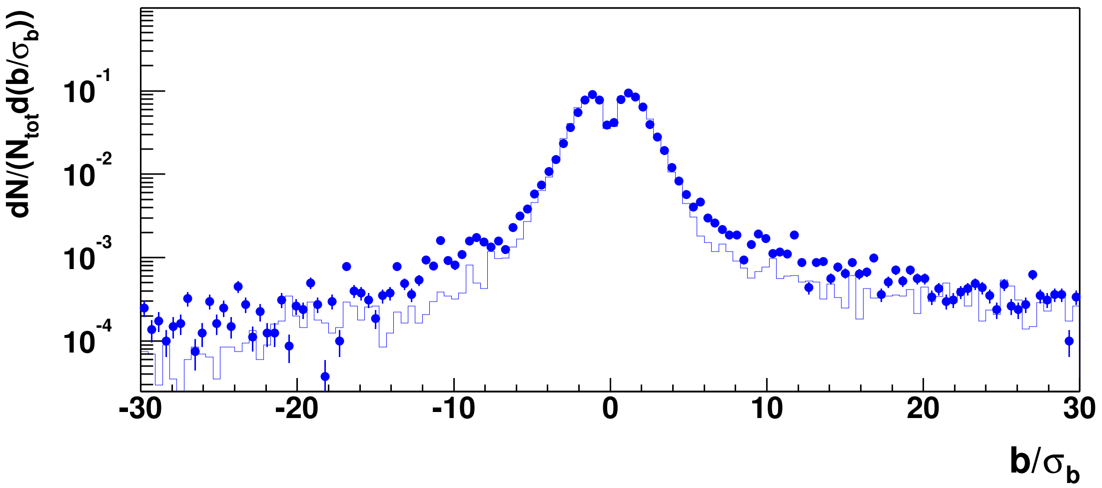

Figure 4.27: *Distribution of the signed significance for all the tracks used to reconstruct D candidates. Only events with one primary were considered.*

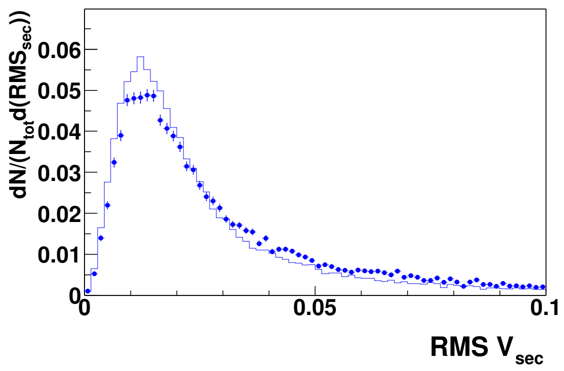

Figure 4.28: *Comparison of the RMS of the secondary vertex fit between the MC (solid line) and the real data (full circles), for all vertices with 3 tracks, in minimum bias events. Only events with one primary vertex are used. Both distributions were normalized to the same number of entries.*

The resolutions of the track slopes were smeared as explained in section 4.3.4 and the correction of the covariance matrix in the real data was applied.

The significance of the signed impact parameter, obtained in this way, is shown in figure 4.27. There are long tails in both direction, the positive and the negative side, because no requirement on the quality of the secondary vertex was applied. The agreement between real data and MC is within the errors in most of the range, demonstrating that the reconstruction in real data is well understood.

4.3.6 Other cross checks

To ensure that the quantities that are going to be used later to select the interesting decays are well understood, additional comparisons were done. One of these quantities is the root mean squared distance between the tracks and the reconstructed secondary vertex, that is used to require good quality of the vertex fit. In figure 4.28 the comparison of the RMS of the secondary vertex fit in real data and in the MC is displayed. The RMS in real data is a factor 1.11 larger than in the MC. One of the possible reasons to explain this difference can be an underestimation of the resolution of the x,y coordinates of the first measured point of the track, that won't be easily seen on the impact parameter resolution. However, the resolution in x and y cannot be the only source of this effect, as it was proved by adding an extra smearing in x,y.

To properly take into account this effect, a correction factor $C_{RMS} = 1.11$ is applied

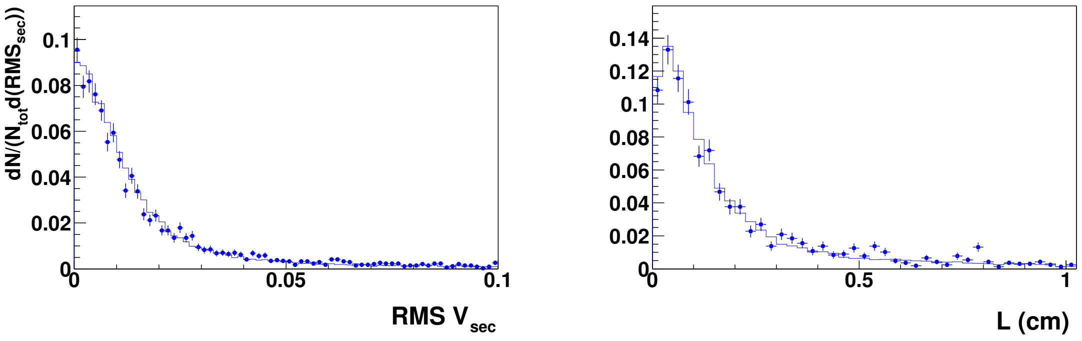

(a) (b)

Figure 4.29: *Distribution of the RMS (a) and the decay distance (b) of the vertices made of two tracks, in minimum bias events (full circles), in comparison with the MC (solid line).*

to the RMS in the MC. In this way, the efficiency of a cut on the RMS, obtained with the MC, corresponds to the expected efficiency in the real data.

For the combinations of two tracks the same cross checks were done, but two distributions were compared: the RMS of the secondary vertex fit and the distance between the secondary and the primary vertex, because these are the variables that will be used to select the D^0 decay. In the figure 4.29 these two distributions are displayed, comparing in both cases the MC (solid line) with the real data (full circles). Both, the distribution of the decay distance and the RMS of the vertex made of two tracks in the MC are in reasonable agreement with the real data, so no new corrections were applied.

4.4 Summary

A method to select the long living D meson decays has been presented. It uses a signed impact parameter significance to define the probability that a track comes from the primary vertex, and it combines the probabilities of all the daughter tracks of the long living particle. This combined probability contains enough information to successfully separate the signal from the background. An example on how to use this method in the decay $D^+ \to K\pi\pi$ was shown.

By comparing a sample of minimum bias data with the MC, it was demonstrated that, for events with only one interaction, the MC is in reasonable agreement with the real data, provided that: a) the covariance matrix in real data is corrected to account for the underestimation of the errors; b) the track slopes in the MC are smeared, in order to get the same resolution as in real data and c) the primary vertex is refitted without wire constrain and only vertices with more than 4 tracks are used.

Now, the method can be applied to the single lepton runs, in order to select the D^+ and D^0 decays and calculate the cross section ratio. In the next chapter the selection of D's will be explained, and in the last one the measurement of the ratio between the D^+ and the D^0 production cross section is presented.

Chapter 5

D meson reconstruction

The expected number of D's, in the single lepton sample, can be estimated by multiplying the D production cross section by the luminosity and the efficiency of the different analysis steps:

$$N_D = \sigma_D \cdot \epsilon_{trig} \cdot Acc \cdot \epsilon_{rec} \cdot L \cdot BR \tag{5.1}$$

The numbers that enter into the right hand side of this equation can be easily estimated. The D^+ production cross section in 800 GeV p-N collisions was measured by the E653 and the LEBC-MPS collaborations, obtaining $\sigma_{D^+} = 38 \pm 3 \pm 13\,\mu$b [74] and $\sigma_{D^+} = 22^{+9}_{-7} \pm 5\,\mu$b [75]. The energy of the HERA proton beam is a little bit larger, 920 GeV, so the D^+ production cross section should be corrected for that. As the variation in the cross section is not expected to be very large (see figure 2.5), for a first estimation of the expected number of D's it can be taken as $\sigma_{D^+} \sim 38\,\mu$b.

The percentage of D events that have a high $\mathrm{p_T}$ muon that crosses all the muon chambers or a high $\mathrm{p_T}$ electron depositing its energy on the ECAL, with $\mathrm{p_T} > 1$ GeV, is around 2%, while the probability that the lepton track is detected in the HERA-B trigger system was around 10% in the 2000 year, resulting in a total trigger efficiency of $\sim$0.2%.

The luminosity measured by the target hodoscopes can be obtained directly from the HERA-B data base. It should be corrected by the dead time in the trigger and in the data acquisition systems and by the acceptance of the carbon wire [60]. For the single muon sample (runs 17116 to 17134) the total estimated luminosity is $\sim 1.88 \cdot 10^9\,\mathrm{mb}^{-1}$. Considering the full single lepton sample, the luminosity will be 4.5 times larger, $\sim 8.44 \cdot 10^9\,\mathrm{mb}^{-1}$.

The acceptance and the tracking efficiencies, as obtained in the following chapter, are 13% and 68.3%, respectively, and the branching ratio of the decay channel $D^+ \to K\pi\pi$ is 9%. The VDS data could not be reconstructed for the $\sim$ 15% of the events collected during the single lepton runs, due to some problems in the readout electronics. Taking this into account, the total reconstruction efficiency in the measured decay channel will be 0.32%.

Joining all this numbers, around 2000 $D^+ \rightarrow K\pi\pi$ decays are expected in five million of events.

The combinatoric background can be estimated by considering the mean number of tracks per event (eight for the Single Lepton runs) and making a simple calculation: $8\times7\times6 \sim 300$ triplets of tracks per event, i.e. ~ 1470 million of background D^+ candidates. The signal to background ratio is therefore $S/B \sim 1.6 \times 10^{-6}$, illustrating the difficulty of the D reconstruction in HERA-B.

The expected number of $D^0 \rightarrow K\pi$ decays can be estimated in the same way. The cross section measured by the E623 and LEBC-MPS collaborations is the same as for the D^+. The acceptance is higher, 22%, and the tracking efficiency for the D^0 daughter tracks the same as for the D^+ daughters. Considering the branching ratio for the measured channel, $D^0 \rightarrow K\pi$ is 3.83%, the total number of expected D^0's is approximately the same as for the D^+ decays, ~ 2000. The combinatoric background will be a factor six lower than for the D^+.

The D^+ and D^0 are reconstructed in the decay channels $D^+ \rightarrow K\pi\pi$ and $D^0 \rightarrow K\pi$. The kinematic characteristics of this decays, illustrated on figure 5.1, are exploited in order to separate the signal from the background. The selection of both, the D^+ and the D^0, is based in two properties: the identification of the kaon and the long lifetime of the D meson. In a hadron collision, the majority of the particles produced are pions. To reduce the number of background combinations it is very effective to require a good kaon identification, using the RICH information. The long lifetime of the D^0 and D^+ mesons ($123.7\,\mu$m and $315\,\mu$m, respectively) provides a very good signature to identify their decays in the middle of the huge combinatoric background. However, requiring a large decay distance is not enough to separate the signal decays. The selectivity can be improved by considering also the large impact parameters of the tracks produced in the decay, using the method presented in the previous chapter. A good reconstruction of the secondary vertex is essential to ensure that the decay distance is well measured and to get the maximum profit from the impact parameter method. Requiring a small root mean squared distance between the daughter tracks and the reconstructed vertex (RMS) a good quality secondary vertex can be obtained.

The expected number of reconstructed D^+ decays, after the selection requirements, can be estimated by multiplying the number of $D^+ \rightarrow K\pi\pi$ decays in the single lepton sample with the efficiency of the event selection (section 5.1) and the D^+/D^0 selection requirements (see table 5.4 and section 6.2). Therefore, the total number of reconstructed and selected D^+ and D^0 decays will be $20 - 70$ D^+'s and $10 - 50$ D^0's, as it in indicated in the table 5.1 where all the efficiencies and relevant quantities in this calculation have

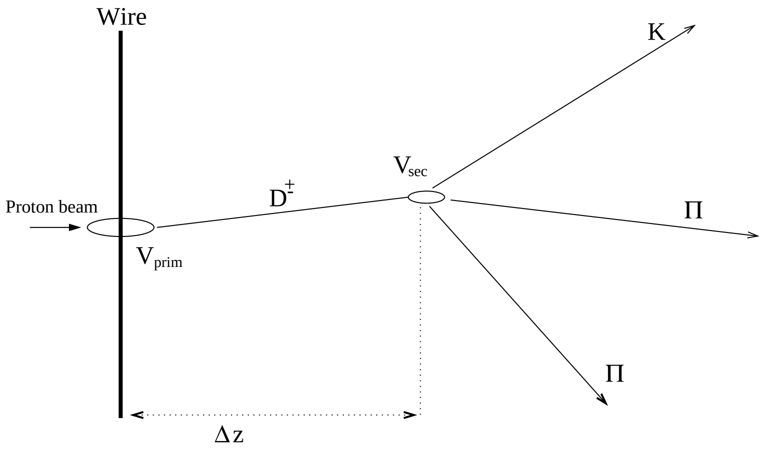

Figure 5.1: *Scheme of the $D^+ \rightarrow K\pi\pi$ decay. The primary vertex is indicated with V_{prim} and the decay vertex of the D^+ with V_{sec}.*

	D^+	D^0
Prod. cross section	$\sim 38\,\mu$b	$\sim 38\,\mu$b
Luminosity	$\sim 1.88 \cdot 10^9 (\mathrm{mb})^{-1}$	$\sim 1.88 \cdot 10^9 (\mathrm{mb})^{-1}$
Trigg. Effic.	$\sim$0.2%	$\sim$0.2%
Acceptance	13%	21%
Tracking effic.	$(69\%)^3$	$(69\%)^2$
VDS rec. events	85%	85%
Branching ratio	9%	3.83%
Ev. with 1 primary	70%	70%
Trigg.track.rec.offline	52%	52%
RMS cut	61%	88%
P_{3T}/P_{2T} cuts	47%	23%
Lifetime	—	58%
Total rec. decays	20-70	10-50

Table 5.1: *Summary of the quantities used in the calculation of the estimated number of $D^+ \rightarrow K\pi\pi$ and $D^0 \rightarrow K\pi$ reconstructed decays in the single lepton sample.*

been summarized.

In this chapter, the criteria used to reconstruct and select the signal D meson decays will be explained. In order to get the best signal to background ratio, the cuts are chosen in such a way that the significance of the signal, $S/\sqrt{B}$, is at its maximum value. S is calculated as the number of signal entries obtained with the MC for each cut and B is the background from real data, calculated by counting the number of entries in the region where the D peak must be, but using wrong charge combinations ($K^+\pi^+\pi^+$ and $K^-\pi^-\pi^-$ for the D^+; $K^+\pi^+$ and $K^-\pi^-$ for the D^0). The cuts are optimized sequentially, following the same order as it is shown here.

The data sample used in the optimization (MC and real data) was described in section 3.6.2.

5.1 Event selection

A basic event selection is applied to avoid events produced by off-bunch protons. Only events that happen in a nominally filled bunch, i.e, with a mean drift time in the OTR chambers between 56 and 66 ns and a root mean squared of the drift times smaller than 19 ns, are further considered.

In order to ensure that the impact parameter errors are calculated correctly, only events with one primary vertex are used, following the prescriptions given in the previous chapter. Badly reconstructed primary vertices are rejected by requiring that the vertex should be formed by at least five tracks. However, this condition does not ensure that the primary is reconstructed on the wire, as it can be seen in figure 4.21, where the distance between the reconstructed primary vertex and the wire was plotted. The histogram with a solid line in this figure, representing the vertices with more than four tracks, have still tails that correspond to the vertices reconstructed far from the wire. Those primaries can introduce fake lifetime, even if they are few, and they can spoil the selectivity of the method. To reject them the distance in z between the vertex and the mean position of the wire is required to be smaller than 3 times the resolution in the z coordinate of the primary vertex ($|z_{prim} - z_{wire}| < 3\sigma_z$), where z_{wire} is calculated as the average z position of the primary vertex in the single lepton sample, and σ_z is the width of that distribution, shown in table 4.2.

In table 5.2, the number of events that survive these selection criteria are shown. The percentage of events with one primary is smaller for the muon triggered events because they have higher occupancy.

To further reduce the background, only events where the trigger track was reconstructed offline were used. The SLT tracks were matched with the offline reconstructed tracks, using a χ^2 a matching criterion (see [65]). The χ^2 is defined as the sum of the

	N_{ev}	N_{eTrg}	$N_{\mu Trg}$	N_{rdm}
All	4.614 M	1.895 M	2.558 M	164 K
One primary vertex	3.219 M (70%)	1.442 M (76%)	1.765 M (69%)	14 K (8%)
Offl. trigg. track.	1.683 M (52%)	0.769 M (53%)	0.914 M (52%)	—

Table 5.2: *Total number of events for the different kinds of trigger: electron, muon, random (see table 3.2). The number of events that pass the event selection cuts are also shown for each trigger. The percentages are calculated with respect to the previous row in the table.*

squared track parameter differences in the VDS and in the OTR, divided by their errors:

$$\chi^2 = \sum_i \frac{(x_i(SLT) - x_i(VDS))^2}{\sigma^2_{x_i(SLT)}} + \sum_i \frac{(x_i(SLT) - x_i(OTR))^2}{\sigma^2_{x_i(OTR)}} \tag{5.2}$$

where $x_i = x, y, tx, ty$.

No further identification of the lepton was required, in order to keep the efficiency as high as possible. Only 52% of the events have the trigger track reconstructed offline, as it is indicated in table 5.2.

5.2 Track selection and particle identification

The track selection explained in section 3.5.5 was applied. Only tracks with a segment in the VDS and another one in the main tracker (ITR+OTR) are used. A clone removal algorithm ensures that each VDS or main tracker segment is used only once. The selection criterion favors long tracks, with many hits and small χ^2 from the refit of the track. Tracks that cross many different subdetectors are also preferred.

There are three PID detectors in HERA-B: the RICH, the ECAL and the muon chambers. The particle identification performed in this analysis uses only the information from the RICH and the muon chambers, as the identification of electrons does not help in rejecting background.

The majority of the particles produced in a proton-nucleus collisions are pions and only a $\sim$10% are kaons [49] . Therefore, out of all the daughter tracks of the D^+ or the D^0, the identification of the kaon is the most important one. The HERA-B RICH was designed to separate kaons from pions in a range of momentum between 3 and 50 GeV/c. The mean momentum of the reconstructed kaons coming from the decay of the D^+ is around 14 GeV/c (19 GeV/c for the kaons from the D^0 decay), that is well inside this range. There are several algorithms to calculate the likelihood probabilities for each mass hypothesis. The one used in this analysis is RITER [48], that takes the directions of the external

	Kaons	Pions	Protons
soft	$l_K > 0.05$	$l_\mu + l_e + l_\pi > 0.05$	$l_p > 0.05$
medium	$l_K > 0.3$	$l_\mu + l_e + l_\pi > 0.5$	$l_p > 0.3$
hard	$l_K > 0.95$	$l_\mu + l_e + l_\pi > 0.95$	$l_p > 0.95$

Table 5.3: *RICH likelihood cuts for each mass hypothesis and each selectivity level (soft, medium and hard) in figure 5.2. L_i stands for the likelihood probability of the mass hypothesis i.*

tracks as a constraint for the ring centers, as explained in section 3.5.4. The efficiency and missidentification probability for kaons, pions and protons as a function of the track momentum have been studied in [41], for three different selectivity levels (soft, medium and hard). The plots shown there are reproduced in figure 5.2 [76]. The selection criterion for each level is explained in table 5.3, where the actual values of the cuts on the likelihood probability for each mass hypothesis and for each selectivity level are shown. Electrons, muons and pions are not separated because the RICH was not designed to distinguish them and it cannot provide a definitive identification in most of the momentum range (see figure 3.9). The ECAL and the muon chambers are used for that.

For the kaon selection, it is necessary to achieve a very high selectivity because the kaon track should be separated from a huge background of pion tracks. Therefore, the cut labeled as 'hard', $l_K > 0.95$, was chosen. The efficiency, around 50% for $P > 10\,GeV$, is lower than for softer cuts, but the rejection factor for pions is better than a 99% for all momentum ranges.

A pion will be any track that is not positively identified as a kaon, a proton or a muon, i.e, the kaon and proton likelihoods, calculated in the RICH, are not too high ($l_k < 0.95, l_p < 0.85$) and the track does not have hits in the muon chambers. No positive identification of the pion track is done for the D^0. For the D^+ the combinatorial background is considerably larger, so at least one of the tracks not identified as a kaon is required to have $l_\pi + l_\mu + l_e > 0.05$. As the pions start to radiate at around 3 GeV, this cut rejects mainly ghost tracks that do not have a ring.

5.3 Vertex reconstruction

The secondary vertex is fitted with the package VT++ [77], with the standard algorithm of weighed fit[1], based on the Kalman filter [78].

[1] A similar algorithm exist in GROVER. Both vertexing packages, GROVER and VT++, have a very similar performance. It is up to the user to decide between them.

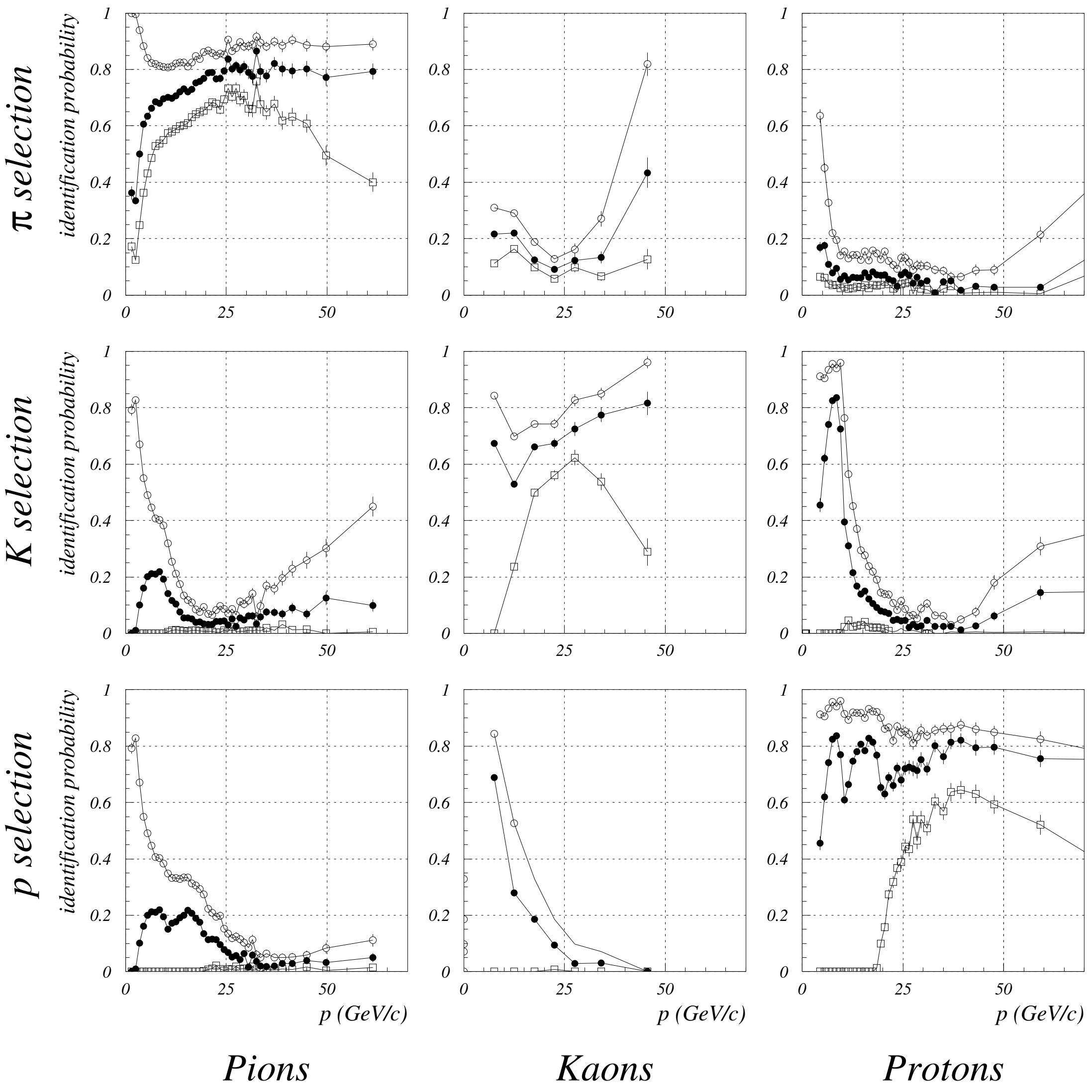

Figure 5.2: *RICH identification probability for kaons, protons and pions. The plots in the diagonal show the efficiency of the particle identification, while the off-diagonal plots show the misidentification probability (for example: the first plot in the second raw shows the probability of identifying a pion as a kaon). Three different cuts are used: soft (open circles), medium (full circles) and hard (open squares). See table 5.3 for the meaning of the cuts.*

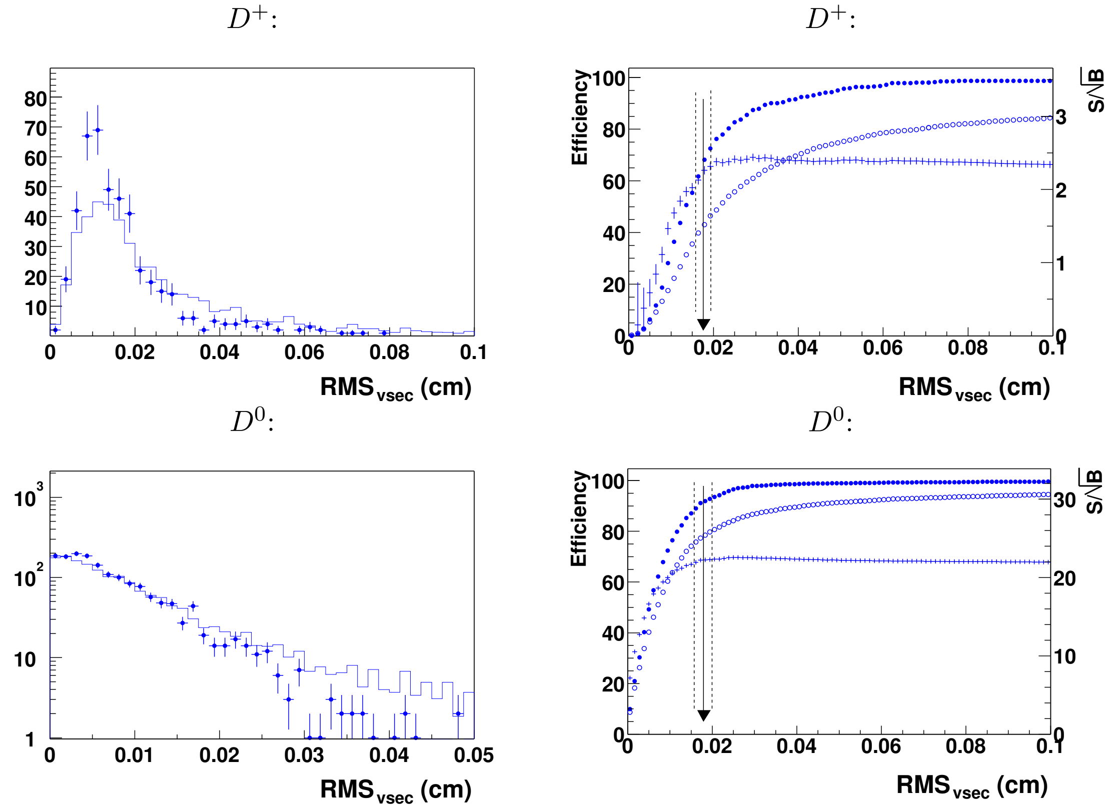

Figure 5.3: *Left: Distribution of the RMS of the secondary vertex fit for the signal from MC (full circles) and the background from real data (solid line). Right: Efficiency of a cut on the maximum RMS of the secondary vertex fit for the signal from the MC (full circles) and the background from real data (solid line) versus the cutoff value. The ratio $S/\sqrt{B}$ for each cut on the RMS of the vertex fit is shown with crosses. The upper plots correspond to the D^+ and the lower ones to the D^0.*

The distributions of the root mean squared distance between the tracks and the secondary vertex (RMS) is plotted in figure 5.3 (left) for the vertices made of two and three tracks, for the background from real data and the signal D^0/D^+ decays from the MC. The RMS for the vertices made of three tracks was corrected in the MC, taking into account the results found in section 4.3.6. The efficiency of a cut on the maximum value of the RMS and the significance of the signal are plotted in the same figure (right) as a function of the cut.

The chosen maximum RMS allowed for the D^+ and for the D^0 reconstructed vertices are shown with arrows: $RMS < 0.017\,\text{cm}$ for the D^+ and $RMS < 0.018\,\text{cm}$ for the D^0. The efficiencies for the signal D^+ and D^0 decays are 61% and 88%, respectively.

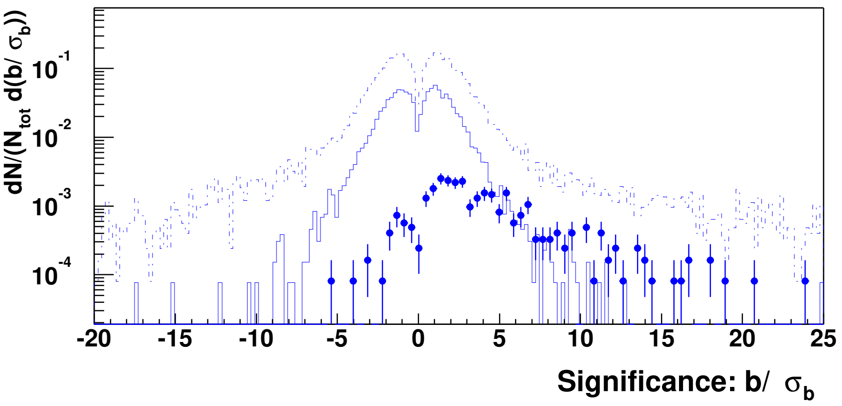

Figure 5.4: *Comparison of the significance distribution for all the tracks used to reconstruct D^+'s in the single lepton runs (solid line) and for the signal D^+ daughter tracks in the MC, after applying the PID and the RMS requirements explained in sections 5.2 and 5.3. The histogram with a dashed line corresponds to the background before applying the cut on the maximum allowed RMS. An arbitrary normalization for the signal tracks was used.*

5.4 Combined probability of the daughter tracks

The calculation of the combined probability was done following the explanations given in section 4.2. The significance distribution of all the tracks used in the D^+ reconstruction in real data (single lepton sample) is compared in figure 5.4 with the significance of the D^+ daughter tracks after applying the previous selection criteria. The histogram with a dashed line represents the significance for all the tracks in the single lepton runs before applying any requirement on the maximum value of the RMS. As it can be seen, by selecting good quality secondary vertex the tails to large positive and negative values of the significance are removed. Otherwise, they would have screened the real lifetime tracks. The tail in the positive side of the significance distribution of the signal tracks expand to very large values, while the background tails are always smaller than $b/\sigma_b \sim 10$. The significance distribution for the background from the single lepton events is symmetric, as it was expected.

The negative side of the significance distribution of the tracks from the single lepton runs was fitted with a function of the form $f(x) = c_1 x(e^{-x^2/2\sigma^2} + e^{-x/\Lambda_1}) + c_2 e^{-x/\Lambda_2}$, as it was indicated in 4.2. The result, shown in figure 5.5 (left), was used to calculate the track probability for both, the signal and the background (figure 5.5, right). In the first approximation, the track probability distribution for the real data is flat, even in the

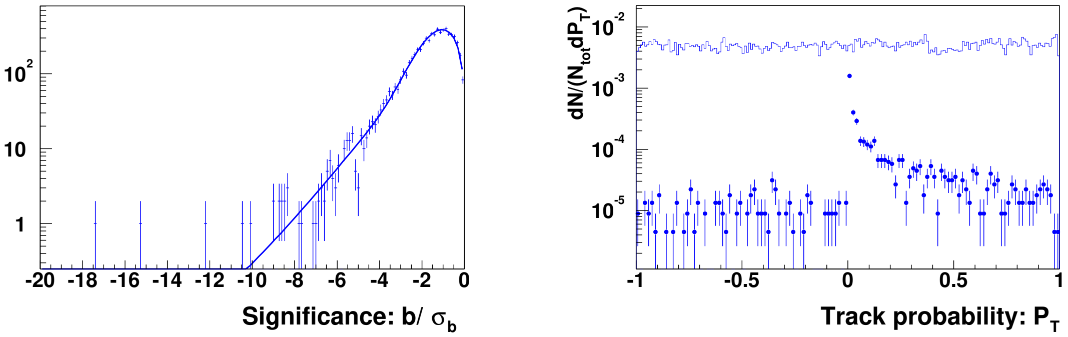

Figure 5.5: *Left: fit of the negative side of the significance distribution for the tracks used in the D^+ reconstruction in the single lepton sample, after applying the PID and the RMS cuts explained in sections 5.2 and 5.3. Right: track probability for the all the tracks in the single lepton sample (solid line) and for the D^+ daughter tracks in MC, after applying the same PID and the RMS requirements.*

positive side, demonstrating that, once a good quality secondary vertex is required, there are no background D candidates in the single lepton runs made of tracks with lifetime. The signal from the MC produce the expected spike at zero, with few cases of big or negative track probabilities, that are due to the decays that happened too close to the primary vertex, as it was explained in section 4.2.

For the $D^0 \to K\pi$ decay the impact parameter method is expected to be less powerful than for $D^+ \to K\pi\pi$ because of two reasons: first, the larger the lifetime of the particle, the larger the efficiency of the method. The D^0 lifetime is a factor three shorter than the one of D^+, so this decays will be more difficult to differentiate from the background coming from the primary vertex. Second, the larger the number of daughter tracks, the more powerful the method will be, as the combined probability condenses more information. The D^+ has one daughter track more than the D^0, so better separation power is expected in the case of the D^+.

The significance distribution of the D^0 daughter tracks, after applying the particle identification and the secondary vertex selection criteria explained in sections 5.2 and 5.3, is displayed in figure 5.6, for all the tracks used in the D^0 reconstruction in the single lepton runs (solid line) and for the signal D^0 daughter tracks in MC (full circles). In the case of the D^0 the tails are longer than for the D^+, and they are not easily removed with stronger cuts on the RMS.

The fit of the negative side of the significance distribution and the track probabilities obtained with it, are shown in figure 5.7 for the D^0 reconstruction. The fitting function has the same shape as used for the D^+. In this case, the background distribution is also

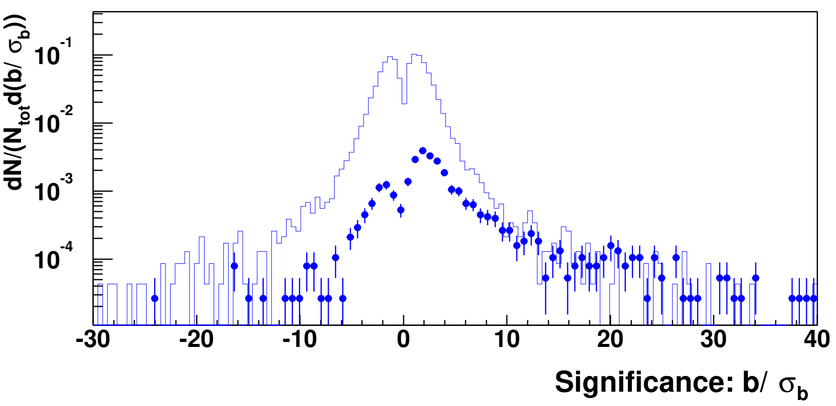

Figure 5.6: *Comparison of the significance distribution for all the tracks used to reconstruct D^0's in the single lepton runs (solid line) and for the signal D^0 daughter tracks in the MC, after applying the PID and the RMS selection requirements explained in sections 5.2 and 5.3. The normalization for the signal is arbitrary.*

flat and the signal produces a small spike at zero. The spike is not as sharp as the one for the D^+, because of the shorter lifetime of the D^0.

The track probabilities of all the daughter tracks of the D^+ (or the D^0) were combined using the expression (4.2) from section 4.2. The distribution of the combined probabilities, P_{3T} and P_{2T}, for the signal D^+ and D^0 from MC and for the background from real data are plotted in figure 5.8. The efficiency of a cut on the maximum value of the combined probability versus the cutoff value is also plotted on figure 5.8, together with the significance of the signal for each cut. As it was expected, the efficiency is lower for the D^0 than for the D^+ by a factor of two, approximately.

The selected cutoff values for P_{2T} and P_{3T} are shown with an arrow in figure 5.8. They were chosen in a compromise between increasing the significance and keeping enough statistics in real data. The values of the cuts are $P_{3T} < 0.01$ for the D^+, with an efficiency of 47% for the signal and a rejection factor of 97% for the background, and $P_{2T} < 0.015$ for the D^0, with an efficiency of 23% for the signal and a rejection factor of 95% for the background.

The efficiency of the P_{3T} cut is smaller than the one obtained in section 4.2.3, where the smearing of the track slopes had not been applied yet. The smearing of tx and ty provokes a worse resolution on the measured impact parameter and, as a consequence, it is more difficult to separate the tracks that really have large impact parameters from the background tracks coming from the primary. With the improvement in the tracking

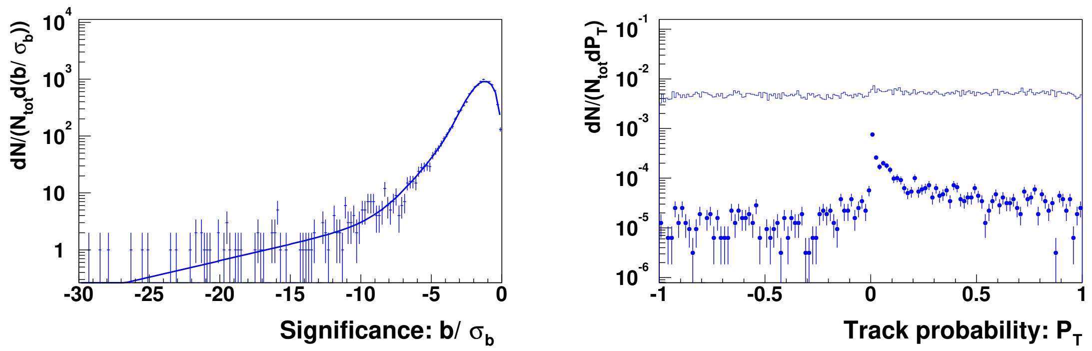

Figure 5.7: *Left: fit of the negative side of the significance distribution for the tracks used in the D^0 reconstruction in the single lepton sample, after applying the selection criteria explained in sections 5.2 and 5.3. Right: track probability for the all the tracks in the single lepton sample used in the D^0 reconstruction (solid line) and for the D^0 daughter tracks in MC, obtained with the fitting function from the left plot.*

detectors for the 2002 data taking the separation power of this method will be better, increasing the reconstruction efficiency of the D^+ and D^0 decays.

5.5 Lifetime cut

As the requirement on the combined track probability is less powerful for the D^0 than for the D^+, an extra condition on the lifetime of the reconstructed D^0 track was applied, in order to improve the significance of the signal. The distribution of the proper decay distance of the signal D^0 decays in MC and the background combination in real data can be seen in figure 5.9, after applying the selection requirements explained in the previous sections. The efficiency of a cut on the minimum D^0 lifetime versus the cut value is plotted in the same figure. The selected cut, $L > 1.6 \cdot c\tau$, marked with an arrow, has an efficiency of 58% for the signal.

5.6 Charge correlation

In a $c\bar{c}$ event where a D is produced, the high-p_T lepton that produces the trigger usually comes from the semileptonic decay of the other charmed particle, so there is a charge correlation between the kaon track and the high p_T lepton. The possibilities are the following ones (plus charge conjugated decays):

- $c \to D^+ \to K^-\pi^+\pi^+$

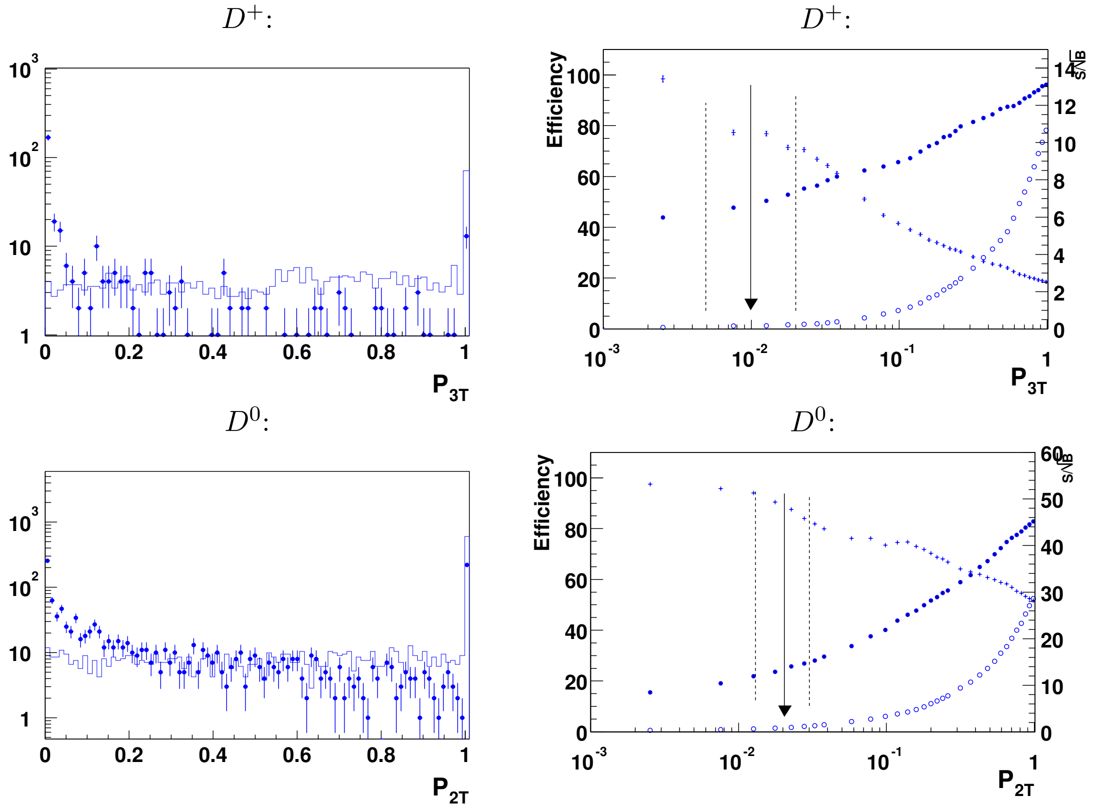

Figure 5.8: *Left: Distribution of the combined track probability of the three daughter tracks for the signal from MC (full circles) and the background from real data (solid line) versus the combined probability. Right: Efficiency of a cut on the maximum combined probability of the daughter tracks for the signal from the MC (full circles) and the background from real data (open circles). The ratio $S/\sqrt{B}$ for each cut is shown with crosses. The upper plots correspond to the D^+ and the lower ones to the D^0.*

and $\bar{c} \to l^-$, $(l = \mu, e)$.

- $c \to D^0 \to K^-\pi^+$

  and $\bar{c} \to l^-$, $(l = \mu, e)$.

The trigger track, found by the SLT, was matched with the offline reconstructed tracks using a χ^2 method, as explained in section 5.1. To keep the efficiency as high as possible no extra requirements on the identification of the lepton were applied. The kaon charge was required to be the same as the charge of the offline reconstructed trigger track. The cut reduces the background by approximately a factor 3 for the electron triggered events and close to a factor 4 for the muon triggers, for both D^0 and D^+ selected decays.

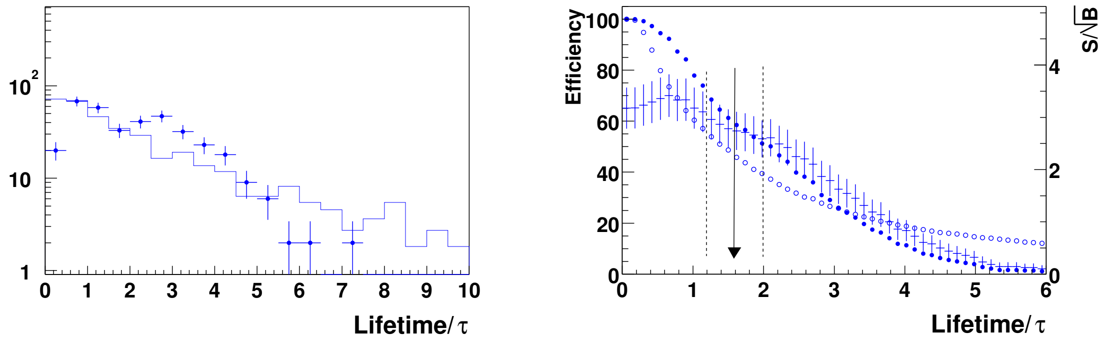

(a) (b)

Figure 5.9: *(a) D^0 lifetime distribution for the signal from MC (full circles) and the background from real data (solid line) versus the lifetime. (b) Efficiency for the signal (full circles) and for the background (open circles) of a cut on the lifetime. The signal to background ratio for each cut is plotted with crosses.*

5.7 D meson signal

The final list of selection requirements and their efficiencies (obtained from the MC) are summarized in table 5.4.

The invariant mass distribution of the reconstructed D^+ and D^0 decays that results after applying these selection criteria is plotted in figure 5.10. Both histograms were fitted to the sum of a gaussian for the signal plus a straight line for the background. The number of signal entries, as obtained from the fit, is 33 ± 9 for the D^+ and 18 ± 6 for the D^0, with a $S/\sqrt{B} \sim 3.6$ in both cases. They are compatible with the expectations presented in the beginning of the chapter. The histograms with a solid line are made of the wrong sign combinations ($K^\pm\pi^\pm\pi^\pm$ and $K^\pm\pi^\pm$) that passed the same selection criteria as the signal. They reproduce the shape of the background for the right-sign combinations.

The mean mass positions of the signal peaks, 1.872 ± 0.003 GeV for the D^+ and 1.864 ± 0.004 GeV for the D^0, are the same as expected from the MC and they are in agreement with the PDG values [37]. The width of the signal may seem a little bit narrow in comparison with the widths obtained with the MC signal when no background is considered (15 MeV for the D^+ and 20 MeV for the D^0). However, when mixing the MC truth signal, normalized to the number of entries obtained in real data, with a background coming from the real data (wrong charge combinations) the resulting width is the same as seen for in figure 5.10 (see figure 5.11). The narrow width is, therefore, just an artifact of the small statistics in the peak in addition to the background.

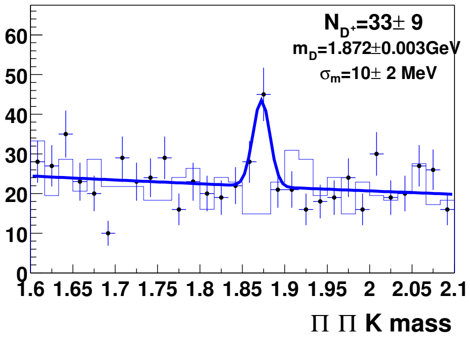

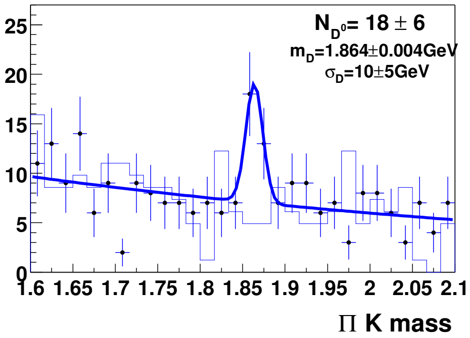

Figure 5.10: $K^{\mp}\pi^{\pm}\pi^{\pm}$ *(left) and* $K^{\mp}\pi^{\pm}$ *(right) invariant mass distribution for the single lepton triggered runs, after applying the selection requirements. The significance of the signal is* $S/\sqrt{B} \sim 3.6$ *in both cases. The histograms with a solid line are made of wrong charge combinations (*$K^{\pm}\pi^{\pm}\pi^{\pm}$ *and* $K^{\pm}\pi^{\pm}$*) that passed the same selection criteria as the signal.*

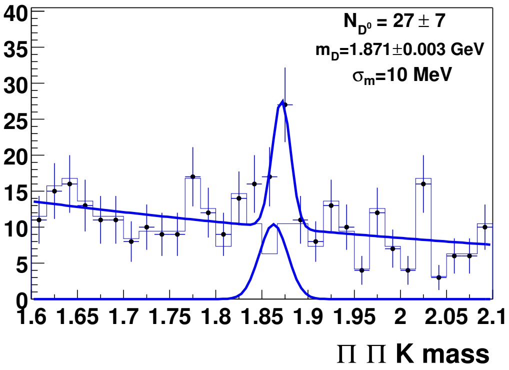

Figure 5.11: D^0 *invariant mass distribution. The signal is taken from the MC, with a number of entries similar to the number of* D^0*'s reconstructed in the single lepton sample, mixed with the background from real data (wrong sign combinations). The width of the peak seems smaller than what it really is. The gaussian drawn below shows the width of the signal peak when no background is added. The mean position of the peak may also be displaced due to the addition of the background, when the number of signal entries is small, as in this case.*

	D^+ selection		D^0 Selection	
	Cut value	Eff.	Cut value	Eff.
RMS	$< 0.017\,\mathrm{cm}$	$(61 \pm 6)\%$	$< 0.018\,\mathrm{cm}$	$(88 \pm 2)\%$
P_N	$P_{3T} < 0.01$	$(47 \pm 4)\%$	$P_{2T} < 0.02$	$(22.5 \pm 0.7)\%$
Lifetime	—	—	$L > 1.6\,c\tau$	$(58 \pm 3)\%$
Chrg. corr.	K has same charge as off. trig. track			

Table 5.4: *Summary of the selection requirements applied in the reconstruction of the D^+ and D^0 decays. Beside these, there was a common event selection: only events with one reconstructed primary vertex were considered. The efficiencies were obtained with the MC simulation data described in section 3.6.2. The errors of the efficiencies are due to the MC statistics.*

Chapter 6

Measurement of the $\sigma_{D^+}/\sigma_{D^0}$ ratio

6.1 Method

The cross section of the D^0 (D^+) production can be written as:

$$\sigma_D = \frac{N_D}{\epsilon_{trig}^{id} \cdot \epsilon_{trig}^{track} \cdot Acc \cdot \epsilon_{ev} \cdot \epsilon_{rec} \cdot \epsilon_{cuts} \cdot BR \cdot L} \tag{6.1}$$

where:

- N_D is the total number of reconstructed D's.
- ϵ_{trig}^{id} is the ideal efficiency of the trigger to select D events, i.e., the percentage of events with a D decaying in the measured channel that have a high-p_T muon or electron crossing all the trigger chambers.
- ϵ_{trig}^{track}: efficiency of the trigger system to detect the high-p_T track.
- Acc: acceptance, defined as the percentage of D decays that have all the daughter tracks inside the acceptance of the detector with respect to all the produced D decays. For a track to be inside the acceptance, it should cross the VDS and the main tracker detectors and leave a signal in at least 6 sensitive planes of the VDS and in at least 17 sensitive planes of the pattern chambers in the main tracker.
- ϵ_{ev}: efficiency of the event selection. This includes the efficiency of reconstruction and selection of primary vertices and the requirement in the number of primary vertices. It also includes the efficiency of the trigger confirmation cut.
- ϵ_{rec}: reconstruction efficiency of the D decay. It is the product of the tracking and particle identification efficiencies for each of the daughter tracks and the efficiency of the reconstruction of the secondary vertex. It can be expressed as:

$$\epsilon_{rec} = \epsilon^{D}_{trk} \cdot \epsilon_{PiD}(K) \cdot \epsilon_{PiD}(\pi) \cdot \epsilon_{vsec}(N_{dau}), \tag{6.2}$$

where ϵ^{D}_{trk} is the tracking efficiency of all the D daughter tracks, i.e., the number of D decays with all the daughter tracks reconstructed with respect to the number of D decays with all their daughters inside the detector acceptance; $\epsilon_{vsec}(N_{dau})$ is the efficiency of reconstructing a secondary vertex with N_{dau} daughter tracks. It includes the requirements on the RMS of the vertex fit.

– ϵ_{cuts}: efficiency of the selection requirements. It is the product of the efficiencies of all the selection conditions (combined probability, lifetime and charge correlation).

– BR: branching ratio of the decay used for the reconstruction of the D meson.

– L: luminosity.

The large systematic uncertainties in the trigger, event selection and detector efficiencies will introduce large errors on the measurement of the absolute value of the cross sections. Nevertheless, calculating the ratio between the D^0 and D^+ cross sections most of the quantities with large systematic errors cancel out, allowing a more accurate measurement of the ratio. The expression for the D^+ to D^0 production cross section is:

$$\begin{aligned} R = \frac{\sigma_{D^+}}{\sigma_{D^0}} = \frac{N_{D^+}}{N_{D^0}} \cdot \frac{\epsilon^{id}_{trigg}(D^0)}{\epsilon^{id}_{trigg}(D^+)} \cdot \frac{Acc(D^0)}{Acc(D^+)} \cdot \frac{\epsilon^{D^0}_{trk}(K,\pi)}{\epsilon^{D^+}_{trk}(K,\pi,\pi)} \cdot \frac{\epsilon_{vsec}(2dau)}{\epsilon_{vsec}(3dau)} \times \\ \times \frac{\epsilon_{PiD}(K)^{D^0}}{\epsilon_{PiD}(K,\pi)^{D^+}} \cdot \frac{\epsilon_{cuts}(D^0)}{\epsilon_{cuts}(D^+)} \cdot \frac{BR(D^0 \to K\pi)}{BR(D^+ \to K\pi\pi)} \end{aligned} \tag{6.3}$$

Here the efficiency of the trigger system to detect the high-p_T track has disappeared, as well as the luminosity and the event selection efficiency, as they affect both cross sections in the same way. The particle identification depends strongly on the momentum of the particles and therefore the kaon (or pion) identification probability for the D^0 and the D^+ daughter tracks may be different. The ratio must be estimated carefully. The tracking efficiency depends also on the momentum and therefore should be calculated for each of the D^+ and D^0 daughter tracks separately.

The efficiency of the reconstruction of the secondary vertex depends on the number of daughter tracks so the ratio for the D^0 and the D^+ does not cancel out .

The acceptance ratio, the ideal efficiency of the trigger to select D events, the efficiency of the selection cuts, and the ratio of the vertexing efficiencies will be estimated with the MC simulation.

The number of reconstructed D^0 and D^+ were obtained in section 5.7 by applying the selection criteria optimized in chapter 5 to the D^+ and D^0 reconstruction in the single lepton runs.

In the next section, each of the factors of the right hand side of the equation (6.3) will be evaluated and the measurement of the production cross section ratio will be obtained. The systematic uncertainties are evaluated in the following section.

6.2 Results

Ideal trigger efficiency ratio

In order to obtain the ratio between the ideal efficiency of the trigger for the D^+ and the D^0 events two samples of MC were analyzed: the $c\bar{c}$ events where a D^+ has decayed to $K\pi\pi$ ($\sim$74 K events) and the $c\bar{c}$ events where a D^0 has decayed to $K\pi$ ($\sim$200 K events). No mixing with inelastics was done, as the difference in the ideal efficiency of the trigger should come from the $c\bar{c}$ event.

Following the definition given in the previous section, the number of events that have a muon (electron) with $p_T > 1\,\mathrm{GeV}$ crossing all trigger chambers and all the muon chambers (depositing its energy in the ECAL) were calculated for the events with a D^+ or a D^0 decay. The resulting trigger efficiencies are:

- For $c\bar{c}$ events with a $D^+ \rightarrow K\pi\pi$: $\epsilon^{id}_{trig} = (1.62 \pm 0.05)\%$
- For $c\bar{c}$ events with a $D^0 \rightarrow K\pi$: $\epsilon^{id}_{trig} = (1.64 \pm 0.03)\%$.

where the quoted errors are only due to the MC statistics[1].

The ratio between them is:

$$R_{trig} = 1.01 \pm 0.04 \tag{6.4}$$

Acceptance ratio

The acceptance of the D^+ and D^0 decays is calculated with the MC simulated data, following the definition given in the previous section. The obtained values are:

- $Acc(D^+) = (13.0 \pm 0.2)\%$.

[1] In the rest of this section, the quoted errors will be the systematic uncertainties due to the statistics of the MC, unless something different is specified.

– $Acc(D^0) = (21.0 \pm 0.3)\%$.

And the resulting acceptance ratio is:

$$R_{acc} = \frac{Acc(D^0)}{Acc(D^+)} = 1.62 \pm 0.03 \tag{6.5}$$

Tracking efficiency

The total tracking efficiency for the D^+/D^0 decays was calculated as the ratio between the D decays with all their daughter tracks reconstructed with respect to the D decays with all their daughters inside the detector acceptance. A track can only be reconstructed if it has segments in the VDS and in the main tracker. The segments need to be matched correctly and the resulting track has to pass the selection criteria shown in section 3.5.5. Therefore, the track reconstruction efficiency includes the efficiency of the segment reconstruction in the VDS and in the main tracker, plus the matching and the track selection efficiencies.

The total tracking efficiencies for the D^+ and D^0 decays are:

– $\epsilon_{trk}^{D^+}(K, \pi, \pi) = (33 \pm 2)\%$.

– $\epsilon_{trk}^{D^0}(K, \pi) = (48 \pm 1)\%$.

And the ratio between them:

$$R_{trk} = \frac{\epsilon_{trk}^{D^0}(K, \pi)}{\epsilon_{trk}^{D^+}(K, \pi, \pi)} = 1.45 \pm 0.08 \tag{6.6}$$

Ratio of the particle identification efficiencies

In figure 5.2, it was shown that the efficiency of the particle identification requirements depends on the momentum. To estimate the ratio between the kaon (pion) identification for the daughter tracks of the D^0 and the D^+ it is necessary to convolute the momentum spectrum of the reconstructed kaon (pion) tracks with the efficiency from figure 5.2. The convolution is calculated by summing the products of the fraction of kaon (pion) tracks in each momentum bin times the efficiency of the particle identification for the corresponding momentum interval, as obtained from figure 5.2. The momentum distributions for the kaons and the pions coming from the D^0 and the D^+ decays in the MC are displayed in figure 6.1.

The resulting identification efficiencies are:

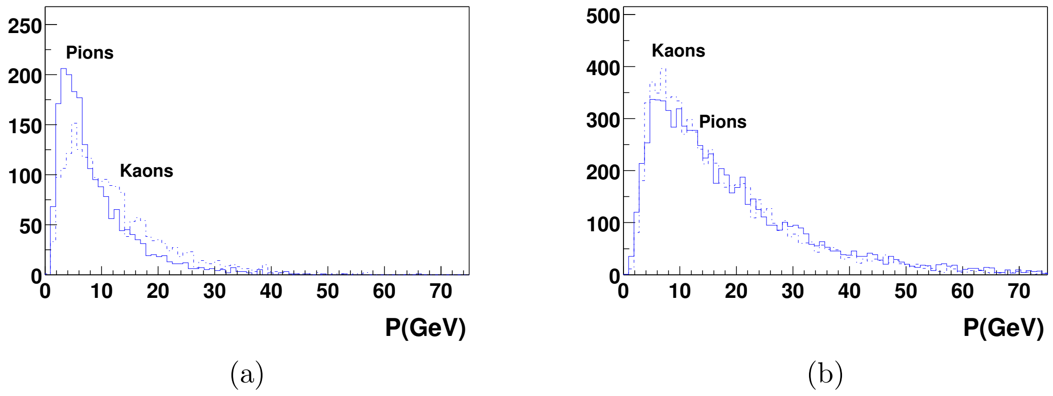

Figure 6.1: *Momentum distribution of the kaons (dashed line) and pions (solid line) coming from the D^+ decays (a) and from the D^0 decays (b).*

– D^+ decays: $\epsilon_{PiD}(\pi) = (86 \pm 1)\%$ and $\epsilon_{PiD}(K) = (23.0 \pm 0.9)\%$.

– D^0 decays: $\epsilon_{PiD}(K) = (28.8 \pm 0.7)\%$.

The errors were calculated as the quadratic sum of the errors for the efficiencies and particle fractions in each momentum interval.

The ratio between the identification efficiencies of the D^+ and D^0 daughter tracks is:

$$R_{PiD} = \frac{\epsilon_{PiD}(K)^{D^0}}{\epsilon_{PiD}(K)^{D^+} \cdot \epsilon_{PiD}(\pi)^{D^+}} = 1.42 \pm 0.05 \tag{6.7}$$

Ratio of the vertexing reconstruction efficiencies

The ratio of the efficiencies of the secondary vertex reconstruction is calculated using the MC data. From the plots shown on figures 5.3 the following numbers are extracted:

– For a vertex with three tracks: $\epsilon_{vsec}(RMS < 0.017\,cm) = (61 \pm 6)\%$

– For a vertex with two tracks: $\epsilon_{vsec}(RMS < 0.018\,cm) = (88 \pm 2)\%$.

Therefore, the ratio is:

$$R_{vrec} = \frac{\epsilon_{vsec}(2dau)}{\epsilon_{vsec}(3dau)} = 1.44 \pm 0.15. \tag{6.8}$$

Ratio of the selection cut efficiencies

The efficiency of the charge correlation requirement is the same for the D^+ and for the D^0 decay reconstruction. This can be understood as follows: the probability that the trigger selected the high-$\mathrm{p_T}$ lepton coming from one of the charm quarks is the same if the other charm quark produced a D^+ or a D^0. The same happens if the lepton that produced the trigger comes from the decay in flight of the kaon from the D meson. If the trigger was selecting any other high-$\mathrm{p_T}$ track in the event, the probability that this track has the same charge as the kaon track will be 50%, independently of how the kaon track was produced.

Therefore, for the D^+ reconstructed decays, the only requirement that enters into the so-called selection efficiency (ϵ_{cuts}) is the cut on the maximum probability that the three daughter tracks come from the primary vertex. The efficiency for the cut on P_{3T} was calculated before (see table 5.4): $\epsilon_{cuts} = \epsilon(P_{3T} < 0.01) = (47 \pm 4)\%$.

For the D^0 decays, two selection requirements should be considered: the combined probability of the two daughter tracks and the lifetime. The efficiencies are (table 5.4):

- $\epsilon(P_{2T} < 0.015) = (22.5 \pm 0.7)\%$
- $\epsilon(L > 1.6 \cdot c\tau) = (58 \pm 3)\%$

The ratio between the selection efficiencies becomes:

$$R_{cut} = \frac{\epsilon_{cuts}(D^0)}{\epsilon_{cuts}(D^+)} = \frac{\epsilon(P_{2T}) \cdot \epsilon(L)}{\epsilon(P_{3T})} = 0.28 \pm 0.03 \tag{6.9}$$

Branching ratio

The branching ratio of the reconstructed decays are the following ones [37]:

- $BR(D^0 \to K^-\pi^+) = (3.83 \pm 0.09)\%$
- $BR(D^+ \to K^-\pi^+\pi^+) = (9.0 \pm 0.6)\%$.

And the ratio between them:

$$R_{BR} = \frac{BR(D^0 \to K^-\pi^+)}{BR(D^+ \to K^-\pi^+\pi^+)} = 0.43 \pm 0.03 \tag{6.10}$$

Ratio of the cross sections

Joining all the numbers from equations (6.4), (6.5), (6.6), (6.7), (6.8), (6.9), (6.10) together with the numbers of reconstructed D^+ and D^0 decays from section 5.7, the obtained ratio between the D^0 and the D^+ production cross sections is:

$$R = \frac{\sigma_{D^+}}{\sigma_{D^0}} = \frac{33 \pm 9}{18 \pm 6} \times 1.01 \times 1.62 \times 1.45 \times 1.42 \times 1.44 \times 0.28 \times 0.43 = \\ = 1.08 \pm 0.46(st.) \tag{6.11}$$

The error quoted in (6.11) is only due to the statistics of the signal. The systematics will be evaluated in the following section.

6.3 Systematic errors

The main contributions to the systematic uncertainty in the measurement of the ratio between the D^+ and the D^0 production cross section are described in this section, following the prescriptions given in [79].

MC statistics

It is due to the limited MC statistics, specially in the channel $D^+ \to K\pi\pi$. It is obtained by summing in quadrature the errors shown in the ratios (6.4), (6.5), (6.6), (6.7), (6.8), (6.9), (6.10). The total systematic uncertainty accounts for a 18% (± 0.19).

External errors

The only external measurements that enters in the cross section ratio are the branching ratios. Their error produce a systematic uncertainty in the cross section ratio of 7% (± 0.09).

Track resolution

The resolution on the first measured point of the tracks has a big influence in the resolution of the RMS of the secondary vertex fit. The position of the track has an average error of $\sim 10\,\mu$m, as it was indicated in figure 4.15. This means that there is an uncertainty of $10\,\mu$m in the measured position of the track. Considering that the RMS is the average distance between the tracks and the reconstructed vertex, the error on the track position is equivalent also to an uncertainty of $\sim 10\,\mu$m in the RMS. To estimate how much this can affect the efficiency of the cut on the maximum allowed RMS and therefore the measured ratio between the cross sections, the RMS cut was varied by $\pm 10\,\mu$m, for the vertices with two or three tracks (separately). The range where this cut was moved is indicated with dashed lines in figure 5.3. All the numbers that enter into the production cross section ratio were calculated again, with the displaced cuts, and the maximum variation in the measured ratio was taken as the systematic uncertainty.

The variation in the ratio due to the displacement of the RMS for the vertices with two and three tracks were found to be the same, 8%. Thus, the total systematic uncertainty is 11% ($\pm$0.12).

Secondary vertex resolution

The resolution on the decay distance depend on how well the decay point is known. The resolution on the z coordinate of the secondary vertex position is around $900\,\mu$m, implying that the decay distance is not known by the same factor, $\sim 900\,\mu$m.

Considering that the average D^0 momentum is ~ 39 GeV, the uncertainty in the proper decay distance will be $\sim 4\,c\tau$. As a consequence, the cut on the minimum decay distance was moved by $\pm 0.4 \cdot c\tau$. The region where the cut was displaced is indicated in figure 5.9 with dashed lines. The calculation of the ratio between the cross sections was redone and the variation was taken as the systematic uncertainty.

It was found that the secondary vertex resolution contributes with an 18% ($\pm$0.19) systematic uncertainty to the total error on the D^+ to D^0 production cross section ratio.

Combined track probability

To estimate the systematic uncertainty in the efficiency of the cut on the maximum combined track probability, the cutoff value was moved as it is indicated by the dashed line in the figure 5.8, in an interval from $P_{3T} < 0.005$ to $P_{3T} < 0.02$, for the D^+ and from $P_{2T} < 0.015$ to $P_{2T} < 0.03$ for the D^0. As the D^+ and D^0 signal are very small, the intervals were chosen in a region where the efficiency and the $S/\sqrt{B}$ change slowly, in order not to loose the signal. The efficiencies and the number of signal entries were calculated again, with the new requirements, and the resulting cross section ratio, R, was obtained. The variation in R was taken as the uncertainty due to the imperfect knowledge of the efficiency of the combined probability requirements. The P_{3T} and P_{2T} cuts were moved independently. The variations in the P_{3T} (P_{2T}) cut produce a 10% (20%) systematic uncertainty. Adding this two uncertainties in quadrature, the total systematic error is $\pm$0.24.

Tracking efficiency

The MC data was used to calculate the tracking efficiency. Even if the MC simulation was done in a very realistic way, there are some effects like noise, misscalibrations or missalignments that are not included in the simulation and that can affect the tracking efficiency.

There is no calculation of the complete tracking efficiency in real data, but there are comparisons of the OTR tracking efficiency in MC and real data, for minimum bias events. This comparison can be used to estimate the expected difference in the efficiency measured in the MC with respect to real data. This difference can be considered as the systematic uncertainty in the tracking efficiency.

The tracking efficiency in minimum bias events (from April 2000, see section 3.6.1), for the second reprocessing of the 2000 data, was measured with two different methods [80], based on different definitions of the external tracks. In the first one, pairs of a VDS segment matched with an ECAL cluster are used. The second method uses tracks formed by a VDS segment that was matched with a RICH ring, reconstructed with the standalone package RISE (see section 3.5.4). This external tracks are required to be inside the acceptance of the outer tracker. Then, K_S^0's are reconstructed and used to estimate the efficiency of the tracking in the OTR, by requiring that the VDS-ECAl or VDS-RICH tracks are matched with an OTR-segment. The results are the following:

– Using VDS-ECAL matches as external tracks: $\epsilon_1 = (86.1 \pm 3.0 \pm 0.8)\%$

– Using VDS-RICH matches as external tracks: $\epsilon_2 = (86.9 \pm 2.3 \pm 0.6)\%$

The same method, applied to the MC simulation, gives: $\epsilon_{MC} = (84.6 \pm 2.5 \pm 1.0)\%$.

The difference between the values obtained with real data and with the MC is $\sim 2\% - 3\%$. The tracking efficiency considered in the expression (6.3) included the VDS, the ITR and the clone removal. It can be considered that a similar systematic uncertainty will arise due to the imperfect VDS and ITR simulation. Therefore, the complete uncertainty will be larger by a factor $\sqrt{2}$, i.e, $\sim$4%.

From the second to the third reprocessing of the 2000 data, the reconstruction chain was changed. The method used for the third reprocessing was explained in section 3.5. For the second reprocessing, the main differences were: the track reconstruction in the OTR was done with the same package that is used to propagate the tracks till the trigger chambers and through the magnet, RANGER; the matching algorithm for the VDS and the main tracker segments was different (it used the first measured point of the main tracker segment, in the magnet region, to do the matching); the scheme to reconstruct tracks was different, based on keeping the maximum efficiency even if the ghost rate was considerably higher and, finally, the alignment and the calibration of the subdetector were improved. However, the simulation of the detector is expected to be as good for the second reprocessing as it was for the third reprocessing. Therefore, it can be considered that for the single lepton runs in the third reprocessing, the difference between the MC simulation and the real data will be approximately the same, $\sim$4%.

The tracking efficiency enters in the cross section ratio as $\sim (\epsilon_{trk}^2/\epsilon_{trk}^3)$ and, as a consequence, a conservative factor of $\sqrt{5}$ can be added. Therefore, the total uncertainty in the D^+ to D^0 production cross section ratio due to the tracking efficiency will be $\sim$9%.

Trigger simulation

The acceptance and all the efficiencies that enter in the calculation of the D^+ to D^0 production cross section ratio should be obtained for the events that pass the trigger requirements. As it was pointed out before (section 3.6.2) it was not possible to obtain a MC sample, with enough statistics, that passed the trigger simulation. Neglecting the effects of the trigger introduces a systematic uncertainty in the measurement of the acceptance and efficiencies and, as a consequence in the production cross section ratio.

In principle, the selection requirements, like the RMS of the secondary vertex fit, the combined probability or the lifetime should not be affected by the presence, in the same event, of a high-p_T lepton. The acceptance and tracking efficiencies, for instance, could be modified, specially if there are triggers produced by the decay in flight of the kaon coming from the D^+/D^0, as it was suggested in [47]. Therefore, the acceptance and the tracking efficiency were calculated again for the D^+/D^0 events that have a high-p_T lepton fulfilling the trigger conditions. The variation on the ratio between the D^+ and the D^0 production cross section, estimated to be smaller than a 1%, was taken as the systematic uncertainty.

MC fragmentation model

The sistematic uncertainty in the extrapolation of the cross section from the HERA-B acceptance to the total angular coverage was estimated using different fragmentation models. Two different MC samples were generated for each fragmentation model at generator level (i.e., without simulating the detector effects): $c\bar{c}$ events where a $D^+ \to K\pi\pi$ was produced and $c\bar{c}$ events where a $D^0 \to K\pi$ was produced. The following fragmentation models were used:

a) Full string fragmentation [68].
b) Independent fragmentation [68].
c) Keeping all fragments from the proton-nucleus collision [68].

In each case, the ideal trigger efficiency (defined as in section 6.1) was calculated separately for the events with a D^+ and for the events with a D^0 decay. The acceptance

Fragmentation model	Variation in the ratio (6.12)
a)	2%
b)	15%
c)	4%

Table 6.1: *Variation in the ratio between the product of the trigger efficiency and the acceptance for the D^0 and the D^+ decays, using different fragmentation models.*

for the D^+ and D^0 decays was calculated using the definition given in section 6.1. The variation in the ratio

$$R_{geo} = \frac{\epsilon^{id}_{trg}(D^0) \cdot Acc(D^0)}{\epsilon^{id}_{trg}(D^+) \cdot Acc(D^+)} \tag{6.12}$$

was taken as the systematic uncertainty due to the extrapolation of the cross section ratio from the acceptance of the HERA-B detector to all the angular coverage. On table 6.1 the variation of the ratio (6.12) for the different MC fragmentation models is shown. The maximum variation, 15% is the total systematic uncertainty.

Other effects, like variations in the kinematical distributions of the D^+ and D^0 decays, were checked for all the fragmentation models and they were found to be negligible.

The list of all the systematic uncertainties and the total error of the cross section ratio are summarized in table 6.2.

6.4 Result for the $\sigma_{D^+}/\sigma_{D^0}$ ratio

Joining all the systematic uncertainties, the resulting value of the ratio between the D^+ and the D^0 production cross section is:

$$\begin{aligned} R = \frac{\sigma_{D^+}}{\sigma_{D^0}} &= 1.08 \pm 0.46(st.) \pm 0.09(syst.extern.) \pm 0.19(syst.MCstat.) \pm \\ &\pm 0.10(syst.tr.eff.) \pm 0.12(syst.tr.res.) \pm 0.19(syst.V_{sec}res.) \pm \\ &\pm 0.24(syst.P_{2T}, P_{3T}) \pm 0.16(syst.fragm.) \pm 0.01(syst.trig.sim.) \end{aligned} \tag{6.13}$$

And adding up all the errors quadratically:

$$\boxed{R = 1.08 \pm 0.46(st.) \pm 0.41(syst.) = 1.08 \pm 0.63}$$

Source	Uncertainty in R (%)	Total uncertainty in R
Statistical error	43%	±0.46
MC statistics	18%	±0.19
external	7%	±0.09
tracking efficiency	9%	±0.10
track resolution	11%	±0.12
V_{sec} resolution	18%	±0.19
Cut on P_{2T}	20%	±0.22
Cut on P_{3T}	10%	±0.11
No trigg. simul.	1%	±0.01
Fragmentation model	15%	±0.16
Total	59%	±0.63

Table 6.2: *List of the systematic uncertainties that affect the calculation of the ratio between the D^+ and the D^0 production cross section in the analysis presented in this thesis.*

This value is in agreement with the results found by other $p-N$ experiments (see figure 6.2). Due to the large error, it is compatible with the theoretical expectation, within 1.3σ. This measurement clusters with the results obtained by other $p-N$ collision experiments at high proton beam energies, stating that the D^+ and the D^0 production cross sections are equal. The result obtained here is the first one that uses a different method, based on a direct calculation of the ratio, instead of measuring the two cross sections separately.

6.5 Cross checks

Besides the systematics uncertainties studied in the previous sections, there might be some systematic effects due to the analysis method. Some cross checks were done in order to verify that the method is not introducing any biases in the measured value of the ratio R.

Invariant mass fit

Some changes on the invariant mass fitting function were done in order to study the systematic effects of the fit:

- the description of the background was changed to an exponential instead of a linear function;
- the binning was modified, increasing and decreasing the number of bins by a 30%;

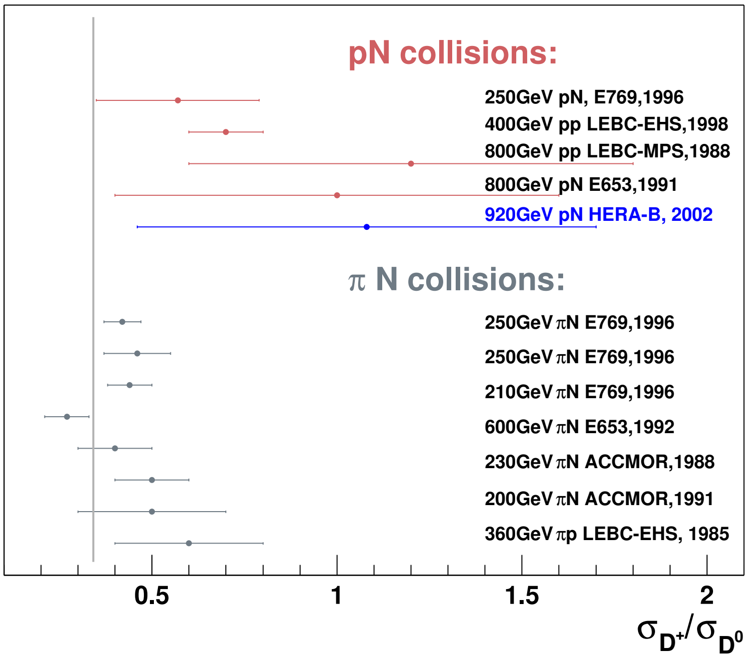

Figure 6.2: *Experimental measurements of the D^+ to D^0 production cross section ratio. The theoretical prediction is shown with a grey line. The HERA-B measurement is shown with a blue point.*

– the mean mass position was fixed to the PDG values, to reduce the number of parameters used in the fit.

The variation in the number of signal D mesons is shown in the table 6.3 In all the cases, the number of signal entries was compatible with the results presented in section 5.7, within 1σ, demonstrating that there is no systematic effect in the fitting procedure.

Charge correlation

The systematic effects due to the requirement in the kaon charge were checked by requiring an anti-correlation, i.e., the kaon track should have the opposite charge as the offline reconstructed trigger track. This trigger mode can be produced in the case of the following beauty hadron decays (plus charge conjugated modes):

$B^0 \to \mu^+ D^- X$ with a μ^-/e^- coming from the b quark.

$B^+ \to \mu^+ \bar{D}^0 X$ with a μ^-/e^- coming from the b quark.

Change	N_{D^+}	N_{D^0}
Backg.: exponential	33 ± 9	18 ± 6
Numb.bins incr. by 30%	30 ± 9	16 ± 6
Numb.bins decr. by 30%	23 ± 7	22 ± 17
Fixed mass to PDG value	33 ± 9	18 ± 6

Table 6.3: *Variation in the number of signal D^+, D^0 decays when changing the fitting function.*

A simple calculation, similar to the one presented at the beginning of chapter 5, can be done to estimate the number of D^+'s (D^0's) coming from $b\bar{b}$ pairs. The $b\bar{b}$ cross section is around thousand times smaller than the D^+ or D^0 production cross section, but the trigger is $\sim$10 times more effective. Taking into account that the b quark decays into a D 20% of the times, the resulting number of D mesons coming from the decay of a beauty hadron will be a factor 2×10^{-3} smaller than the number of D's coming from $c\bar{c}$ events, i.e., < 0.1. As a consequence, no D peaks can be seen in the invariant mass plot when requiring a charge anti-correlation. This was exactly what was observed in the real data, demonstrating that there are no D's coming from beauty hadrons and that the correlation requirement is not artificially increasing the peak.

Track probability calculation

In order to check the possible biases on the fit of the negative side of the significance distribution, the fitting function can be changed, describing the tails in a different way, for example. However, as soon as it describes the shape of the distribution correctly no differences are observed in the track probability distribution and therefore on the combined probability. A better approach is to use a different selection of tracks to do the fit, as this method describes better the possible biases of the whole probability calculation.

The procedure used in this analysis consisted of optimizing the cuts in a different order, in such a way that the fit of the significance distribution is done for a different selection of tracks. In addition, the optimization was done considering the significance of the signal as $S/\sqrt{S+B}$, where S is the number of signal entries in the MC and B is the number of background entries in real data, obtained with the wrong sign combinations.

The scheme is the following one:

- The particle identification was done with slightly different requirements:
  - Kaon track (for the D^+ and the D^0 reconstruction): $l_K > 0.95$.
  - D^0 decay: the non-kaon track was required to verify $l_e + l_\mu + l_\pi > 0.05$.

- D^+ decay: at least one of the tracks not identified as a kaon should verify $l_e + l_\mu + l_\pi > 0.05$.

- Vertexing: the maximum RMS required for a reconstructed vertex with three tracks was relaxed, $RMS < 0.02\,\text{cm}$. For the vertices with two tracks the maximum RMS required was the same as in section 5.3: $RMS < 0.018\,\text{cm}$.

- Charge correlation: the kaon track should have the same charge as the offline reconstructed trigger track. The efficiency of this condition was not calculated exactly, due to the impossibility of simulating the trigger chain in the MC, but it is assumed to be the same for the D^+ and for the D^0 decays, as explained in section 6.2.

- The impact parameter significance distribution of all the tracks that fulfill the previous requirements is fitted. Then the track probability and the combined probability of the daughter tracks are calculated and the cutoff value for the maximum combined probability is found by maximizing the significance of the signal, $S/\sqrt{S+B}$. It is important to notice that the tracks used for the fit of the impact parameter significance are different from the ones used in section 5.4, as the particle identification and RMS conditions are different, and here the charge correlation requirement is applied before the combined probability.

  After the optimizations, the chosen cutoff values for the maximum combined probabilities, P_{2T} and P_{3T} were 0.014 and 0.015, respectively.

- For the D^0 decay, a further cut on the minimum lifetime was applied. The cutoff value, $L > 1.9\,c\tau$ was stronger than the one required in section 5.5.

The efficiencies for the selection criteria are summarized in table 6.4.
With the new requirements, the numbers of signal D mesons obtained are the following:

- Number of $D^+ \to K\pi\pi$: 41 ± 11.

- Number of $D^0 \to K\pi$: 13 ± 5.

with a significance better than three in both cases.

Repeating the analysis done in section 6.2, the D^+ to D^0 cross section ratio is

$$R = \frac{\sigma_{D^+}}{\sigma_{D^0}} = 1.06 \pm 0.50(stat.) \tag{6.14}$$

where the quoted error is only statistical. This value differs from (6.11) by less than a 2%, confirming that the selection of tracks used in the fit of the impact parameter significance does not introduce any bias in the cross section ratio. This result also verifies that the

	D^+ selection		D^0 Selection	
	Cut value	Eff.	Cut value	Eff.
PID Kaon	$l_K > 0.95$	23%	$l_K > 0.95$	28.8%
PID Pion	One non-K track $l_e + l_\mu + l_\pi > 0.05$	86%	non-K track $l_e + l_\mu + l_\pi > 0.05$	85%
RMS	$< 0.020\,\text{cm}$	73%	$< 0.018\,\text{cm}$	91%
charge corr.		—		—
P_N	$P_{3T} < 0.014$	50%	$P_{2T} < 0.015$	22%
Lifetime	—	—	$L > 1.9\,c\tau$	49%

Table 6.4: *Summary of the D^+ and D^0 selection requirements done for the cross check done. The cuts were optimized in the same order shown in the table, maximizing the significance of the signal $S/\sqrt{S+B}$, where S is the number of signal entries in MC and B is the number of background entries in real data (wrong sign combinations). The event selection was done in the same way as explained in 5.1. The efficiency of the charge correlation requirement is assumed to be the same for the D^+ and for the D^0, as explained in section 6.2.*

selection requirements can be optimized in a different way without changing the final result.

RMS correction factor

To cross check that the correction factor applied to the RMS of the vertices with three tracks was correct, the MC was reconstructed in a different way. The smearing in the slope ty was not applied. Instead, a smearing of 0.17 mrad was applied to the slope tx. As explained in section 4.3.4, this smearing in tx can perfectly simulate the difference between the resolution of the impact parameter in MC and in real data, while keeping the good agreement in other track distributions. The RMS distribution in MC was compared again with the real data. It was found that it disagrees with the real data by a factor that is compatible with the correction factor found before ($C_{RMS} = 1.11$).

This proves that, as long as the corrections applied to the resolution of the track slopes in the MC reproduce the same impact parameter resolution as observed in the real data, the difference between the RMS distribution in MC and in real data will be the same. Then, the correction factor was properly estimated and it is stable.

Chapter 7

Summary and conclusions

Heavy quark production and hadronization provides a benchmark process for testing perturbative QCD. Although there are many experimental results in this field, not all of them are in agreement with the theoretical expectations. One point where the experimental results do not agree with the theoretical prediction is the ratio between the D^+ and the D^0 production cross section. The theory states that the D^+ production cross section should be around three times smaller than the D^0 cross section. The experimental results for $\pi - N$ collisions are close to the predicted value, while the $p - N$ experiments obtain larger ratios. There is no reasonable theoretical explanation for the fact that proton-nucleus and pion-nucleus experiments give different results. More experimental measurements in $p - N$ collisions can help to reduce the errors and provide a better understanding of the process.

The aim of this thesis is to obtain a new measurement of the D^+ to D^0 production cross section for 920 GeV proton-nucleus collisions, with the HERA-B detector. The data sample used consisted of 5 million events taken with a high-p_T lepton trigger, at the end of the 2000 run period.

The published values of the D^+ to D^0 production cross section ratio [14] were obtained by measuring the two cross section separately. In this analysis, the production cross section ratio was computed directly, by measuring the number of reconstructed D^+ and D^0 decays in the single lepton sample and calculating the ratios of the reconstruction efficiencies with the Monte Carlo simulation. In this way, some of the uncertainties cancel out in the calculation and the final systematic uncertainty is smaller.

In order to select the D^+ and the D^0 decays, a method to reconstruct and select the decays of long lived particles was developed. The method is based on the definition of the signed impact parameter significance of a track with respect to the primary vertex. The tracks with negative impact parameter are identified as being produced at the primary vertex. They are used to define the probability that a track with a certain impact parameter significance was produced at the main interaction vertex. The probabilities of all the tracks produced in the decay of the long lived particle are combined in one quantity that represents the total probability that any group of tracks without lifetime produce the set of observed impact parameter significances or any other set equally or more unlikely. The combined track probability was proved to be very effective to separate the signal D meson decays.

Before applying the impact parameter method to the D^+ and D^0 reconstruction in real data, the track and primary vertex errors were studied by comparing a sample of minimum bias data with the MC simulation in order to prove that the errors are correctly estimated in the real data. Some discrepancies were found and corrected.

The method was applied then to the reconstruction the D^+ and the D^0 decays. The optimization of the selection criteria was done by maximizing the significance of the signal, defined as $S/\sqrt{B}$, where S is the number of signal entries in the MC and B is the background in the real data. The final sample of D mesons consisted of 33 ± 9 $D^+ \to K\pi\pi$ decays and 18 ± 6 $D^0 \to K\pi$ decays.

The ratio between the D^+ and the D^0 production cross section, at $920\,\mathrm{GeV}$ $p-N$ collisions was obtained:

$$R = \frac{\sigma_{D^+}}{\sigma_{D^0}} = 1.08 \pm 0.46(st.) \pm 0.41(syst.) = 1.08 \pm 0.63$$

This value is in agreement with the other measurements in $p-N$ collisions and clusters with the results obtained by the experiments with a high energy proton beam, stating that the D^+ and D^0 production cross sections are equal. However, this result is still compatible with the theoretical expectations, within 1.3σ, due to the large errors.

The measurement done in this analysis can be improved with the data that will be collected during the 2002-2003 run. The improvement in the detector performance, especially in the trigger and tracking systems, can increase the selectivity of the impact parameter method, permitting a more efficient selection and reconstruction of the D meson decays. A sample with more statistics would help to reduce the statistical uncertainty, that is still the dominant contribution to the total uncertainty in the measurement presented here.

Appendix A

Calculation of the impact parameter error

In this appendix, the calculation of the impact parameter error, presented in section 4.2, will be explained.

Consider the track shown in figure A.1, that is determined by its direction (the momentum, $\vec{p} = (p_x, p_y, p_z) = p_z(tx, ty, 1)$) and the first measured point ($T_0 = (x_0, y_0, z_0)$). The primary vertex is shown with a point, indicated by V^0.

Defining

$$\hat{u}_0 = \frac{\vec{P}}{|\vec{P}|} = (tx, ty, 1) \cdot \frac{1}{\sqrt{tx^2 + ty^2 + 1}}, \tag{A.1}$$

the impact parameter, b, of the track is given by the expression:

$$b = |\vec{T_f} - \vec{V^0}| = |\vec{T^0} - \Delta\hat{u}_0 - \vec{V}|, \tag{A.2}$$

where $\Delta = (\vec{T_0} - \vec{V}^0) \cdot \hat{u}_0$.

The error on the measured impact parameter can be expressed as [71]:

$$\sigma_b = \left(\hat{b} \cdot \frac{\partial \vec{b}}{\partial x_i}\right)\left(\hat{b} \cdot \frac{\partial \vec{b}}{\partial x_j}\right)\sigma_{ij}, \tag{A.3}$$

where $\hat{b}$ is a unitary vector in the direction of the impact parameter, as indicated in figure A.1. The x_i are all the coordinates used in the calculation of the impact parameter, i.e., the track plus the vertex coordinates $(x_0, y_0, tx, ty, v_x^0, v_y^0, v_z^0)$.

σ_{ij} is the covariance matrix of the coordinates from the track and the vertex. Considering that there is no correlation between the measured track and vertex positions [1] the

[1]As the primary vertex is reconstructed without the tracks that are used in the reconstruction of the D decay, there is no correlation terms between the tracks and the vertex.

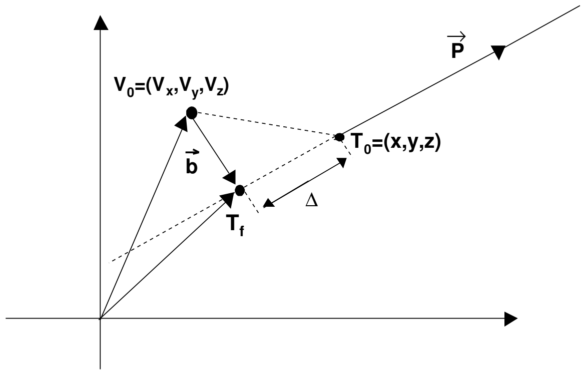

Figure A.1: *Scheme of the impact parameter calculation.*

covariance matrix can be written as:

$$\sigma_{ij} = \begin{pmatrix} \sigma^{V^0} & | & 0 \\ ----- & ---- & ----- \\ 0 & | & \sigma^{Tr} \end{pmatrix} \tag{A.4}$$

In this expression σ^{V^0} represents the covariance matrix of the primary vertex, and σ^{Tr} the covariance matrix of the tracks.

The equation (A.3) can be written as a separate sum over the derivatives of the impact parameter with respect to the track coordinates and the derivatives with respect to the vertex coordinates:

$$\sigma_b = \left(\hat{b}\cdot\frac{\partial\vec{b}}{\partial x_i^{Tr}}\right)\left(\hat{b}\cdot\frac{\partial\vec{b}}{\partial x_i^{Tr}}\right)\sigma_{ij}^{Tr} + \left(\hat{b}\cdot\frac{\partial\vec{b}}{\partial x_i^{V^0}}\right)\left(\hat{b}\cdot\frac{\partial\vec{b}}{\partial x_i^{V^0}}\right)\sigma_{ij}^{V^0} \tag{A.5}$$

The calculation of the derivatives of the impact parameter (A.2) with respect to the track coordinates (x, y, tx, ty) give the result:

$$\frac{\partial b_x}{\partial tx} = u_z\left[-\Delta(1-u_x^2) - u_x(x-V_x)(1-u_x^2) + u_x^2(y-V_y)u_y + u_z u_x(z-V_z)\right]$$

$$\frac{\partial b_x}{\partial ty} = u_z u_x\left[\Delta u_y + u_x u_y(x-V_x) - (y-V_y)(1-u_y^2) + u_z u_y(z-V_z)\right]$$

$$\frac{\partial b_y}{\partial tx} = u_y u_z\left[\Delta u_x - (1-u_x^2)(x-V_x) + u_y u_x(y-V_y) + u_x u_z(z-V_Z)\right]$$

$$\frac{\partial b_y}{\partial ty} = -u_z\Delta(1-u_y^2) + u_y u_z\left[(x-V_x)u_x u_y - (y-V_y)(1-u_y^2) + (z-V_Z)u_y u_z\right]$$

$$\frac{\partial b_x}{\partial x} = 1 - u_x^2$$
$$\frac{\partial b_x}{\partial y} = \frac{\partial b_y}{\partial x} = -u_x u_y$$
$$\frac{\partial b_y}{\partial y} = 1 - u_y^2$$
$$\frac{\partial b_z}{\partial x} = -u_z u_x$$
$$\frac{\partial b_z}{\partial y} = -u_z u_y$$
$$\frac{\partial b_z}{\partial tx} = u_z^2 \left[\Delta u_x - (x - V_x)(1 - V_x)(1 - u_x^2) + (y - V_y)u_x u_y + (z - V_z)u_x u_z\right]$$
$$\frac{\partial b_z}{\partial ty} = u_z^2 \left[\Delta u_y + (x - V_x)u_x u_y - (y - V_y)(1 - u_y^2) + (z - V_z)u_y u_z\right] \tag{A.6}$$

where the u_i are the components of the vector (A.1) and $\Delta = (\vec{T_0} - \vec{V}^0) \cdot \hat{u}_0$.

For the derivatives with respect to the primary vertex position, (V_x, V_y, V_z), the results are simpler:

$$\frac{\partial b_i}{\partial t_j} = -\delta_{ij} \tag{A.7}$$

The final result can be obtained by multiplying each derivative term in equations (A.6)with the corresponding covariance matrix error and summing all the terms, as shown in equation (A.5). These expresions were implemented in a C++ program that was used to calculate the impact parameter error.

Appendix B

Resume da tese

HERA-B é un experimento deseñado para medir violación CP no sistema de mesóns B, e en particular na canle $B_d^0 \to J/\Psi K_S^0$ [40], tamén chamada canle dourada. Utiliza o feixe de protóns de 920 GeV do anel HERA (DESY, Hamburgo) para producir colisións protón-núcleo cun branco fixo.

Neste traballo preséntase a medida do cociente entre a sección eficaz de producción dos mesóns D^+ e D^0, en colisións protón núcleo a 920 GeV, usando o detector de HERA-B. A mostra de datos utilizada foi tomada en Agoto do 2000, durante a fase de comisionado do detector, e consiste nuns 5 millóns de sucesos triggerizados cun leptón de alto momento transverso ($\mathrm{p_T}$).

Desenvolviuse un método para seleccionar as desintegracións de partículas de longa vida media. O método baséase na utilización do parámetro de impacto das trazas para definir a probabilidade de que a traza proveña da interacción primaria. As probabilidades de tódalas trazas producidas na desintegración combinánse nunha soa cantidade, que condensa moita información e polo tanto é moi efectiva para separa-lo sinal do ruído.

Este método aplícase na selección dos mesóns D cargados e neutros, que se utilizan logo para medir o cociente entre as dúas seccións eficaces de producción.

B.1 Introducción teórica

O estudo da producción de quarks pesados proporciona un bo test da teoría de perturbacións da cromodinámica cuántica (PQCD) debido a que a masa do quark pesado define a escala na que se ha de evaluar a constante de acoplamento forte, α_s. No caso de que a masa do quark sexa moito maior que a escala típica en QCD, $m_q \gg \Lambda_{QCD}$, pódese usar a teoría de perturbacións (PQCD). O feito de que existan quarks con masas moi diferentes permite evaluar os resultados obtidos con PQCD para rangos moi diferentes de enerxía, onde os efectos non perturbativos xogan papeis moi diferentes. Así, para o quark t espérase que os resultados obtidos cos primeiros termos do desenvolvemento perturbativo sexan bastante precisos, mentres que para o quark c, que ten unha masa moito menor, a teoría de perturbacións está no límite de se poder usar. Por este motivo, o estudo de producción de pares $c\bar{c}$ ou de mesons con *encanto* (*charm*) pode proporcionar pistas sobre qué efectos non perturbativos son mais importantes.

Actualmente existe unha grande cantidade de medidas sobre producción de quarks pesados: seccións eficaces de producción, distribucións inclusivas de hadróns, correlacións entre os quarks, distribución de jets, ... obtidas con diferentes mecanismos de producción (colisións hadrón-hadrón, electrón-positrón, electrón-fotón ou fotón-fotón). A pesares de que a maioría dos resultados están de acordo coas espectativas teóricas, existen todavía algunhas discrepancias. Un exemplo destas discrepancias é o cociente entre a sección eficaz de producción de mesóns D cargados e neutros [14]. Unha primeira estimación do valor deste cociente pódese obter fácilmente: considérese simetría de isospín na transición $c \to D$ e $c \to D^*$. Eso significa que a probabilidade de producción dos mesón D e D^* (cargados ou neutros), nun estado de polarización particular, será a mesma independentemente do tipo de mesón de que se esté a falar. Por contaxe dos estados de polarización a sección eficaz de D's será aproximadamente 1/3 da dos D^*. Con isto, usando os valores das fraccións de desintegración $D^* \to D$, obtense

$$R \sim 0.33. \tag{B.1}$$

As medidas experimentais obtidas para colisións pión-núcleo están próximas á predición teórica, como se pode ver na figura B.1. Sen embargo, os experimentos con colisións protón-núcleo obteñen cocientes moito maires, algúns deles próximos á unidade. As medidas con menor erro teñen valores mais pequenos, entre 0.5 e 0.7. Non existe ningunha razón pola que as colisións $p - N$ deban dar resultados diferentes das de $\pi - N$. Medidas máis precisas en colisións protón-núcleo poden axudar a discernir se este efecto é un producto da falta de estadística ou se, polo contrario, hai algún outro efecto descoñecido.

Nas seguintes seccións explicarase o método utilizado para a medida deste cociente co detector de HERA-B. Na primeira sección descríbese o detector, destacando as características mais importantes para esta análise. Na sección B.3 preséntase o método desenvolvido para seleccionar desintegracións de partículas con longa vida media. A reconstrucción dos mesóns D utilizando ese método explícase na sección B.4. Na última parte preséntase a medida do cociente das seccións eficaces de producción. Na última parte preséntanse as conclusións.

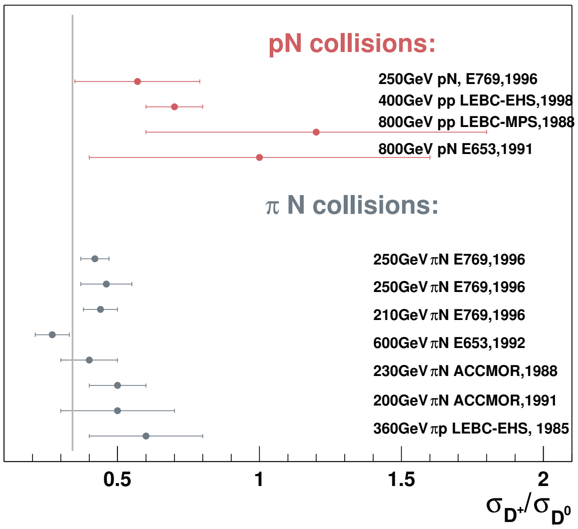

Figure B.1: *Medidas experimentais do cociente entre a sección eficaz de producción de mesóns D cargados e neutros, en colisións protón-núcleo e pión-núcleo. A predicción teórica está indicada cunha liña gris.*

B.2 O detector HERA-B

HERA-B é un experimento de branco fixo [40], deseñado para traballar cun alto ritmo de colisión e poder separar as desintegracións dos mesóns B_D^0, que ocorren aproximadamente en unha de cada $\sim 10^{11}$ colisións, para obter unha medida precisa do parámetro de violación CP, $sen(2\beta)$. Este programa de física tan innovador impuxo fortes condicións no deseño do trigger, do sistema de adquisición de datos e nas características do detector.

Na figura B.2 móstrase un esquema da disposición de cada un dos compoñentes.

HERA-B é un espectrómetro orientado na mesma dirección que o feixe de protóns incidente, que cubre unha rexión angular entre 10 e 160 mrad no plano paralelo ao campo magnético. Este ángulo é equivalente ao 90% da cobertura total no centro de masas.

O branco fixo está formado por dúas estacións de catro fíos cada unha, situadas entorno ao feixe de protóns, que se poden desprazar ó longo da dirección transversal do feixe ata acadar o ritmo de interacción desexado. A continuación sitúase o detector de silicio (VDS), que foi deseñado para separar con grande precisión o punto de desintegración do B_d^0 do punto onde se produxo a colisión primaria. Despois do VDS están colocados os detectores de trazas, dispostos en 13 estacións con varios planos cada un. A primeira estación está situada antes do campo magnético, xusto ó terminar o detector de vértice,

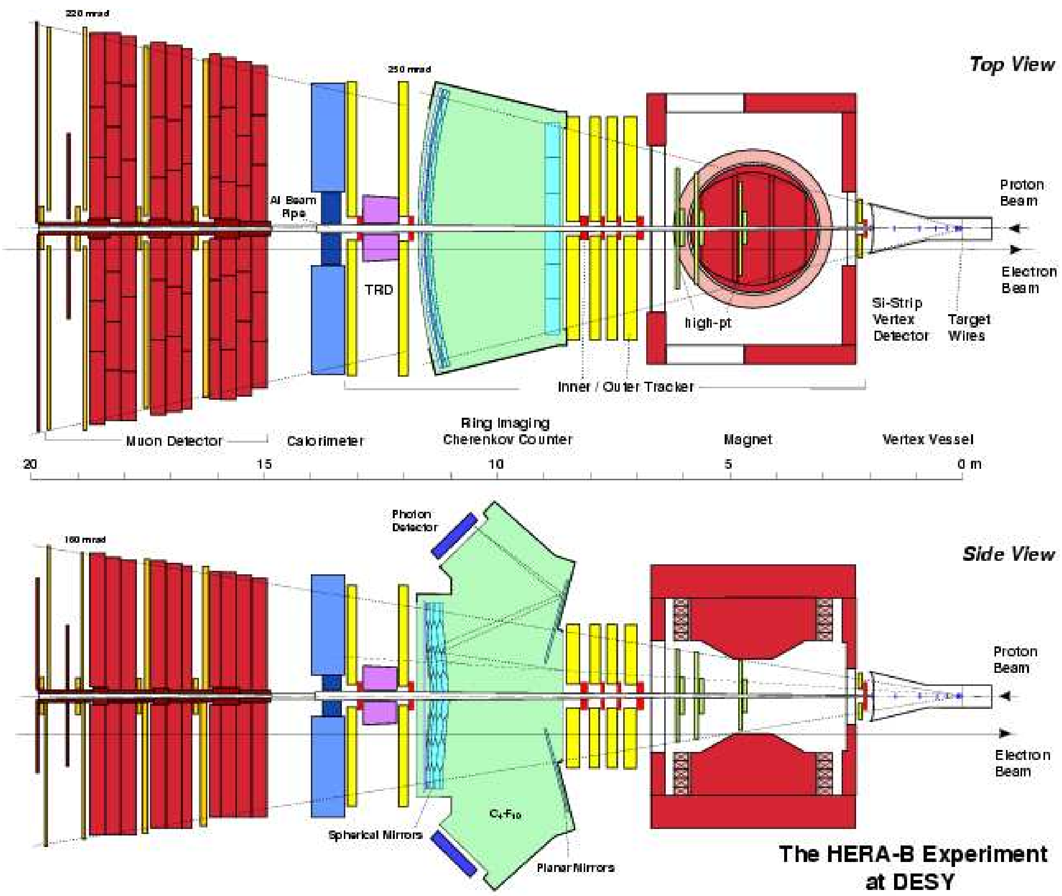

Figure B.2: *Vista esquemática do detector HERA-B.*

para asegurar que cada traza ten un punto medido antes do campo magnético. As oito estacións seguintes están dentro da rexión do campo magnético. O seu obxectivo é medir o punto de desintegración do K_S^0 con boa precisión. A continuacion, na rexión libre de campo, hai catro estacións mais, que se utilizan na reconstrucción de trazas. As dúas últimas estacións, coladas antes do calorímetro, utilízanse no trigger para comenzar a búsqueda dos dous leptóns procedentes da do J/Ψ.

O detector de trazas está feito con dúas tecnoloxías diferentes: a zona mas interna (10-100 mrad), onde o fluxo de partículas é mais grande, está cuberta con detectores de micro-strips (MSGC's). A parte mais externa, que recibe ocupancias menores, ten tamén menor granularidade, e está feito de cámaras de fíos dispostas en forma de panal de abella (*honey-comb drift chambers*).

O campo magnético de HERA-B ten unha intensidade maxima de 0.8 T, cunha integral de campo de 2.2 Tm, para proporcionar unha boa resolución no momento das trazas.

A identificación de partículas faise con tres subdetectores diferentes: o calorímetro electromagnético (ECAL), o detector de aneis de luz Čerenkov (RICH) e as cámaras de muóns. O RICH foi deseñado para separar pións de kaóns nun amplo rango de momentos, entre 10 e 60 GeV, co obxectivo de ser usado na identificacion do sabor do mesor B^0_d. O ECAL, situado ao final das cámaras de trazas, proporciona a identificación dos electróns e dos fotóns. Tamén se usa para proporcionar o sinal que comenza a búsqueda de trazas no primeiro nivel do trigger, chamado *pretrigger*. As cámaras de muóns, feitas de varias estacións de camáras de deriva e bloques de formigón como material absorbente, proporcionan a identificación dos muóns. Aparte diso, ao igual que o ECAL, úsanse no pretrigger.

O trigger de HERA-B ten como obxectivo principal buscar pares de leptóns (electróns ou muóns) de alto momento transverso, que veñan da desintegración da J/Ψ filla do B^0_d. Está dividido en catro niveles. O primeiro deles, o pretrigger, consiste nun sinal producido nas cámaras de muóns ou no ECAL, que proporcionan a identificación dos leptóns. O primeiro nivel do trigger fai un rápido seguemento da traza a través do detector de trazas, esixindo que haxa un punto de interacción en cada plano das cámaras usadas no trigger, cun algoritmo baseado en rexións de interese. O segundo nivel do trigger fai unha axuste rápido das trazas atopadas no primeiro nivel, propagadas ata o detector de vértice. Pode facer tamén unha reconstrucción do vértice secundario e aplicar un corte na distancia de desintegración. O terceiro nivel do trigger utiliza toda a información do suceso para facer unha reconstrucción máis precisa das trazas dos leptóns e do vértice de desintegración da J/Ψ. O cuarto nivel do trigger corresponde á reconstrucción do suceso e a súa clasificación en diversos grupos de interese para diferentes análises.

B.3 O método do parámetro de impacto

Para poder separar as desintegracións dos mesóns D do ruído desenvolviuse un método que consiste en sacar o máximo proveito dos grandes parámetros de impacto que caracterizan as desintegracións de partículas de longa vida media. Utiliza a significancia do parámetro de impacto ($S = b/\sigma_b$) da traza con respecto ó vértice primario, calculado en tres dimensións. O parámetro de impacto considérase positivo se o punto de máxima aproximación entre a traza e a liña de voo da partícula nai está na dirección cara adiante dende o punto onde ocorreu a colisión primaria. Neste sentido, precísase de reconstruir o vértice secundario no que se produxo a desintegración para poder calcula-lo signo. Con esta definición, os parámetros de impacto das trazas producidas na desintegración da partícula de vida media longa van ser sempre positivos. Polo contrario, para as combinacións de trazas que

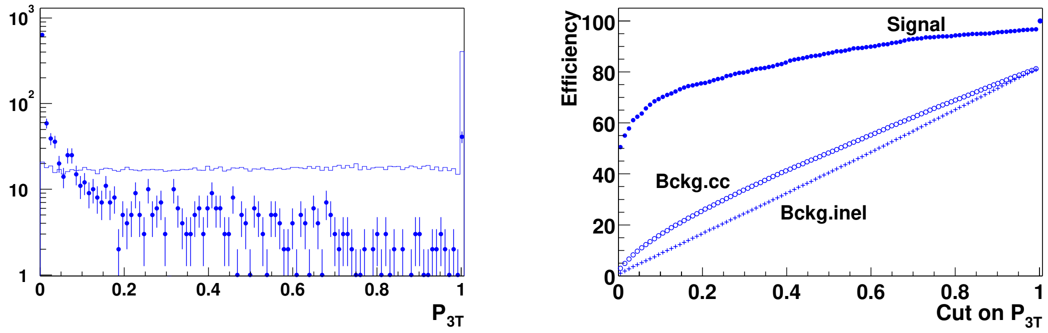

Figure B.3: *(a) Distribución da probabilidade de que as tres trazas fillas do D^+ proveñan do vértice primario, para o sinal (círculos azuis) e para o ruído en sucesos inelásticos (liña contínua). (b) Eficiencia do corte na probabilidade combinada para o sinal (círculos azuis), para o ruído producido en colisións inelásticas (cruces) e para o ruído producido en sucesos $c\bar{c}$ (círculos valeiros).*

proveñen do vértice primario, que forman a meirande parte do ruído na reconstrucción da desintegración, o signo ten a mesma probabilidade de ser positivo ou negativo.

A distribución da significancia dos parámetros de impacto negativos utilízase para definir a probabilidade de que a traza proveña do vértice primario. As probabilidades de tódalas trazas fillas con parámetros de impacto positivos combínanse nunha soa cantidade, a *probabilidade combinada* (P_N), que condensa moita información e polo tanto é suficiente para separar o sinal do ruído.

Na figura B.3 (a) móstranse as distribucións da probabilidade combinada, P_{3T}, para o caso de que se estea a reconstruir a desintegración $D^+ \to K\pi\pi$. O sinal, está indicado con círculos escuros, e o ruído producido en sucesos inelásticos, en Monte Carlo, cunha liña contínua. O sinal produce un pico moi estreito a cero, mentres que o ruído produce unha distribución prácticamente plana. A eficiencia do corte en P_{3T} para o sinal e para o ruído móstrase tamén na figura B.3 (b), en función do corte. Para unha rexección do ruído dun 96%, correspondente a un corte bastante suave ($P_{3T} < 0.05$) a eficiencia para o sinal é dun 64%. Un corte na vida media do D^+, por exemplo, tería unha eficiencia $\sim 30\%$ mais baixa para o mesmo factor de rexección do ruído.

Para que este método funcione é preciso que tanto o parámetro de impacto como o seu erro estean ben medidos. Na etapa na que esta tese foi feita existían sospeitas de que os errors das trazas non estaban ben medidos, mais non se sabía exactamente canto. Fíxose un estudo detallado dos erros das trazas e dos vértices primarios, para determinar se existía algún bias na medida da significancia do parámetro de impacto ou no seu erro. Atopouse que os erros das pendentes das trazas estaban subestimados, e aplicouse a corrección apropiada. Demostrouse que a significancia das trazas en datos reais está ben medida no caso de sucesos nos que houbo unha soa interacción primaria, identificados por teren só un vértice primario reconstruído.

B.4 Reconstrucción dos mesóns D

O método que se desenvolviu na sección anterior utilízase para reconstruir mesóns D^+ e D^0. Os cortes de selección optimizáronse de tal xeito que se maximice a significancia do sinal, definida como $S/\sqrt{B}$, onde S é o número de desintegracións $D^+ \to K\pi\pi$ ($D^0 \to K\pi$) reconstruídas no Monte Carlo e B o ruído en datos reais, obtido con combinacións erroneas de carga ($K^+\pi^+\pi^+$ ou $K^-\pi^-\pi^-$ para o D^+, e $K^+\pi^+$ ou $K^-\pi^-$ para o D^0).

- Utilízanse só sucesos que teñen un vértice primario, para asegurar que os errors están ben medidos. O vértice debe cumplir un par de condicións, para asegurar que está ben reconstruído:
  - Ter mais de 4 trazas.
  - A posición en z non debe estar moi lonxe do fío no que se produxo a colisión: $|z_{prim} - z_{fio}| < 3\sigma_z$, onde σ_z é o erro distancia entre o vértice e o fío.
- Identificación do kaón e do pión:
  - Tanto para o D^+ como para o D^0 identifícase o kaón requerindo que a probabilidade de que o anel detectado no RICH proveña dun kaón sexa maior que o 95%: $l_k > 0.95$.
  - Para o D^+, que ten maior ruído combinatorio, aplícase unha condición de identificación extra nunha das trazas non identificadas como kaón: que a suma das probabilidades de que o anel detectado no RICH proveña dun pión, dun electrón ou dun muón sexa maior do 5%: $l_e + l_\mu + l_e > 0.05$. Esta condición é pouco restrictiva, co obxectivo de eliminar trazas falsas mantendo a eficiencia de identificación alta.
- Reconstrucción do vértice secundario: os vértices secundarios con boa calidade selecciónanse requerindo que o promedio do cuadrado das distancias entre as trazas fillas e o vértice reconstruído (RMS) sexa menor que un certo valor máximo:
  - Para o D^+: $RMS < 0.017\,\mathrm{cm}$.
  - Para o D^0: $RMS < 0.018\,\mathrm{cm}$.

	Selección D^+		Selección D^0	
	Corte	Efic.	Corte	Efic.
RMS	$< 0.017\,\mathrm{cm}$	$(61 \pm 6)\%$	$< 0.018\,\mathrm{cm}$	$(88 \pm 2)\%$
P_N	$P_{3T} < 0.01$	$(47 \pm 4)\%$	$P_{2T} < 0.02$	$(22.5 \pm 0.7)\%$
Lifetime	—	—	$L > 1.6\,c\tau$	$(58 \pm 3)\%$
Corr.carga	O K ten a mesma carga que a tr. trigg.			

Table B.1: *Resume dos cortes aplicados na selección dos mesóns D. Só se usaron sucesos que teñen un vértice primario reconstruído.*

- Probabilidade combinada das trazas: para reducir o ruído producido por trazas que se orixinaron na interacción primaria requírese que a probabilidade combinada das trazas envolvidas na desintegración do mesón D sexa menor que un certo valor máximo:
  - Para o D^+: $P_{3T} < 0.01$.
  - Para o D^0: $P_{2T} < 0.02$.
- Para o D^0 o corte na probabilidade combinada é menos eficaz que para o D^+, posto que a eficiencia do método e a súa capacidade de rexección do ruído melloran para vidas medias largas e para maior número de partículas producidas na desintegración. A vida media do D^0 é tres veces menor que para o D^+, e ten só dúas trazas fillas, polo que o poder de separación do ruído é menor para o D^0.

  Para mellorar a significancia do sinal do D^0 requírese que a súa distancia propia de desintegración cumpla:

  $$L > 1.6 \cdot c\tau$$

  onde τ representa a vida media do D^0.
- O último corte de selección que se aplica explota o feito de que nos sucesos nos que se produxo un mesón D o leptón do trigger provén na meirande parte dos casos da desintegración semileptónica do outro quark c. Existe, polo tanto, unha correlación de carga entre o leptón do trigger e o sabor do D. A última condicion consiste en esixir que a carga do kaón sexa a mesma que a da traza do trigger reconstruída polos algoritmos do cuarto nivel do trigger.

Os cortes de selección resúmense na táboa B.1, onde tamén se indican as eficiencias de cada un deles.

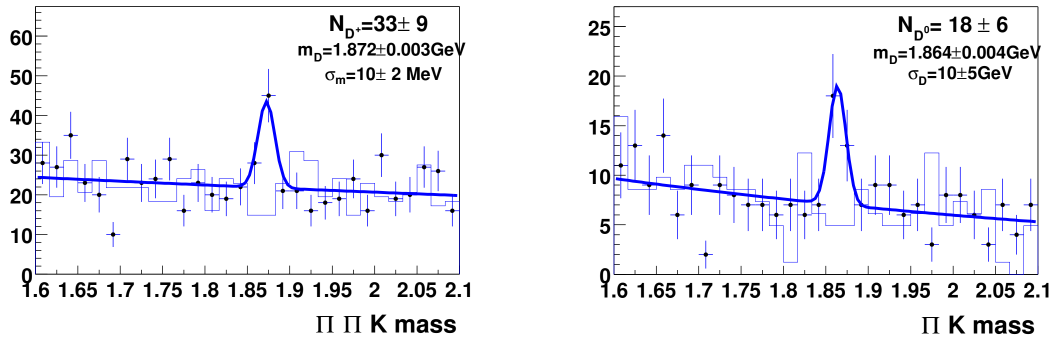

Figure B.4: *Distribución da masa invariante do D^+ (a) e do D^0 (b), obtida para os runs triggerizados cun leptón de alto momento transverso. O histograma de traza contínua representa o ruído obtido con combinacións erróneas de carga.*

O sinal que se obtén con esa selección para a mostra de datos triggerizada cun só leptón de alto momento transverso móstrase na figura B.4. O sinal ten unha significancia $\frac{S}{\sqrt{B}} \sim 3.6$ nos dous casos.

B.5 Cociente $\sigma_{D^0}/\sigma_{D^\pm}$

O cociente entre as seccións eficaces de producción do D^+ e do D^0 calcúlase a partires da expresión:

$$R = \frac{\sigma_{D^+}}{\sigma_{D^0}} = \frac{N_{D^+}}{N_{D^0}} \cdot \frac{\epsilon^{id}_{trigg}(D^0)}{\epsilon^{id}_{trigg}(D^+)} \cdot \frac{Acc(D^0)}{Acc(D^+)} \cdot \frac{\epsilon^{D^0}_{trk}(K,\pi)}{\epsilon^{D^+}_{trk}(K,\pi,\pi)} \cdot \frac{\epsilon_{vsec}(2dau)}{\epsilon_{vsec}(3dau)} \times$$
$$\times \frac{\epsilon_{PiD}(K)^{D^0}}{\epsilon_{PiD}(K,\pi)^{D^+}} \cdot \frac{\epsilon_{cuts}(D^0)}{\epsilon_{cuts}(D^+)} \cdot \frac{BR(D^0 \to K\pi)}{BR(D^+ \to K\pi\pi)} \tag{B.2}$$

Onde:

- $\frac{\sigma_{D^+}}{\sigma_{D^0}}$ é o cociente entre o número de D's que se reconstruíron na mostra de datos considerada.
- $\frac{\epsilon^{id}_{trigg}(D^0)}{\epsilon^{id}_{trigg}(D^+)}$: cociente entre a eficiencia do trigger para seleccionar sucesos nos que se produxo un D^0 con respecto á mesma eficiencia para os sucesos nos que se produxo un D^+.

- $\dfrac{Acc(D^0)}{Acc(D^+)}$: cociente entre a eficiencia xeométrica para o D^0 e para o D^+.

- $\dfrac{\epsilon_{trk}^{D^0}(K,\pi)}{\epsilon_{trk}^{D^+}(K,\pi,\pi)}$: cociente entre as eficiencias de reconstrucción de tódalas trazas producidas na desintegración do D^0 e do D^+.

- $\dfrac{\epsilon_{vsec}(2dau)}{\epsilon_{vsec}(3dau)}$: cociente entre as eficiencias de reconstrucción e selección de un vértice secundario con dúas trazas e con tres trazas.

- $\dfrac{\epsilon_{PiD}(K)^{D^0}}{\epsilon_{PiD}(K,\pi)^{D^+}}$: cociente entre as eficiencias da identificación das trazas producidas na desintegración do D^0 e do D^+.

- $\dfrac{\epsilon_{cuts}(D^0)}{\epsilon_{cuts}(D^+)}$: cociente entre a eficiencia de selección do D^0 e do D^+.

- $\dfrac{BR(D^0 \to K\pi)}{BR(D^+ \to K\pi\pi)}$: cociente entre a probabilidade de que o D^0 decaia a $K\pi$ e a probabilidade de que o D^+ decaia a $K\pi\pi$. Obténense do PDG [37].

A meirande parte destas eficiencias son calculadas co MC (eficiencia do trigger, da reconstrucción de trazas, da reconstrucción dos vértices, dos cortes selección e as aceptancias).

A eficiencia da identificación das trazas calcúlase a partires dos histogramas de eficiencias que se poden ver en [41]. As curvas de eficiencia convoluciónanse coa distribución do momento dos kaóns ou pións do MC, para obter a eficiencia total.

O resultado final obtido para o cociente é:

$$\boxed{R = \frac{\sigma_{D^+}}{\sigma_{D^0}} = 1.08 \pm 0.46(st.) \pm 0.41(syst.) = 1.08 \pm 0.63}$$

onde o primeiro erro é debido á estadística e o segundo aos errors sistemáticos. Este valor está de acordo cos resultados obtidos por outros experimentos en colisións protón-núcleo, e agrúpase coas medidas obtidas polos experimentos de maior enerxía.

O resultado que se presentou aquí é o único que se obtivo a partires dunha medida directa do cociente, xa que os outros experimentos obtiveron as seccións eficaces de produción de mesóns D^+ e D^0 por separado.

B.6 Conclusións

A producción de quarks pesados e a súa posterior hadronización proporcionan un proceso único para comprobar a teoría de perturbacións da cromodinámica cuántica. A pesares de haber moitas medidas experimentais neste campo, non todas elas están de acordo coa teoría. Un exemplo no que os resultados experimentais discrepan das predicccións teóricas é o cociente das seccións eficaces de producción dos mesóns D^+ e D^0. Máis medidas neste campo poden axudar a discernir se as discrepancias son debidas á falta de estadística ou se, polo contrario, existen efectos desconocidos na producción destas partículas.

O obxectivo desta tese é obter unha nova medida do cociente entre as seccións eficaces de producción dos mesóns D^+ e D^0, en colisións protón-núcleo a 920 GeV, usando o detector HERA-B. A mostra de datos utilizada consiste nuns 5 millóns de sucesos seleccionados ao nivel do trigger por teren un leptón de alto momento transverso.

Para seleccionar as desintegracións dos mesóns D^+ e D^0 desenvolviuse un método que extrae o máximo proveito dos altos parámetros de impacto que caracterizan a desintegración dunha partícula de vida media longa.

Este método aplícase na reconstrucción e selección dos mesóns D. O sinal resultante consiste en 33 ± 9 desintegracións $D^+ \to K\pi\pi$ e 18 ± 9 desintegracións $D^0 \to K\pi$. Con esto, o valor resultante para o cociente é:

$$R = \frac{\sigma_{D^+}}{\sigma_{D^0}} = 1.08 \pm 0.46(st.) \pm 0.41(syst.)$$

Este valor estáde acordo con medidas anteriores obtidas en colisións protón-núcleo. Tamén concorda coas prediccións teóricas debido ao grande erro do resultado.

Esta medida poderá ser mellorada cos datos que se tomen durante o periodo de toma de datos do 2002-2003, no experimento HERA-B. As melloras no detector, especialmente no trigger e no detector de trazas, aumentarán o poder de separación do método que se desenvolviu nesta tese, permitindo unha identificación máis eficiente dos mesóns D. Ao mesmo tempo, unha mostra de datos maior permitiría reducir o erro estadístico, que sigue sendo o erro predominante na medida que se presentou aquí.

Bibliography

[1] P.Nason, *Heavy Quark Production*, in *Heavy Flavours*, eds. J.Buras and M.Lindner, Advanced Series on Directions in High Energy Physics, World Scientific Publishing Co.

[2] M.Mangano, P.Nason and G.Ridolfi, *Nucl.Phys.* **B373** (1992) 295.

[3] P. Nason, S. Dawson and R.K. Ellis, *Nucl. Phys.* **B303** (1998) 607.

[4] W. Beenakker, H. Kuijf, W.L. van Neerven and J.Smith, *Phys. Rev.* **D40** (1989) 54.

[5] L.N. Lipatov, *Sov. J. Nucl. Phys.* **20** (1975) 95;
V.N. Gribov and L.N. Lipatov, *Sov. J. Nucl. Phys.* **15** (1972) 438;
Yu. L. Dokshitzer *Sov. Phys. JETP* **46** (1977) 641.

[6] G.Altarelli,G.Parisi, *Nucl. Phys.* **B126** (1977) 298.

[7] E.G. Floratos, D.A. Ross, C.T. Sachrajda, *Nucl. Phys.* **B129** (1977) 66, E ibid. **B139** (1978) 545.

[8] E.G. Floratos, D.A. Ross, C.T. Sachrajda, *Nucl. Phys.* **B152** (1979) 493.

[9] A. Gonzalez-Arroyo, C. Lopez and F.J. Yndurain, *Nucl. Phys.* **B153** (1979) 161.

[10] A. Gonzalez-Arroyo, C. Lopez, *Nucl. Phys.* **B166** (1980) 429.

[11] G. Gurci, W. Furmanski and R. Petronzio, *Nucl. Phys.* **B175** (1980) 27.

[12] W.Furmanski and R. Petronzio, *Phys. Lett.* **B97** (1980) 437.

[13] E.G. Floratos, C. Kounnas and R. Lacaze, *Nucl. Phys.* **B192** (1981) 417.

[14] S.Frixione, M.Mangano, P.Nason, G.Ridolfi, *Heavy Quark Production*, CERN-TH/97-16,hep-ph/9702287, 1997. Published in *Heavy Flavours II*, eds. A.J.Buras and M.Lindner, Advanced Series on Directions in High Energy Physics, World Scientific Publishing Co., Singapore.

[15] R. Bonciani, S. Catani, M. Mangano, P. Nason, *Nucl. Phys.* **B 529** (1998) 424, hep-ph/9801375.

[16] N. Kidonakis, G. Sterman, *Nucl. Phys.* **B505** (1997) 321.

[17] R.K. Ellis, D.A. Ross, *Nucl. Phys.* **B345** (1990) 79.

[18] J.C. Collins, R.K. Ellis, *Nucl. Phys.* **B360** (1991) 3.

[19] S. Catani, M. Ciafaloni, F. Hautmann, *Phys. Lett.* **B 242** (1990) 97.

[20] B.Mele, P.Nason, *Nucl. Phys.* **B361** (1991) 626.

[21] W.Furmanski and R.Petronzio, preprint TH.2933-CERN (1980), *Phys.Lett* **B97** 437 (1980).

[22] C. Peterson, D. Schlatter, I.Schmitt, P.M.Zerwas, *Phys. Rev.* **D27** (1983) 105.

[23] M.Mangano, *Two lectures on Heavy Quark Production in Hadronic Collisions*, CERN-TH/97-328, hep-ph/9711337, 1998.

[24] S. Aoki et al., WA75 Coll., *Prog. Theor. Phys.* **87** (1992) 1315, erratum ibid. **88** (1992) 621;

[25] S. Aoki et al., WA75 Coll., *Phys. Lett.* **B209** (1988) 113.

[26] G.A. Alves et al., E769 Coll., *Phys. Rev. Lett.* **69** (1992) 3147.

[27] M. Aguilar-Benitez et al., LEBC-EHS Coll., *Phys. Lett.* **B161** (1985) 404.

[28] M.I. Adamovich et al., WA92 Coll., *Nucl. Phys. (Proc. Suppl.)* **B27** (1992) 212.

[29] S.Barlag et al., ACCMOR Coll., *Z. Phys.* **C39** (1988) 451.

[30] S.Barlag et al., ACCMOR Coll., *Z. Phys.* **C49** (1991) 555.

[31] K. Kodama et al., E653 Coll., *Phys. Lett.* **B284** (1992) 461.

[32] K. Kodama et al., E653 Coll., *Phys. Lett.* **B263** (1991) 579.

[33] S.Barlag et al., ACCMOR Coll., *Z. Phys.* **C39** (1988) 451.

[34] R. Ammar et al. LEBC-MPS Coll., *Phys. Rev. Lett.* **61** (1988) 2185.

[35] M. Aguilar-Benitez et al., LEBC-EHS Coll., *Z. Phys.* **C40** (1988) 321.

[36] M.I. Adamovich et al., WA82 Coll., *Nucl. Phys. (Proc. Suppl.)* **B27** (1992) 212.

[37] D.E. Groom *et al.*, Eur. Phys. J. **C15** (2000)1.

[38] G.Marchesini and B.R. Webber, *Nucl. Phys.* **B310** (1988) 461.

G.Marchesini, B.R. Webber, G.Abbiendi, I.G.Knowles, M.H.Seymour and L.Stanco, *Comput. Phys. Commun.* **67** (1992) 465.

[39] references [32]-[35], [27]-[31] and:

G.A. Alves et al., E769 Coll., *Phys. Rev. Lett.* **77** (1996) 2388.

M. Aguilar-Benitez et al., LEBC-EHS Coll., *Phys. Lett.* **B161** (1985) 400.

[40] T.Lohse *et al.*, DESY-PRC 94/02 (1994).

[41] The HERA-B RICH group, *The HERA-B Ring Imaging Čerenkov Counter*, submitted to Elsevier Science, 2002.

[42] HERA-B collaboration, *Report on status and prospects*, DESY-PRC 00/04, 2000.

[43] HERA-B collaboration, *Update of status and plans for 2001/02*, HERA-B note 01-065, 2001.

[44] I.Kisel, S. Maschiocchi, *Celular Automaton for Tracking in the Silicon for the HERA-B Vertex Detector*, HERA-B note 99-242, 1999.

D. Emelianov, I.Kisel, *Track fitting algorithm based on the discrete Kalman filter*, HERA-B note 00-032, 2000.

[45] R.Mankel, A.Spiridonov, several HERA-B notes: 99-111, 98-206, 98-154, 97-082.

[46] http://www-hera-b.desy.de/subgroup/detector/ecal/care/care.html

M. Vila, *Progress report on the ECAL reconstruction software*, HERA-B note 97-135, 1997.

[47] D. Dujmič, *Open Charm Production at HERA-B*, PhD thesis, 2001.

[48] R. Pestotnik, *Identification of Pions, Kaons and Protons in the HERA-B Spectrometer*, PhD thesis, 2001.

[49] I.Ariño, *Measurement of hadron fractioons in Proton-Nucleus interactions at 920 GeV/c, using the HERA-B detector*, PhD Thesis, Universitat de Barcelona, 2001.

[50] O.Igonkina, http://www-hera-b.desy.de//subgroup/software/arte/MARPLE/index.html

[51] W. Hulsbergen, *A Study of Track Reconstruction and Massive Dielectron Production in HERA-B*, PhD thesis, 2002.

[52] P.Conde, *New scheme to form RTRA's*, Tracking Meeting, 7.02.2001.

S. Masciocchi *et al.*, Coll. Meeting, Feb. 19-23, 2001, Tracking Meeting.

[53] R.Mankel, *Aplication of the Kalman Filter Technique in the HERA-B Track Reconstruction*, HERA-B note 95-239, 1995.

[54] A.Spiridonov, *Momentum and angular resolution in the HERA-B detector*, HERA-B note 02-069, 2002.

[55] B. Fominykh, *Murec-B*, Software meeting, HERA-B (DESY, Hamburg) June-1999.

[56] M.A. Pleier, *Cloneremove V1.0*, HERA-B note 01-0062, 2001.

[57] M.A. Pleier, *Measurement of the $\Lambda/\bar{\Lambda}$ hiperon polarization in proton nucleus collisions at 920 GeV proton beam energy*, PhD thesis, Ruperto-Carola University, Heidelberg, 2002.

[58] D.Emeliyanov, V. Kekelidze, I.Kisel, M.Sang, S.Schaller, *Grover* (http://wwwhera-b.mppmu.mpg.de/analysis/grover.html) .

[59] D. Emeliyanov, I.Kisel, S.Masciocci, M.Sang, Y. Vassiliev, *Primary Vertex Reconstruction by ROVER*, HERA-B note 00-061.

[60] A. Somov, *HERA-B rate calibration and luminosity measurement using Ecal Energy Sum*, HERA-B note 00-005, 2000.

V.Vagnoni, *Measurement of the mean interaction rate at HERA-B using the ECAL energy spectrum*, HERA-B note 00-134, 2000.

J.Bastos, J.Carballo, M.Schmelling, *A Statistical Method for Monitoring the Luminosity of the HERA-B data*, HERA-B note 02-039, 2002.

W. Hulsbergen, *Discusion of the Statistical Method for Luminosity Determination*, HERA-B note 02-076, 2002.

[61] HERA-B collaboration, *Inclusive V^0 Production Cross Section from 920 GeV Fixed-Target Proton-Nucleus Collisions*, to be published.

[62] HERA-B collaboration, *Measurement of the $b\bar{b}$ Production Cross Section in 920 GeV Fixed-Target Proton-Nucleus Collisions*, Hep-ex/0205106, 2002. To be published in EPJC.

[63] HERA-B collaboration, *Backward Production of J/Ψ Mesons in Proton-Nucleus Collisions at $\sqrt{s} = 41.6\ GeV$*, to be published in Phys.Lett. B.

[64] O.Igonkina, *A study of the J/Ψ and χ_c production in p-N collisions at 920 GeV.*, PhD thesis, ITEP (Moscow), 2002.

[65] B. Petersen, *Beauty Production at HERA-B: Performance of the Second Level Trigger and the $b\bar{b}$ cross section in 920 GeV pN collisions*, PhD Thesis, University of Copenhagen.

[66] T.Sjöstrand, Computer Physics Comm. **82** (1994) 74, hep-ph/9508391.

[67] H.Pi, Computer Physics Comm. **71** (1992) 173.

[68] J.Ivarsson, P.Kreuzer, T.Lohse, *PYTHIA and FRITIOF: Event Generators for HERA-B*, HERA-B 99-067, 1999.

[69] R. Brun, R. Hagelberg, M. Hansroul, J.C. Lassalle, CERN-DD-78-2-REV.

[70] Thanks to D.Dujmič (University of Texas, Austin).

[71] D. Buskulic *et al.* [ALEPH Collaboration], Phys. Lett. B **313** (1993) 549.

D. Brown, M. Frank, *Tagging b hadrons using track impact parameters*, ALEPH note 92-135, 1992.

[72] R.J.Barlow *Statistics: a guide to the Use of Statistical Methods in the Physical Sciences*, John Wiley& sons, 1989.

[73] D. Emelianov, Coll. Meeting, May 13-17, 2002, tracking meeting.

[74] K.Kodama *et al.*, E653 Coll., *Phys. Lett* **B263** (1991) 573.

[75] R. Ammar et al. LEBC-MPS Coll., *Phys. Rev. Lett.* **61** (1988) 2185.

[76] Marko Starič, private comunication.

[77] T.Glebe, *VT++ version 1.0*, HERA-B note 00-175, 2000.

[78] T.Lohse, *Vertex Reconstruction and Fitting*, HERA-B note 95-013, 1995.

[79] R. Barlow, *Systematic errors: Facts and Fictions*, hep-ex/0207026, presented at *Advances Statistical Techniques in HEP*, Durham, March 2002.

[80] Robert Pernack, private comunication.